DEVICE FABRICATION AND RADIATION EFFECTS STUDIES

OF VARIOUS SEMICONDUCTORS

492863

by

T. W. Kim

W. W. Grannemann

Technical Report EE-200(72)ONR-005

December 1972

ACKNOWLEDGEMENTS

ABSTRACT

High mobility indium antimonide thin films were prepared using the electron-beam evaporation technique to permit study of thin-film structure and formation. Thin-film Hall devices and magnetoresistors were fabricated, and electron and stable fast neutron radiation effects on InSb films were studied. Gallium arsenide phosphide (GaAsP) and silicon MIS capacitors were fabricated by using aluminum oxide (Al_2O_3) and silicon oxide (SiO_x). Tellurium thin-film transistors (TFTs) were also fabricated using electron-beam evaporated Al_2O_3 or the anodization of aluminum. The device stability was studied before and after thermal annealing in different gases.

Physical properties of InSb compound semiconductors were studied to gain understanding of the detailed mechanism of thin-film nucleation and growth. It was found that larger grain size resulted in high mobility films. High mobility InSb thin films were prepared using the electron-beam gun at a rate of 300 to 500 Å/sec on precleaned glass substrates, maintained at 300°C, at a pressure of 2 to 3 x 10^{-7} torr. After being heated in an oven at 250°C for about 20 minutes, the films were recrystallized in a dry argon atmosphere (2 liters/min) between 520 and 535°C for 2 to 3 minutes. Electron mobility ranged from 40,000 to 68,000 cm^2/V-sec. For a two-layer thin-film Corbino disk, a magnetoresistance of 18 was obtained at 10 Kgauss.

When irradiated with electron dose rates up to 2 x 10^{11} rads(InSb)/sec at 2.3 MeV and with neutron fluences of 10^{14}, 10^{15}, and 10^{16} nvt, these films did not indicate any change in electron mobilities. However, at 10^{17} nvt, electron mobilities of all these films dropped below 20,000 cm^2/V-sec. The carrier removal rates ranged from 0.247 to 3.350 cm^{-1}.

The Al_2O_3 was deposited from single-crystal sapphire at rates of 60 to 200 Å/min in an oxygen background of 5 x 10^{-5} torr on n-type silicon or $GaAs_{1/2}P_{1/2}$; aluminum or chromium was the gate metal. The fabricated MIS devices were annealed at 250°C in helium (1 liter/min) for 20 minutes and in oxygen (1 liter/min) for 40 minutes. After annealing, the hysteresis loop of C-V characteristic curves disappeared, resulting

in excellent stability. While the inversion was observed in silicon MIS capacitors, depletion was observed in GaAsP. Surface-state charge and surface-state density values of Q_{ss} = -5.21 x 10^{-9} coulombs/cm^2, N_{ss} = 3.26 x 10^{10} states/cm^2 for silicon and Q_{ss} = -1.175 x 10^{-8} coulombs/cm^2, N_{ss} = 7.35 x 10^{10} states/cm^2 for GaAsP were obtained. The resistivity and breakdown voltage of the Al_2O_3 ranged from 10^{13} to 10^{14} ohm-cm and from 2.2 x 10^6 to 2.8 x 10^6 V/cm, respectively.

A rather high-transconductance tellurium TFT with well-saturated characteristics was fabricated using Al_2O_3 and the photoengraving technique. The gate was 5 x 600-mil aluminum; gold was used for the source and drain metal. The thicknesses of the insulator and semiconductor were 450 Å and 100 Å. For a gate voltage of 5 volts and drain voltage of 1 volt, transconductance and gain bandwidth product values of g_m = 9 x 10^{-3} mho and f_m = 0.77 x 10^6 Hz were obtained.

TABLE OF CONTENTS

LIST OF ILLUSTRATIONS

LIST OF ILLUSTRATIONS (continued)

CHAPTER I

INTRODUCTION

The achievement of metal-insulator-semiconductor (MIS) capacitors and thin-film transistors (TFTs) using thin-film semiconductor and insulator techniques is of considerable importance in microelectronics, especially in obtaining integrated circuits.

Studies of the thin-film structure and formation are helpful in fabricating high mobility III-V compound semiconductor thin films (Chapter II). High mobility thin films of indium antimonide are fabricated by using electron-beam evaporation and recrystallization processes developed at The University of New Mexico. Measurement of Hall effect and resistivity determines the electrical properties of these films, which are carrier type, carrier concentration, and carrier mobility. Applications of the fabricated high mobility thin films are the Hall devices and magnetoresistors in various geometries (Chapter III).

The indium antimonide thin films are polycrystalline in structure and have many crystalline imperfections; therefore, low doses of electron and neutron radiation do not change the film properties. Because of this, radiation-hardened thin-film devices can be fabricated.

One of the most important fabrication techniques for the MIS capacitors and MISTFTs is the development of a process which can be used to form a stable dielectric on the semiconductor surface (Chapter IV). Gallium arsenide phosphide (GaAsP) MIS capacitor research was begun at The University of New Mexico in 1969 and has continued toward the development of a suitable gate dielectric material. The dry thermal oxidation of GaAsP produces stable GaAsP MIS capacitors; however, aluminum oxide (Al_2O_3) study is also necessary to develop the dielectric-growth process which has been used to produce stable GaAsP MIS capacitors (Al-Al_2O_3-GaAsP structure). In order to verify the superiority of the Al_2O_3 in stability, the aluminum oxide (e.g., sapphire) was electron-beam evaporated on the n-n^+ type silicon chips as well as on the GaAsP, and electrical characteristics were measured. At the same time, the silicon

1

monoxide (SiO or SiO$_x$) was also evaporated on the GaAsP to compare SiO with Al$_2$O$_3$. Thermal annealing effects on electron-beam evaporated Al$_2$O$_3$ and wet anodized film were studied for different temperatures, gases, and times.

Insulated-gate thin-film field effect transistors (IGTFTs) have been fabricated using electron-beam evaporated thin films of indium antimonide and insulating films of aluminum oxide. However, considering the high mobility of indium antimonide, thin-film transistors with good room temperature drain characteristics have not been fabricated, primarily because of the narrow bandgap energy of InSb and the need for the development of a good recrystallization process for the very thin films of InSb. In the meantime, rather high transconductance tellurium-Al$_2$O$_3$-Al thin-film transistors with well-saturated drain characteristics have been fabricated using both wet anodization of aluminum and electron-beam evaporation of Al$_2$O$_3$, followed by thermal annealing in hydrogen, helium, and oxygen. Passivation of devices by Al$_2$O$_3$ overcoating was done to prevent possible contamination. These fabricated tellurium thin-film transistors have shown fairly stable drain characteristics.

A STUDY OF ELECTRON BEAM EVAPORATED HIGH-MOBILITY
INDIUM ANTIMONIDE AND III-V COMPOUND
SEMICONDUCTOR THIN FILMS

Properties of III-V Compound and InSb Semiconductors ·

In the period between 1940 and 1950, the technology of germanium
and silicon semiconducting elements was strongly emphasized. Until now
these materials have been the prime substances for a systematic investi-
gation of the semiconductor mechanism. Particularly, silicon technology
has been well developed and extended to large-scale integrated circuits.

After a long time of neglecting the study of compound semiconduc-
tor materials, Welker demonstrated that the III-V compounds have partic-
ularly interesting properties, that they are all semiconductors, and
that they have a close relationship to the semiconducting elements of
the fourth column of the periodic table (References 2-1 and 2-2). In
addition he was able to predict the important new characteristics of
these semiconductors and to prove them experimentally. Thus, a connec-
tion was exhibited between germanium and silicon, on one hand, and the
II-VI and I-VII compounds, on the other hand. However, the compounds
are technologically much more difficult to prepare, and the theoretical
model that had been developed for the covalently bonded elements—ger-
manium and silicon—could generally not be extended to the more ionic
compounds.

Some of the semiconducting compounds were known to crystallize in
the zinc-blende and wurtzite structures and consequently to have a bind-
ing mechanism similar to that of germanium and silicon.

Crystal Structure

The most important lattices with a tetrahedral arrangement are the
diamond lattice, the zinc-blende lattice, and the wurtzite lattice. In
the diamond lattice, each atom lies in the center of a tetrahedron

formed by the four nearest neighbors. Two neighboring tetrahedrons are oriented in such a way that the base triangles are rotated by 60 degrees from one another. The zinc-blende structure is formed in the same way except that the two nearest-neighbor points are occupied by different elements. The diamond lattice is consequently restricted to elements, the zinc-blende structure to binary compounds. The wurtzite lattice is not cubic but can be considered as two interpenetrating, close-packed hexagonal lattices. One of the four nearest-neighbot tetrahedrals is oriented in such a way that the two bases lie exactly over each other (Reference 2-3). In this chapter, InSb, one of the important group III-V compounds, which has a zinc-blende structure as shown in Figure 2-1, will be discussed.

Band Structure

The theory of the band structure of the III-V compounds in the vicinity of a symmetry point was developed quantitatively by Kane (Reference 2-4) and Dresselhaus (Reference 2-5) using k-p perturbation calculation of the quantum theory. From their calculations, the band structure as shown in Figure 2-2 is obtained.

The conduction band for InSb is parabolic near its minimum. With increasing k the curvature decreases, and the effective mass of the electrons therefore increases. The influence of the higher- and lower-lying bands causes a shift of the band at $k \neq 0$ to higher energies and a lifting of the spin degeneracy except in the [100]- and [111]-direction. The topmost valence band (V_1-band) is not influenced at all by the conduction band but is affected strongly by all the other bands. The spin degeneracy is lifted even at $k \approx 0$ (except in the [100]-direction) by terms linear in k. The maxima of the band lie on the [111]-axes outside of k = 0. The next highest valence band (V_2-band) is degenerate with the V_1-band at k = 0. It is nonparabolic, similar to the conduction band, and it contains terms linear in k which lift the spin degeneracy except in the [100]- and [111]-directions. The V_3-band is similar to the V_2-band except for the absence of linear k terms. Because of the nonparabolicity of the conduction and V_2 bands, three different effective masses must be introduced for an isotropic but nonparabolic band

4

◯ : Sb

▨ : In
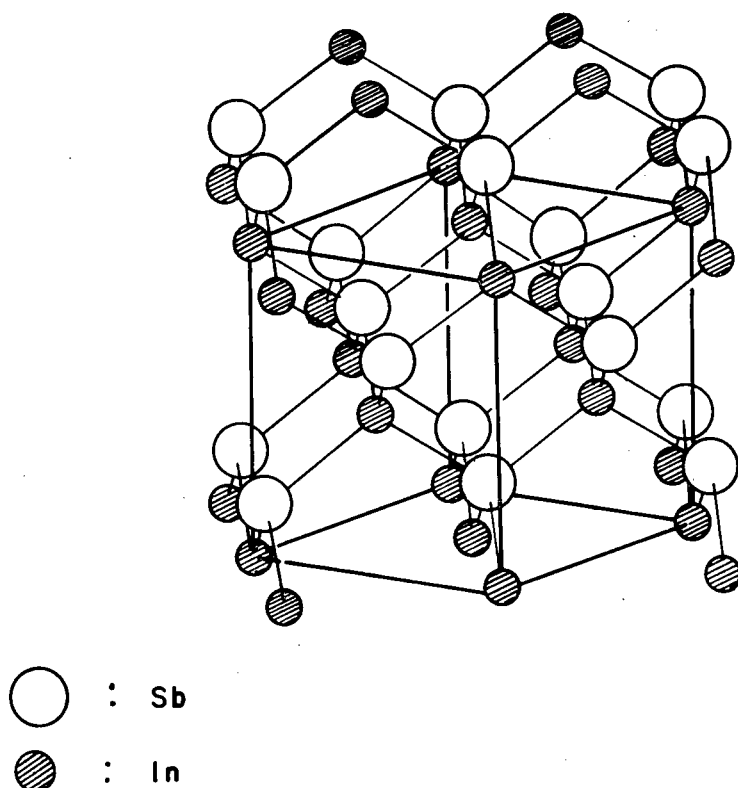
Figure 2-1. Zinc-Blende Lattice (B3-Type), Observed along a [110]
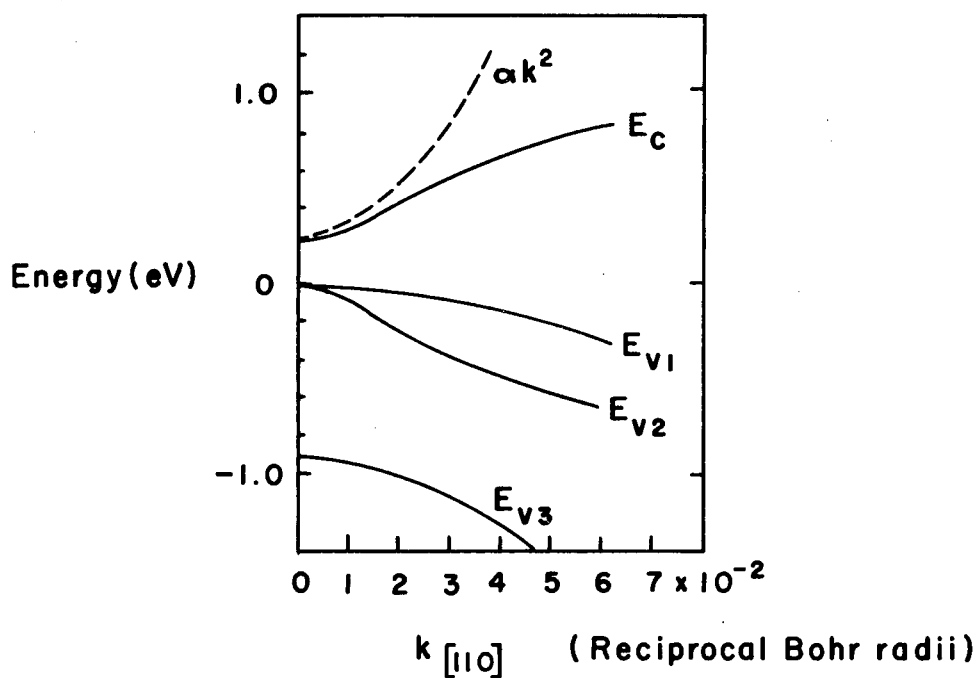
Figure 2-2. Energy vs. Wave Number in [110]-Direction
for InSb According to Kane

Splitting of the twofold degeneracy has not been included. The dashed
curve represents the parabolic approximation for the conduction band.

5

(Reference 2-3). Information about the shape of the valence band may be obtained from the band-to-band absorption of degenerate samples, where the Fermi level lies within one of the bands. A band model for aniso-tropic InSb with a single parabolic conduction band (E_C) and two degen-erate valence bands (E_{V1} and E_{V2}) at k = 0 is shown in Figure 2-3. For
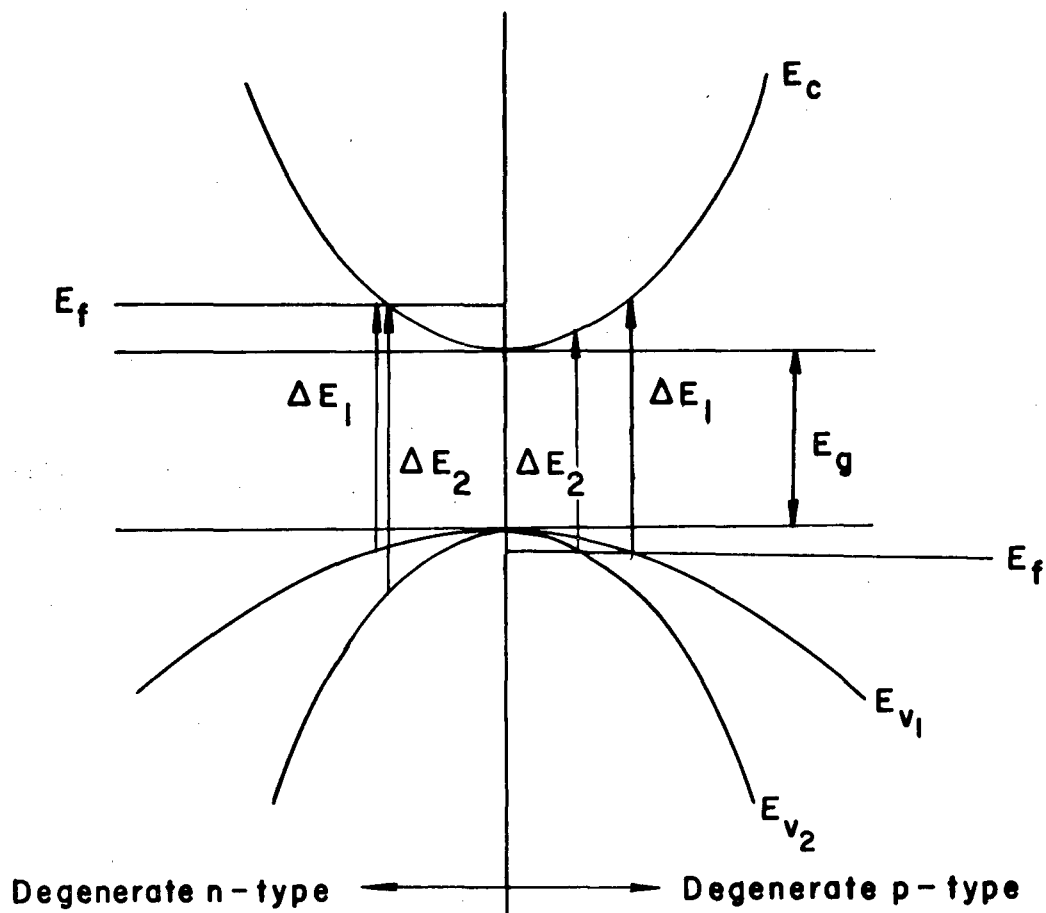
Figure 2-3. Band Model for an Isotropic Semiconductor with a Single Parabolic Conduction Band (E_C) and Two at k = 0 Degenerate Valence Bands (E_{V1} and E_{V2})

a semiconductor with isotropic conduction band and two valence bands which are degenerate at k = 0, if the sample is n-type, the Fermi level lies in the conduction band, and direct band-to-band transitions take place only above an energy $\Delta E_1 > E_G$. The absorption edge is displaced to higher energies. Additional transitions from the E_{V2}-band above ΔE_2 lead to an increased absorption. When the Fermi level lies in the

6

valence band, the absorption starts at ΔE_2 and increases once more discontinuously at ΔE_1. If the E_{V2}-band has a large curvature, ΔE_2 is almost equal to E_G. The absorption edge is then not shifted by degeneracy (Reference 2-3).

Properties of InSb Compound

1. Lattice constant, a   6.4787 Å

2. Coordinates

$$d_{InSb}^{[4]} = \frac{a}{4}\sqrt{3}$$

$$d_{In}^{[12]} = d_{Sb}^{[12]} = \frac{a}{2}\sqrt{2}$$

3. Number of molecules per unit cell, M   4 (4 In and 4 Sb)

4. Energy gap, E_G 0.167 eV at 300°K

       0.25 eV at 0°K

$$E_G = 0.25 - 2.8 \times 10^{-4}\, T$$

5. Electron mobility, μ_e 78,000 cm^2/V-sec

$$\mu_e = 78,000 \times \left(\frac{T}{300}\right)^{-1.66}$$

6. Hole mobility, μ_h 750 cm^2/V-sec

$$\mu_h = 2.55 \times 10^7\, T^{-1.81}, \text{ above } 100°K$$

$$\mu_h = 5.40 \times 10^6\, T^{-1.45}, \text{ } 30\text{-}100°K$$

7. Intrinsic concentration, n_i 2.06×10^{15} cm^{-3} at 300°K

$$n_i = 6 \times 10^{14}\, T^{3/2} \exp\left(\frac{-0.26}{2kT}\right)$$

8. Electron effective mass, m_n^* 0.013 m_o

$$0.01\, m_o < m_n^* < 0.02\, m_o$$

$$m_n^* = (0.016 \pm 0.007)m_o \text{ (Reference 2-3)}$$

9. Hole effective mass, m_p^* 0.6 m_o

$$m_p^* = 0.17\, m_o \text{ (Reference 2-3)}$$

10.	Conductivity, σ	3×10^2 to 6×10^2 $(\Omega\text{-cm})^{-1}$ for n-type
		2.5×10 to 2.5×10^2 $(\Omega\text{-cm})^{-1}$ for p-type
11.	Hall coefficient, R_H	7×10 to 3×10^2 $cm^3/coul$ for n-type
		6×10 to 7×10^2 $cm^3/coul$ for p-type
12.	Dielectric constant, ϵ	17
13.	Melting point, T_m	530°C
14.	Acceptors	Cd, Zn, and Mg
15.	Donors	Te, Se, and S

Bulk and Thin-Film Semiconductors

The properties of a thin film may be quite different from those of the bulk, particularly if the film thickness is very small. The thin films probably represent in many cases the most structurally imperfect materials available (Reference 2-6). These anomalous properties are due to the peculiar structure of the film, and this structure, in turn, is dictated by the processes which occur during film formation. Generally, thin films are prepared by depositing the film material, atom by atom, on a substrate. Such processes of deposition involve a phase transformation, and the formation of a thin film can be understood by a study of the thermodynamics and kinetics of this phase transformation.

The electrical properties of a thin film may bear little resemblance to the properties of the same material in bulk form, because the bulk properties may be completely masked by the effect of defects. Apart from those defects within the interior of the film, the surface itself acts as a gross defect. In the case of bulk materials the surface does not normally have an appreciable influence on the electrical conductivity, since its influence extends only a relatively short

distance into the interior. However, in the case of thin films, the effect of the surface may extend throughout the entire thickness of the material because of their greatly reduced third dimension. Moreover, in a thin-film transistor, both interfaces of the semiconductor film can influence the device properties, whereas only one interface is significant in the MOS field effect transistor.

Theories of Thin Film Nucleation and Growth

The best-understood process of film formation is that of condensation from the vapor phase. Since the production of thin films by vacuum deposition or vapor reaction in a gaseous-flow system is also the most important practical process, film formation by condensation from the vapor phase is the subject of this section.

Condensation simply means the transformation of a gas into a liquid or solid. Thermodynamically, the only requirement for condensation to occur is that the partial pressure of the film material in the gas phase be equal to or larger than its vapor pressure in the condensed phase at that temperature. However, this is true only if condensation takes place on film material already condensed or on a substrate made of the same material. In general the substrate will have a chemical nature different from that of the film material. Under these conditions, still a third phase must be considered, namely, the absorbed phase, in which vapor atoms are adsorbed on the substrate but have not yet combined with other adsorbed atoms. Condensation is initiated by the formation of small clusters through combination of several adsorbed atoms. These clusters are called nuclei, and the process of cluster formation is called nucleation. Since small particles display a higher vapor pressure than bulk material under the same conditions, a super-saturation ratio larger than unity is required for nucleation to occur (Reference 2-7). The process of enlargement of the nuclei to finally form a coherent film is termed growth. Frequently both nucleation and growth occur simultaneously during film formation. It is not sufficient to consider the condensation process to be simply equivalent to a random raining down on the substrate of sticky corkballs which stick where they impinge. Rather, there will be sufficient surface mobility on the substrate to

lead to the formation of well-defined islands of film material on the substrate even long after the nucleation step. Eventually these islands coalesce to form a continuous film, but this will generally occur only after the average film thickness has grown to several monolayers.

The general picture of the sequence of nucleation and growth steps to form a continuous film which emerges from nucleation theory and electron microscopic observations (References 2-6, 2-7, and 2-8) is as follows:

1. Formation of adsorbed monomers.

2. Formation of subcritical embryos of various sizes.

3. Formation of critically sized nuclei—nucleation step.

4. Growth of these nuclei to supercritical dimensions with the resulting depletion of monomers in the capture zone around them.

5. Concurrent with step 4, there will be nucleation of critical clusters in areas not depleted of monomers.

6. Clusters touch and coalesce to form a new island occupying an area smaller than the sum of the original two, thus exposing fresh substrate surface.

7. Monomer adsorbs on these freshly exposed areas, and secondary nucleation occurs.

8. Large islands grow together, leaving channels or holes of exposed substrate.

9. The channels or holes fill via secondary nucleation to give a continuous film.

Four stages of the growth process are distinguished as nucleation and island structure, coalescence of islands, channel formation, and formation of the continuous film. Some of these steps are shown schematically in Figure 2-4, and a schematic of the shape changes during coalescence is shown in Figure 2-5.

NUCLEATION   NUCLEI GROW   COALESCENCE-I   COALESCENCE-II

CHANNELS   HOLES   CONTINUOUS FILM
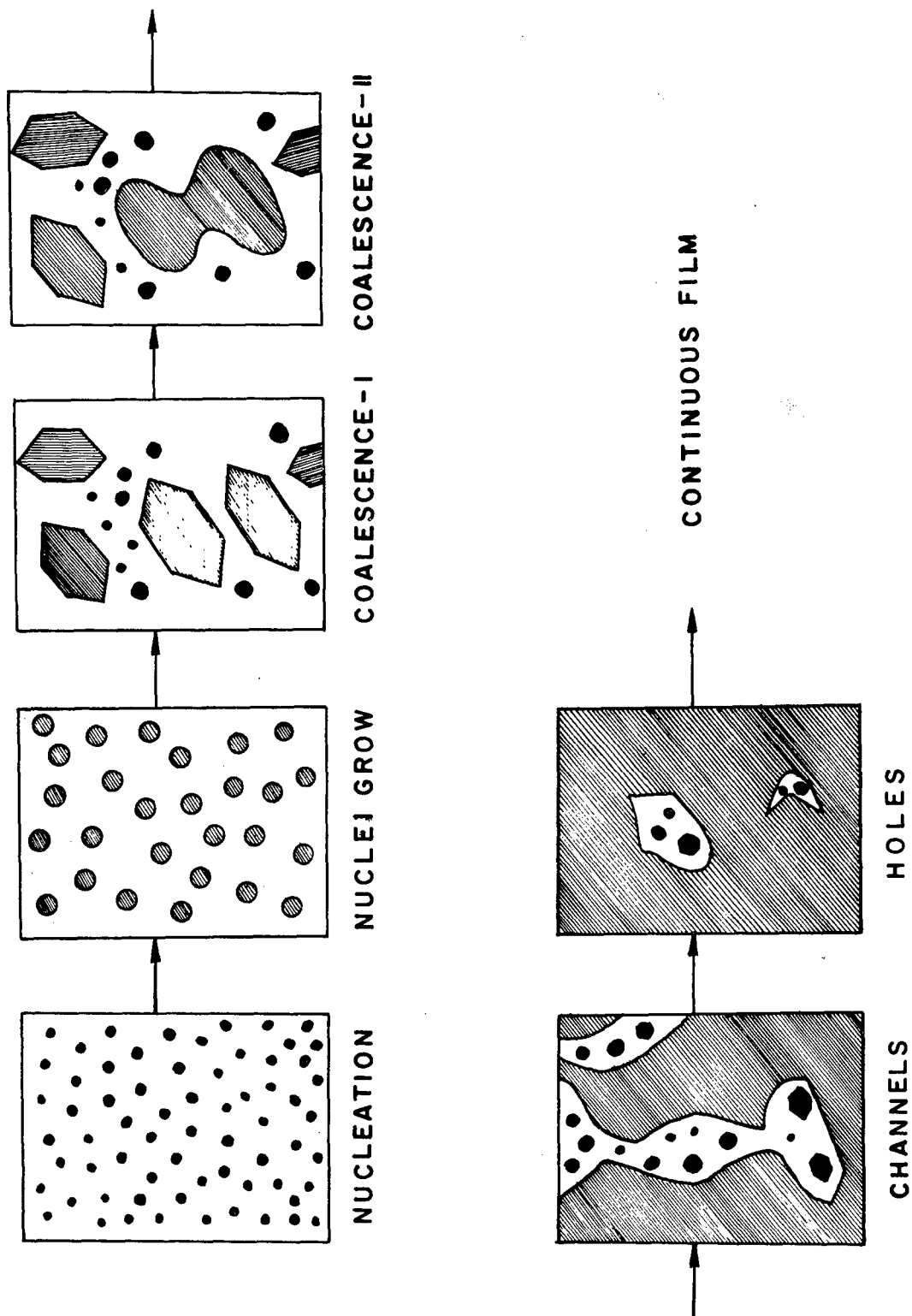
Figure 2-4.   Schematic of the Stages of Film Growth

11

INITIAL   FINAL
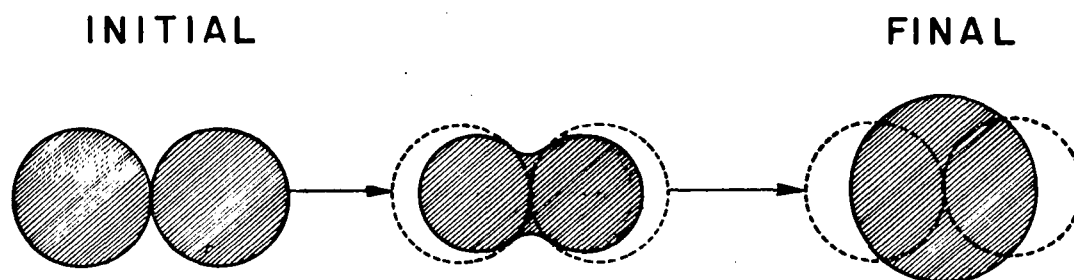
Figure 2-5.   Schematic of the Shape Changes
              During Coalescence

Vacuum Chamber Pressure and Deposition Rate

The residual pressure in the vacuum chamber can have a consider-
able effect on the properties of the film being deposited even if the
vacuum process is considered to occur in a virtually impurity-free at-
mosphere. For example, if the substrate were cooled so that the mole-
cules of residual gas bombarding it all condensed, a gas film would grow
at the rate of about 60 Å/min, for a pressure of 10^{-6} torr in the vacuum
chamber (Reference 2-6). It is quite common for films to be deposited
at this rate, but fortunately they contain a gas impurity content of
less than 50 percent, since all the gas molecules striking the condens-
ing film do not necessarily react with it. However, to obtain the pur-
est films, it is often desirable to deposit the films at a high rate so
that the freshly deposited surface, with its unsatisfied valences, can
be recovered with more evaporant before a significant number of gas
molecules have time to strike the surface. Thus, it is not the residual
pressure alone that determines the proportion of trapped gas, but the
ratio of the deposition rate to the pressure.

Defects and Grain Boundaries

When the islands during the initial stages of film growth are
still quite small, they are observed to be perfect single crystals.
However, as soon as the islands become large enough so that they touch,
grain boundaries or lattice defects will be incorporated into the film,
unless the islands coalesce to form a single grain. This latter phenom-
enon is indeed frequently observed, even if the two initial nuclei are

12

in completely different orientations (Reference 2-8). Observation of defects introduced during the growth of evaporated-metal films became possible with the application of the electron microscope to problems of thin-film structure. Thus, even in polycrystalline film a recrystallization process occurs continuously, at least during the early stages of formation of films, resulting in a number of grains per unit area which is much less than the density of initial nuclei. Sooner or later, however, a large number of defects is incorporated when these grains grow together, even in single-crystal films grown epitaxially.

Usually, single-crystal films were studied to observe the defects since such films display their defects more clearly than polycrystalline deposits. However, the types of defects observed in these films and their mode of formation are probably typical of what might be found in any evaporated film, single crystal or not, with the possible exception that stacking faults and twin boundaries probably occur much less frequently in fine-grained polycrystalline films than in single-crystal films, and that the grain-boundary area is much larger in polycrystalline films.

According to the laws of thermodynamics, all crystals contain an equilibrium number of vacancies in the lattice at any finite temperature. The reason is that an atom has the choice of two energy levels in the crystal. The lower energy state occurs when an atom is in the interior and all the valences are satisfied. The higher energy state occurs at the surface where all the valences are not satisfied. Consequently, the number of vacancies increases with temperature since the probability that an atom will be in the higher energy state by diffusing to the surface rather than in the lower state in the interior is given by the Boltzmann factor. Thus, a certain number of vacancies will form during the formation of the film, depending on its temperature. Due to the somewhat imperfect method of producing vacuum-deposited films, which corresponds roughly to quenching from the vapor phase to the solid, the number of vacancies may be considerably larger than the room temperature equilibrium value. When the film cools, all of the excess vacancies cannot collapse since this causes the film to shrink—an effect opposed by the bonding to the substrate; this situation leads to stresses in the

film. Thus a large number of vacancies may become locked into the film. The stress may already be large anyway because of the tendency of the crystallites to flow into each other, when they first touch during growth, thereby reducing their surface energy. The fact that they are bonded to the substrate restricts their movement, and considerable stress results. The large number of vacancies in a vacuum-deposited semiconductor film can dominate its electrical properties, since vacancies can ionize and act as donors or acceptors.

The most frequently encountered defects in evaporated films are dislocations. A density of 10^{10} to 10^{11} lines/cm^2 is frequently encountered. Most information about dislocation in evaporated films comes from electron microscopic investigations of films of face-center cubic metals. There are six mechanisms by which dislocations can be formed in such films during growth:

1. When two islands whose lattices are slightly rotated relative to one another coalesce, they form a sub-boundary composed of dislocations (Reference 2-7).

2. Since the substrate and film usually have different lattice parameters, there will be a displacement misfit between islands. Dislocations can result from this misfit when islands grow together.

3. Stress present in continuous films can generate dislocations at the edges of holes usually present in the earlier stages of film growth.

4. Dislocations ending on the substrate surface may continue into the film.

5. When islands containing stacking faults bounded by the surfaces of the island coalesce, partial dislocations must now bound these faults in the continuous film.

6. A dislocation network may be set up at the interface between film and substrate to relieve the strain.

For greater film thickness, there is evidence of longer dislocation lines running parallel to the film plane. If the dislocation

density is measured during film growth, it is found that most dislocations are incorporated into the film during the channel (or network) and the hole stage.

The displacement-misfit mechanism is responsible for many of the dislocations at this stage of growth.

Stresses in the growing film and resulting plastic deformation are responsible for multiple incipient dislocations observed in holes.

It is considered that plastic deformation is the most probable explanation of the multiple incipient dislocations observed in holes.

The minor defects observed frequently in deposited films include dislocation loops, stacking-fault tetrahedra, and small triangular defects. Dislocation loops may be as large as 100 to 300 Å.

A large number of vacancies can be introduced into deposited films during preparation for two reasons. First, the effective temperature at which impinging atoms freeze into the lattice is probably considerably higher than the normal substrate temperature. Second, metal films are often formed by a rapid condensation in which a deposited layer of atoms is covered by succeeding layers, before reaching thermal equilibrium with the substrate. In this way, many vacancies can become trapped in the film.

Dot-like features are often observed in electron micrographs of evaporated films. They are believed to be either unresolved dislocation loops, vacancy aggregates, or aggregates of impurity atoms trapped in the film during preparation.

The interpretation of the formation of minor defects by vacancy or interstitial condensation is somewhat in doubt, since features can be formed in the specimen while it is being observed in the electron microscope, because of bombardment by negative ions originating in the electron gun (Reference 2-7). There is no conclusive evidence of any defects arising from point-defect aggregation. This is not a surprising situation, since the mobility of point defects at the temperature of formation of many films will be sufficiently high to allow the vacancies and interstitials to escape to the film surface. However, films formed

under conditions where the point-defect mobility is small might be expected to contain impurities due to point-defect aggregation.

In general, a thin film will possess a larger grain-boundary area than bulk materials, since the average grain size will generally be smaller. In the extreme case of very low surface mobility, the grain size of the film may not be much larger than the size of the critical nucleus. However, the islands will be much larger when they touch. The grain size depends on deposition conditions and annealing temperature, as indicated schematically in Figure 2-6. The common feature in the behavior illustrated in Figure 2-6 is that the grain size saturates at some value of the deposition variables. With film thickness as the deposition variable, this means that new grains are nucleated on top of the cold ones after a certain film thickness has been reached. Nucleation of a new grain may become necessary because of a layer of contamination making coherent growth with the grain below impossible, or if the top surface of the grain below is a nearly perfect close-packed plane.

Larger grain sizes are naturally expected for increasing substrate or annealing temperature because of an increase in surface mobility, thus allowing the film to decrease its total energy by growing large grains and also decreasing its grain boundary area. Under a kinetic regime, the fastest growing crystal planes will grow at the expense of the slower ones, thereby leading to large surface roughness. These surface structures are to be expected at higher substrate temperatures. Low temperatures, on the other hand, lead to small grain sizes. The formation, structure, and annealing of films of very small grain size have been described by Buckel and Mönch and coworkers (References 2-10 and 2-11), and Suhrmann and Schnackenberg (Reference 2-12). An amorphous or liquidlike structure has been obtained only if large amounts of impurities are codeposited to inhibit grain growth (References 2-13, 2-14, and 2-15). However, it is significant that even at the lowest substrate temperatures explored so far, in the liquid helium temperature region, metal deposits are still found to be crystalline and therefore possess a small but finite crystal size. The dependence on deposition rate is less obvious but can be rationalized on the basis that film atoms just impinged on the surface, although they may possess a large
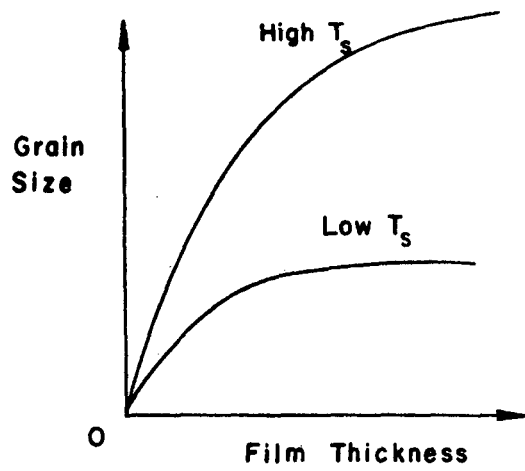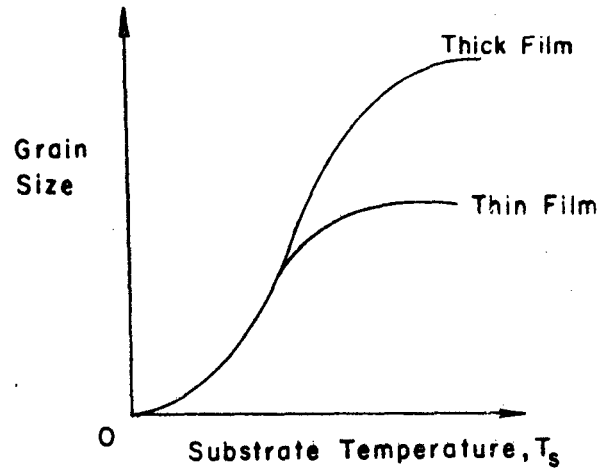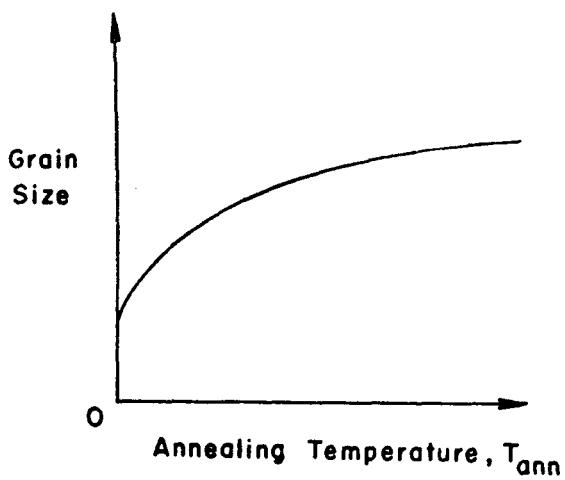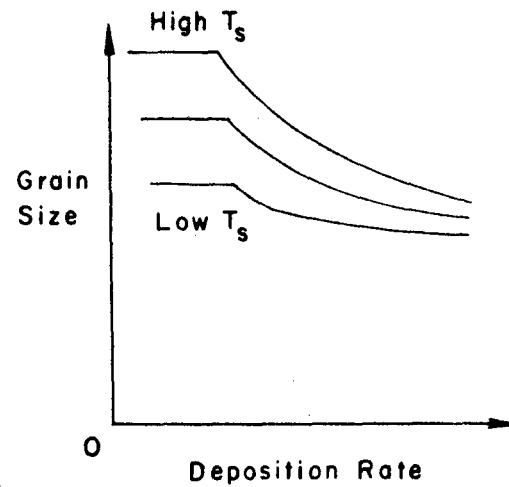
Figure 2-6.   Dependence of Grain Size on Film Thickness,
Substrate Temperature, Annealing Temperature,
and Deposition Rate (Reference 2-7)

17

surface mobility, become buried under subsequent layers, at high deposition rates, before much diffusion can take place (Reference 2-9). In order for this effect to operate, a certain minimum rate must be exceeded. Below this threshold rate, grain size is limited by temperature only; above it the grain size is decreased more for higher rates. During the formation of a semiconductor film, and also during any subsequent annealing, any impurity atoms in the crystallites which do not fit into the lattice may diffuse out and remain in the grain boundaries where the packing of atoms is necessarily less compact. Moreover, the lower packing density of atoms in the grain boundaries and their great freedom of movement provide paths for diffusion of impurities from the external environment.

If the electron concentration is n_{ec} in the crystallites and n_{eb} in the boundaries, then the difference in concentration leads to a potential barrier of amplitude ϕ, given by

$$\phi = \frac{kT}{q} \ln\left(\frac{n_{ec}}{n_{eb}}\right)$$

as in a conventional p-n junction diode. However, it is not necessary for the region in the grain boundary to be converted from n- to p-type conductivity. The differences in effective donor concentrations are sufficient to set up a potential barrier, as in an n-n$^+$ junction which does in fact rectify in the same manner as a p-n junction, except that the backward resistance is relatively low. Thus the grain boundaries in conjunction with the crystallites on either side of them behave in a manner similar to back-to-back p-n junctions, one of which is always back biased, irrespective of the direction of the applied potential difference, and consequently opposes the flow of current. The structure of the film is shown in Figure 2-7.

The additional resistance introduced by the boundaries is not attributed to the ohmic resistance of the boundaries themselves, since the proportion of the total volume they occupy is negligible. In fact, if the resistivity of the crystallites is decreased by increasing the donor concentration, the resistance of the semiconductor could increase because of the resultant increase in barrier height. Since the resistance

Low Carrier Concentration

High Carrier Concentration
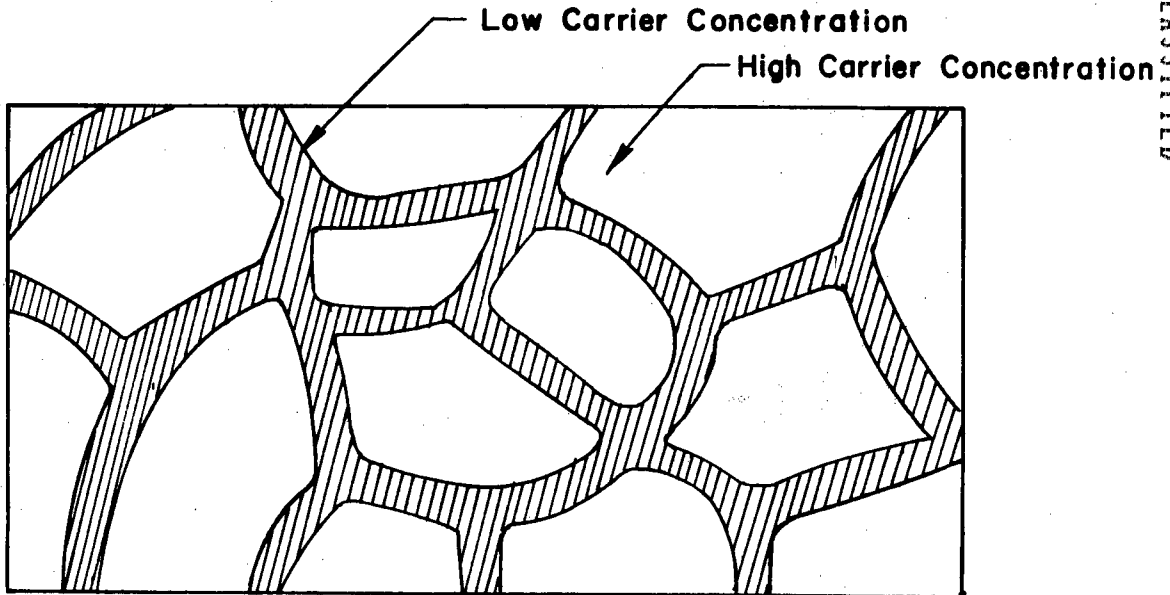
Figure 2-7. Schematic Drawing of Grain Boundaries
Between Crystallites

of the junction is nonlinear, the current density J in the barrier varies with the potential difference V_j applied across the junction in a similar manner to the current in a p-n junction, which is given by

$$J \propto \exp\left(-\frac{\phi}{kT}\right)\left[1 - \exp\left(-\frac{qV_j}{kT}\right)\right]$$

Total film energy can be minimized by keeping the surface area as small as possible, i.e., ideally flat. A certain surface roughness, and therefore an increased surface area, must be expected because of the randomness of the deposition process. If atoms stick where they impinge on the substrate without subsequent surface diffusion, then statistical fluctuations in the local film thickness will result. The average thickness deviation Δd from the average film thickness d is given by Poisson's probability distribution of a random variable (Reference 2-16) and reduces to

$$\Delta d = \sqrt{d}$$

Thus the surface roughness, and therefore the surface area of such a film, increases with the square root of the film thickness.

Surface migration can lead to less surface area by filling in the valleys and leveling the peaks to give a lower surface energy. If deposition occurs in a system in which the residual gas pressure is high enough for condensation of the vapor atoms into small smoke particles, then a very porous structure with a very large internal surface area must be expected because of the loose packing of the particles on the substrate, leaving much empty space. This is particularly true if the substrate temperature is so low that a substantial rearrangement of the atoms after deposition is unlikely.

Surface Scattering

The scattering properties of the surface are different from those of the interior because the surface represents a gross discontinuity in the structure. In addition, it may contain a number of occupied surface states or traps which act as charged scattering centers and scatter more strongly than does the lattice.

When the film thickness is much greater than the mean free path (average distance between collisions at which deflection of the carriers occurs) most of the collisions are with scattering centers in the interior of the film. However, when the film thickness approaches the dimensions of the mean free path, the majority of carriers in the film are constrained nearer to the surface; thus scattering of carriers by the surface becomes more frequent. Since the surface scatters more strongly than the interior, the carrier mobility decreases with decreasing film thickness.

Since the concentration of injected electrons in a thin-film transistor is, in general, largest at the surface of the semiconductor because of the formation of a surface channel, intercrystalline barrier modulation is restricted to the surface layer.

Apart from the intercrystalline barrier modulation, mobility modulation is attributed to a change in the number of effective scattering centers. A positively ionized charge center, i.e., a structural defect, ionized donor, or other impurity, acts both as a powerful scattering center and as a trapping center. If part of the injected charge is sacrificed by neutralizing such positive scattering centers, the resultant

20

decrease in the modulation may be more than compensated for by the increase in mobility.

Electron Beam Evaporated High-Mobility InSb Thin Films

Vacuum deposition methods utilizing evaporation continue to receive considerable attention from workers interested in exploring basic formative processes and physical properties. Also, the prospect of ultimately fabricating passive and active components in integrated circuits by compatible techniques continues to excite growing interest in the extended application of newer evaporative approaches. The range of potentially useful semiconductor materials is now extremely wide, and their marked differences in physical and chemical properties have made it necessary to devise a variety of vacuum techniques, each suited primarily to the deposition of films of one class of substances. These vacuum deposition methods have been applied thus far to the growth of elemental and compound semiconductor films. Particularly, at The University of New Mexico, new thin-film vacuum deposition technology for the compound materials has been developed using an electron beam source which is not known to the compound semiconductor workers (References 2-17, 2-18, and 2-19).

Semiconducting materials display an extremely wide range of vapor pressures, and therefore a corresponding variation in the ease with which they can be vaporized to form thin films. From the treatments of Dushman (Reference 2-20) and Holland (Reference 2-21), the rate of vaporization N_e for an element is given by the expression

$$N_e = 3.513 \times 10^{22} \, a_1 P_e / (M_e T_e)^{1/2} \text{ molecules/cm}^2\text{-sec} \qquad (2\text{-}1)$$

where

a_1 = an evaporation coefficient which is equal to unity with a clean evaporant surface

P_e = vapor pressure

T_e = temperature

M_e = atomic weight

In standard as well as in more complex methods of evaporating semiconducting films the background pressure in the system and the source design play a vital role. These factors not only affect the vaporization rate, but also, through chemical reactions during evaporation or condensation, can modify profoundly the structural and electrical properties of the film. Depending upon the type of pumping system used, the ambient in which evaporation is carried out will contain a variety of gaseous impurities. Mass spectrographic analysis commonly shows the residual background gases to be composed of H_2O, CO_2, O_2, N_2, H_2, and various organic vapors, e.g., CH_4. These impurities arise from desorption from the chamber walls, decomposition of pump oils, and outgassing from elastomer or synthetic rubber seals (Reference 2-21). The equation expressing the rate at which such gas molecules strike the substrate surface takes essentially the same form as Equation 2-1 above, i.e.,

$$N_g = 3.513 \times 10^{22} \, P_g / (M_g T_g)^{1/2} \text{ molecules/cm}^2\text{-sec} \qquad (2-2)$$

where g means gas.

The rate N_d at which the evaporant is deposited is related to N_e in Equation 2-1 by a geometrical constant. Thus from Equations 2-1 and 2-2,

$$\frac{N_g}{N_d} = \left(\frac{P_g}{P_d}\right) K$$

where

K = constant whose value depends among other things upon the geometry of the source-substrate arrangement.

It is clearly desirable to keep the ratio N_g/N_d negligibly small, and this is only achieved by using low pressures ($< 10^{-8}$ torr) or high deposition rates.

Vacuum Evaporation Methods

Earlier experiments in the vacuum evaporation of semiconductor elements and compounds involved the use of resistively heated sources almost exclusively, and these are still in vogue. Some of the more successful source materials, chosen so as to minimize chemical interactions and hence contamination of the film, are W, Mo, C, Ta, SiO_2, and Al_2O_3. Although some materials such as Mo, Ta, and W may be relatively stable in good vacuum, the presence of reactive gases, e.g., H_2O or O_2, may lead to the formation of volatile metal oxides which are incorporated in the grown film. It is now widely recognized that an effective solution to this problem is to use a crucible-free or cold-crucible source in which the evaporant is heated by electron beam bombardment. If the semiconductor is contained in a well-cooled crucible of high thermal conductivity, it may be melted by means of electron bombardment without the occurrence of chemical interaction at the semiconductor-crucible interface. To reduce the relative importance of gaseous contaminants and of interdiffusion and to achieve rapid fabrication of active devices on a competitive commercial scale, it is desirable to deposit films at rates in the micron per minute range.

A multisource deposition (three-temperature deposition) and a flash evaporation method are commonly applied for the deposition of compound films. Control of the incident fluxes and condensation conditions at the substrate is obtained by means of a three-temperature deposition method, whereby the temperatures of the source for elements A and B (e.g., In and Sb) and of the substrate are separately adjusted. For a compound which dissociates on evaporation and loses its most volatile components first, the flash evaporation method is used to grow stoichiometric films, which fulfills grain-by-grain vaporation of the compound using an arrangement of the type shown by Richard (Reference 2-22). Impurities required for n- or p-type doping of the films may be introduced into the compound powder charge. However, it is necessary to employ granulated charges of the compounds themselves or mixtures of these; the low-melting-point group III elements (e.g., In) are often not physically amenable to being evaporated as powders.

The electron beam deposition method which was recently developed at The University of New Mexico is so powerful that for the InSb films 78,500 cm^2/V-sec of mobility can be obtained.

Vacuum Deposition by Electron Beam Source

It is known to the III-V compound workers that vacuum deposition by an electron beam source cannot be used for the volatile III-V compound materials because the quick evaporation of group V elements compared to that of group III elements results in the group III elements being left in the crucible. Even if for the first stage of evaporation a stoichiometric film can be attained, much costly material is lost.

In this laboratory, the vacuum deposition by electron beam gun in the Drivac system (which does not use a pumping oil) becomes possible by modifying some of the factory-recommended operating procedures.

Instead of using the built-in copper crucible in the electron beam gun assembly, a trimmed molybdenum boat charged with the compound material powder (InSb) is put above the cold copper crucible as shown in Figure 2-8. This setup sacrifices one of the advantages of the electron
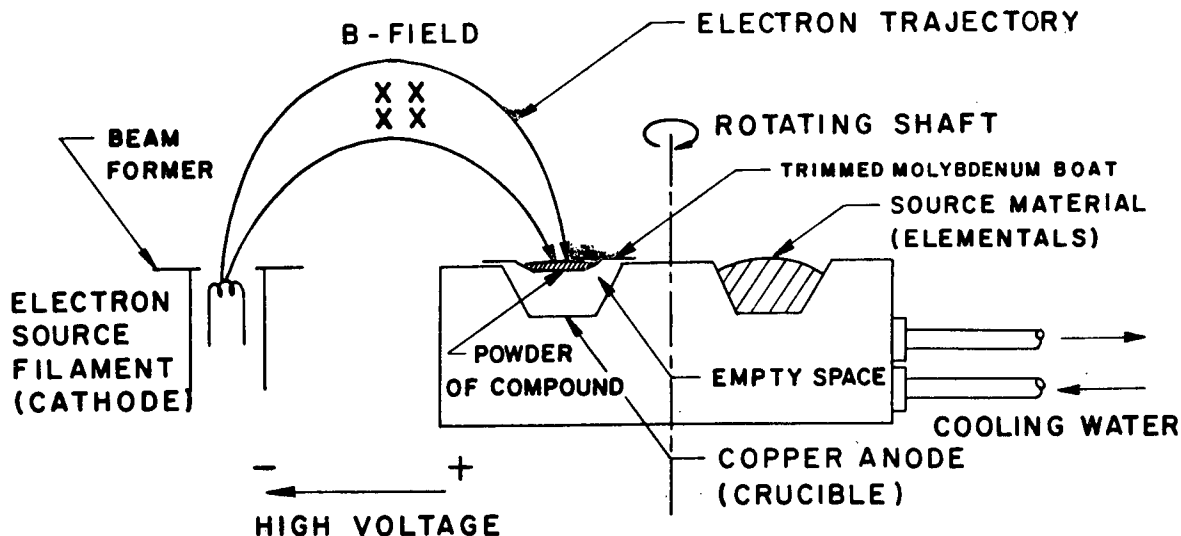
Figure 2-8. Electron Beam Source and Setup for III-V Compound Deposition

beam source, which is the water-cooled cold crucible; however, it is an excellent method of producing high-mobility thin films economically.

About 40 depositions of InSb films, each requiring only a few grams of compound powder, have been made with the original molybdenum boat.

The following shows the method of preparation of high-mobility InSb thin films.

1. Pump the system to a pressure of 3 to 10 x 10^{-7} torr.

2. Outgas the substrate while pumping by increasing the substrate temperature to 400°C.

3. Stabilize the substrate at a temperature between 250 and 300°C.

4. Evaporate the compound powder using the electron gun, maintaining a deposition rate of 10,000 Å/min or faster.

5. Oxidize the deposited films in an air oven at 250°C for 20 to 30 minutes.

6. Recrystallize the films with the oxide surface in a tube furnace which has a uniform 5- to 10-inch heating zone. Argon is passed over the sample at a rate of 2 liters/min. The recrystallization temperature should always be between 522 and 536°C. Time varies from run to run, but about 3 minutes gives good results.

<div align="center">Experimental Results</div>

Significant improvement of the InSb thin-film mobility was attained using the electron beam evaporation technique developed at The University of New Mexico, followed by recrystallization of the thin film. Mobility values obtained by several authors are shown in Figure 2-9 for comparison. Radiation effects will be discussed in Chapter III. The experimental and evaluation procedures are detailed in Appendixes B and C.
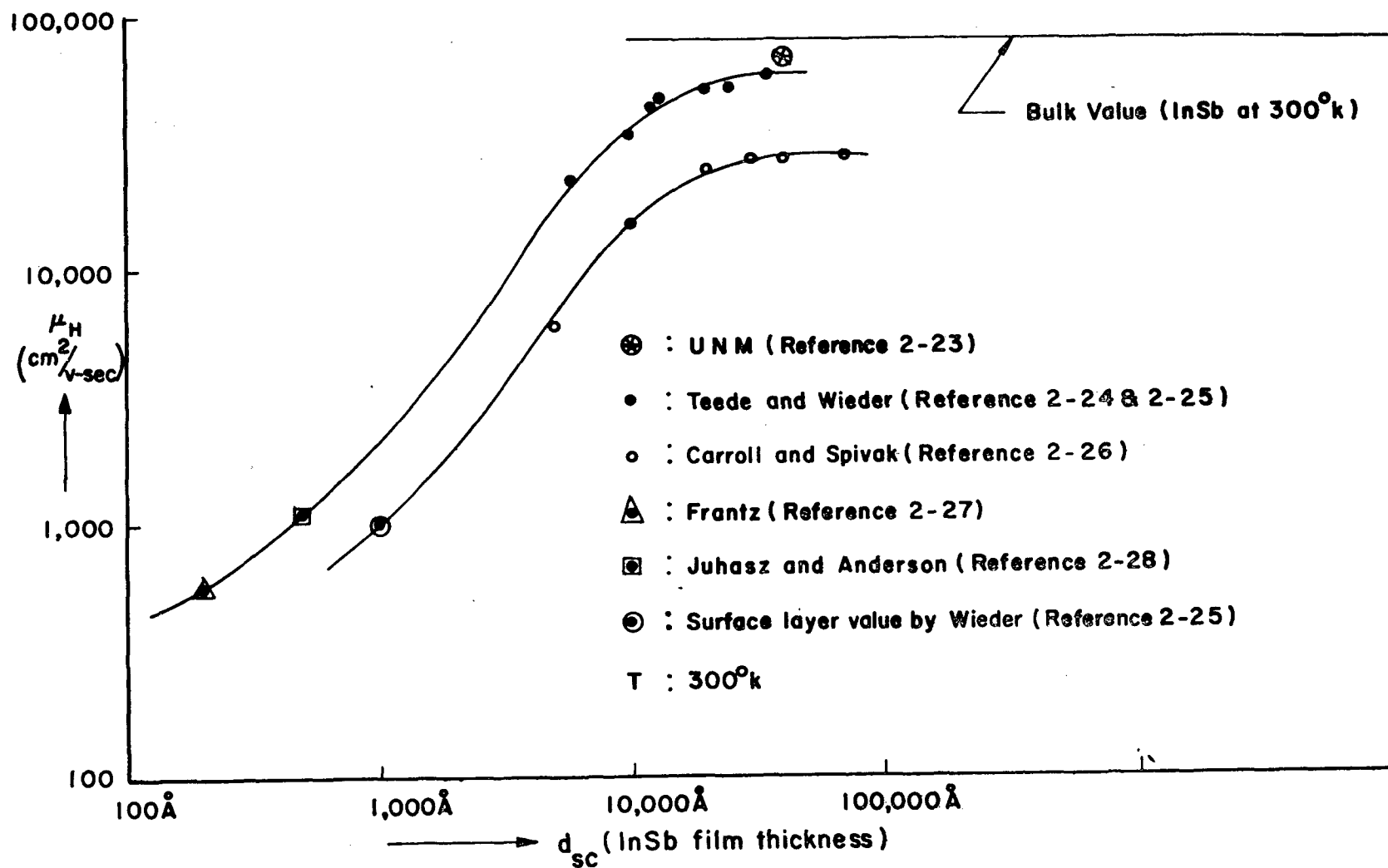
Figure 2-9.   Hall Mobility vs. Film Thickness of InSb at 300°K

2-1. H. Welker, "Über neue halbleitende Verbindungen," *Zeitschrift für Naturforschung*, Vol. 7a, p. 744, 1952.

2-2. H. Welker, "Über neue halbleitende Verbindungen II," *Z. Naturforsch.*, Vol. 8a, p. 248, 1953.

2-3. O. Madelung, *Physics of III-V Compounds*, John Wiley & Sons, N.Y., 1964.

2-4. E. O. Kane, "Band Structure of Indium Antimonide," *The Journal of Physics and Chemistry of Solids*, Vol. 1, p. 249, 1957.

2-5. G. Dresselhaus, "Spin-Orbit Coupling Effects in Zinc Blende Structures," *Physical Review*, Vol. 100, No. 2, p. 580, 1955.

2-6. A. C. Tickle, *Thin-Film Transistors: a new approach to microelectronics*, John Wiley & Sons, N.Y., 1969.

2-7. L. I. Maissel and R. Glang, *Handbook of Thin Film Technology*, McGraw-Hill, N.Y., 1970.

2-8. G. A. Bassett, et al., *Structure and Properties of Thin Films*, John Wiley & Sons, 1959.

2-9. R. Thun, in G. Haas (ed.), *Physics of Thin Films*, Vol. 1, Academic Press, Inc., N.Y., 1964.

2-10. W. Buckel, *Structure and Properties of Thin Films*, John Wiley & Sons, N.Y., 1959.

2-11. W. Mönch, "Über die charakteristische Temperatur Θ_R abschreckend Kondensierter Metallschichten," *Zeitschrift für Physik*, Vol. 170, p. 93, 1962.

2-12. R. Suhrmann and H. Schnackenberg, "Über den Reaktions ablauf beim Übergang reiner Metallschichten aus dem ungeordneten in dem geordneten Zustand," *Z. Physik*, Vol. 119, p. 287, 1949.

2-13. R. Hilsch, in V. D. Fréchette (ed.), *Non-crystalline Solids*, John Wiley & Sons, N.Y., 1958.

2-14. E. Feldtkeller, "Struktur und Widerstand sehr stark gestörter Kupferschichten bei tiefen Temperaturen," *Z. Physik*, Vol. 157, p. 65, 1959.

2-15. W. Ruhl, "Rontgenographische Untersuchungen an Kondensierten Zinnfilmen bei tiefen Temperaturen," *Z. Physik*, Vol. 138, p. 121, 1954.

2-16. C. A. Nevgebauer, in G. Haas and R. Thun (ed.), *Physics of Thin Films*, Vol. II, Academic Press, N.Y., 1964.

2-17. T. W. Kim and W. W. Grannemann, "A Study of Metal-Insulator-Semiconductor Magnetoresistance, Bulk and Surface Properties of Indium Antimonide," Scientific and Technical Aerospace Reports (C26 N71-25377), Vol. 9, No. 13, July 8, 1971.

2-18. T. W. Kim, V. D. Deokar, and W. W. Grannemann, "Electron Beam Evaporated High Mobility Thin-Films of Indium Antimonide," Scientific and Technical Aerospace Reports (C17 N71-35576), Vol. 9, No. 22, November 23, 1971.

2-19. T. W. Kim, V. D. Deokar, and W. W. Grannemann, "Magnetoresistance and Radiation Effects on Electron Beam Evaporated High Mobility Thin-Films of Indium Antimonide," A Radiation Effects Research Program, Bureau of Engineering Research, The University of New Mexico, EE-192(71)ONR-005, September 1971.

2-20. S. Dushman, Scientific Foundations of Vacuum Technique (J. M. Lafferty, ed.), 2nd ed., John Wiley & Sons, N.Y., 1962.

2-21. L. Holland, Thin Film Microelectronics (Holland ed.), Champman and Hall, London, p. 108, 1965.

2-22. J. L. Richard, P. B. Hart, and L. M. Gallone, "Epitaxy of Compound Semiconductors by Flash Evaporation," J. Applied Physics, Vol. 34, p. 3418, 1963.

2-23. T. W. Kim, unpublished data.

2-24. N. F. Teede, "Single Crystal InSb Thin Films by Electron Beam Recrystallization," Solid State Electronics, Vol. 10, p. 1069, 1967.

2-25. H. H. Wieder, "Anomalous Transverse Magnetoresistance of InSb Films," J. Appl. Phys., Vol. 40, No. 8, p. 3320, July 1969.

2-26. J. A. Carroll and J. F. Spivak, "Preparation of High Mobility InSb Thin Films," Solid State Electronics, Vol. 9, p. 383, 1966.

2-27. V. L. Franz, "Indium Antimonide Thin Film Transistor," Proc. IEEE, Vol. 53, p. 760, July 1965.

2-28. C. Juhasz and J. C. Anderson, J. British Inst. of Radio and Electronic Eng., Vol. 33, p. 223, 1967.

CHAPTER III

RADIATION EFFECTS ON HALL AND MAGNETORESISTANCE DEVICES
OF InSb BULK AND THIN FILMS

The Hall Effect

The Hall effect is one of the most important features for deter-
mining carrier concentration and carrier mobility of any conducting ma-
terial. It has affected detailed semiconductor studies, particularly
the determination of low-temperature carrier concentrations. The slope
of the carrier concentration versus reciprocal temperature curve is re-
lated to the ionization energy of the electrically active impurities in
extrinsic semiconductors (References 3-1, 3-2, and 3-3).
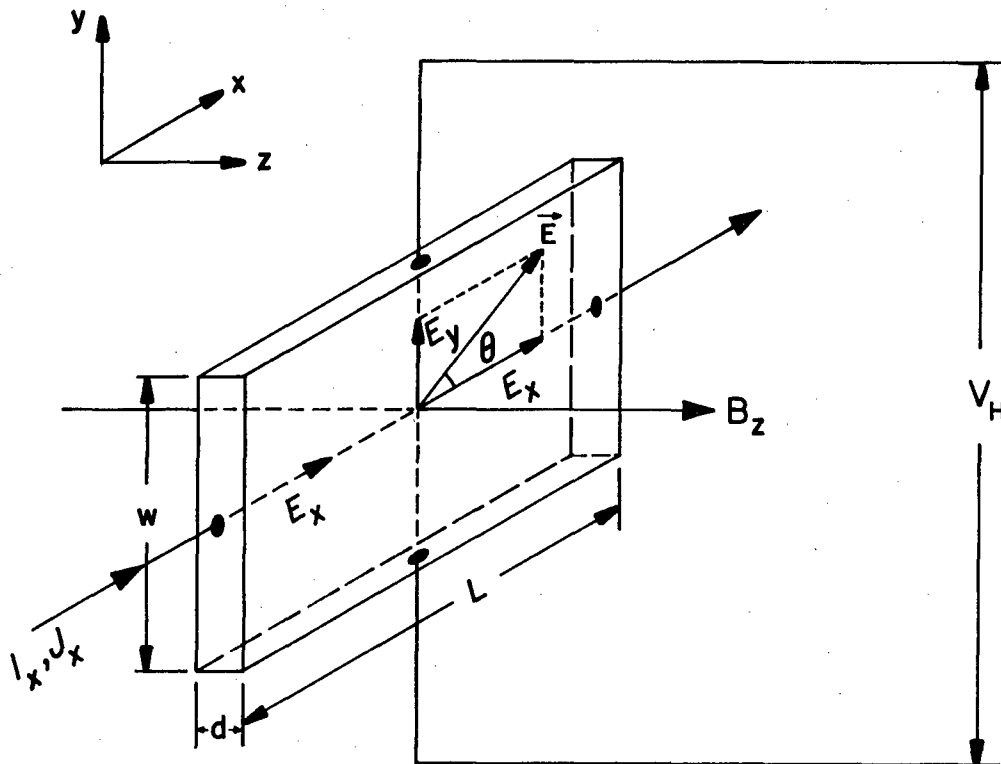
Figure 3-1. Rectangular Hall Effect Device

The basic principles of Hall effect are illustrated by application
of the Lorentz force to moving charges in a free-electron system (Figure
3-1). The total force on a charged particle in an electric and magnetic
field is given by the vector equation

$$\vec{F} = e[\vec{E} + \vec{V} \times \vec{B}]$$

where

$\vec{F}$ = force

e = electron charge

$\vec{V}$ = velocity of the particle

$\vec{E}$ = electric field

$\vec{B}$ = magnetic flux density

If a rectangular slab with a current I_x in the x-direction is inserted in a uniform magnetic flux density B_z in the z-direction, then an electric Hall field E_y (or Hall voltage V_H) is developed in the y-direction until the force which it exerts on a charged particle counterbalances that resulting from the magnetic field. Then subsequent particles of the same charge and velocity are no longer deflected, and a steady state exists. The Hall field can be expressed as

$$E_y = \frac{J_x B_z}{en} = -\frac{1}{en}(\vec{J} \times \vec{B})_y = \frac{1}{en}(\vec{B} \times \vec{J})_y$$

where

J_x = electric current density in x-direction

$J_x = env_x$

v_x = velocity of particles in x-direction

B_z = magnetic flux density in z-direction

Now the Hall coefficient R_H is defined by the ratio $E_y/J_x B_z$

$$R_H = \frac{E_y}{J_x B_z} = \frac{1}{en} \tag{3-1}$$

and

$R_H > 0$ for conduction by holes

$R_H < 0$ for conduction by electrons

In a real semiconductor, the idealized free-particle treatment no longer applied; therefore, the distribution of velocities and the interaction of the charge carriers with impurities, defects, and lattice thermal vibration of the semiconductor must be taken into account. Considering most of the complexities just mentioned, an expression similar to Equation 3-1 is obtained as

$$R_H = \frac{r}{en}$$

where

r = Hall coefficient factor

The parameter r depends on the nature of the scattering, the band structure, the magnetic field strength, and on the statistics characterizing the distribution of velocities of the carriers. Smith (Reference 3-4) expressed r as

$$r \equiv \frac{<\tau^2>}{<\tau>^2} = \frac{\text{Hall mobility}}{\text{conductivity mobility}} = \frac{\mu_H}{\mu} = \frac{R_{HB \rightarrow 0}}{R_{HB \rightarrow \infty}}$$

where

τ = relaxation time due to scattering or mean free time between carrier collisions, which depends on the carrier energy, e.g., for semiconductors with spherical constant energy surfaces
$\tau \sim E^{1/2}$ for phonon scattering
$\tau \sim E^{3/2}$ for ionized impurity scattering
and, in general, $\tau = aE^{-S}$ where a and S are constants

For the phonon scattering, the ratio r is

$$r = \frac{3\pi}{8} \simeq 1.178$$

For the ionized impurity scattering,

$$r = \frac{315\pi}{512} \simeq 1.93$$

31

In most cases, its value differs from unity by less than ±50 percent. The fact that r approaches unity in the limit of strong magnetic fields provides a means for experimental determination if measurements can be made into the strong-field limit. Another point to note is that r is unity for very large carrier concentrations—i.e., large degeneracy. Those charge carriers with velocity in the neighborhood of the Fermi velocity contribute significantly to conduction, and the characteristics of the single-velocity picture are obtained (Reference 3-3).

From Figure 3-1, the Hall angle can be defined as

$$\theta = \tan^{-1} \frac{E_y}{E_x} \qquad (3-2)$$

Thus the Hall effect can be described as a rotation (θ) of the electric field—a concept which is very useful. The rotation aspect of the Hall effect is also brought out by considering the components of the conductivity tensor, which relate electric current densities and fields. For the boundary condition that $J_z = 0$, we have

$$J_x = \sigma_{xx} E_x + \sigma_{xy} E_y$$

$$J_y = -\sigma_{xy} E_x + \sigma_{xx} E_y \qquad (3-3)$$

$$J_z = 0$$

Since

$$\begin{bmatrix} J_x \\ J_y \\ J_z \end{bmatrix} = \begin{bmatrix} \sigma_{xx} & \sigma_{xy} & \sigma_{xz} \\ \sigma_{yx} & \sigma_{yy} & \sigma_{yz} \\ \sigma_{zx} & \sigma_{zy} & \sigma_{zz} \end{bmatrix} \begin{bmatrix} E_x \\ E_y \\ E_z \end{bmatrix}$$

The above equation holds for media of sufficient symmetry that $\sigma_{xx} = \sigma_{yy}$ and $\sigma_{xz} = \sigma_{yz} = \sigma_{zz} = 0$. This is satisfied in isotropic media, and it also holds for a cubic system when the coordinate axes are along the cube axes. For certain symmetric conditions,

$$\sigma_{xy}(B) = -\sigma_{yx}(B) \tag{3-4}$$

Although the validity of the relation (Equation 3-4) is dependent on a certain symmetry in the solid, it should be pointed out that the general Onsager relationships (Reference 3-5) are applicable to the elements of the conductivity tensor, regardless of the degree of isotropy of the material, yielding the general relation

$$\sigma_{iK}(B) = \sigma_{Ki}(-B)$$

Two useful items of information follow from the above Onsager relation.

$$\sigma_{ii}(B) = \sigma_{ii}(-B)$$

$$\sigma_{xy}(B) = -\sigma_{xy}(-B)$$

That is, the diagonal elements of the conductivity tensor contain only even powers of B; the off-diagonal elements, in the case of adequate symmetry, contain only odd powers of B. Since the boundary conditions for Hall coefficient measurement require that J_y vanish, it is derived from Equations 3-2 and 3-3 that

$$\sigma_{xy} = \sigma_{xx} \tan\theta \quad \left(\text{or } \tan\theta = \frac{\sigma_{xy}}{\sigma_{xx}}\right)$$

Also, from the definition of the Hall coefficient as given by Equation 3-1,

$$R_H = \frac{\sigma_{xy}}{\sigma_{xx}^2} \frac{1}{B_z} \tag{3-5}$$

in weak magnetic fields.

The conductivity mobility is related to the conductivity σ by

$$\mu = \frac{\sigma}{en} \tag{3-6}$$

in the case of conduction by a single type of carrier.

33

The Hall mobility is defined as

$$\mu_H \equiv \frac{\tan\theta}{B_z} = R_H \sigma \quad (\text{or } \tan\theta = \mu_H B_z) \tag{3-7}$$

Now, it can be seen that the ratio of Hall mobility and conductivity mobility is precisely the Hall coefficient factor r. Also, from Equation 3-7, it follows that the Hall angle is proportional to the mobility as well as to the magnetic field. Therefore, to achieve large Hall effect or magnetoresistance effect at a reasonable magnetic field, materials with large charge-carrier mobilities must be favored. It is convenient to express the magnetic field conditions as

$$\mu_H B_z \ll 1 \quad \text{for weak magnetic field}$$

$$\mu_H B_z \gg 1 \quad \text{for strong magnetic field}$$

For a rectangular semiconductor slab, as shown in Figure 3-1, the Hall field is expressed as

$$E_y = \frac{J_x B_z}{e} \frac{r(P - nb^2)}{(P + nb)^2} \tag{3-8}$$

where

$$J_x \equiv \sigma E_x$$

$$J_y = J_{ye} + J_{yh} + \sigma E_y = 0$$

$$\sigma = e(n\mu_e + P\mu_h)$$

$$r \equiv \frac{\mu_{Hh}}{\mu_h} = \frac{\mu_{He}}{\mu_e}$$

$$b \equiv \frac{\mu_e}{\mu_h}$$

The Hall voltage is

34

$$V_H = \frac{I_x B_z r}{ed} \frac{b^2 n - P}{(bn + P)^2} \tag{3-9}$$

where

I_x = current flow in the x-direction

d = slab thickness

and the Hall coefficient is

$$R_H = \frac{r}{q} \frac{P - b^2 n}{(P + bn)^2} \tag{3-10}$$

For an n-type semiconductor, n is greater than P and

$$R_H = -\frac{r}{en}$$

For a p-type semiconductor, P is greater than n and

$$R_H = +\frac{r}{eP}$$

In InSb, the n-type is particularly important so that some of the useful expressions will be calculated as

$$V_H = \frac{I_x B_z r}{end} \tag{3-11}$$

$$n = \frac{I_x B_z r}{edV_H} \tag{3-12}$$

$$\sigma = en\mu_e \tag{3-13}$$

$$\mu_{He} = \frac{V_H d\sigma}{B_z I_x} \tag{3-14}$$

The value r corresponds to the ratio of Hall to conductivity mobility and is expressed as

$$r = \frac{R_{H(B\to 0)}}{R_{H(B\to\infty)}}$$

The net donor concentration, $N_D - N_A$, has been calculated in all cases from

$$R_{H0} = \frac{r}{ne}$$

to eliminate uncertainty in scattering (Reference 3-6). Similarly the Hall mobility defined by $\mu_{He} = \sigma_o R_{H0}$ has been calculated using the weak field Hall voltage from

$$\mu_{He} = \frac{V_{H(B\to 0)}}{V_{ab}} \left(\frac{L}{W}\right) \frac{1}{B_z} \qquad (3\text{-}15)$$

where

> V_{ab} = applied voltage measured between potential probes a and b
>
> $\left(\frac{L}{W}\right)$ = length-to-width ratio

Secondary effects considered in the interpretation of DC Hall effect measurements are the transverse magnetoresistive effect, the Nernst effect, the Ettingshausen effect, and the Righi-Leduc effect. The transverse magnetoresistive effect is an increase in the resistivity due to the curvature of the trajectories of the charge carriers and, thus, a net increase in the average drift distance along the direction of current flow between successive collisions, when the current-carrying slab is placed in a transverse magnetic field. The magnetoresistive effect can be compensated for by maintaining constant current through the slab. The last three effects are thermomagnetic ones which are due to thermal gradients in the Hall slab (References 3-1, 3-7, 3-8, and 3-9). These four effects are normally small; therefore, they will be ignored.

Sheet Resistance and Resistivity

The resistance of the slab is defined by

$$R = \rho \left(\frac{L}{W}\right) \cdot \frac{1}{d}$$

If L = W, this then becomes the sheet resistance,

$$R_S = \frac{\rho}{d} \quad \text{in ohms per square}$$

so that the resistance R_S of one square of film is independent of the size of the square and dependent only on resistivity and thickness. If the thickness is known, the resistivity is readily obtained from

$$\rho = R_S d$$

The sheet resistivity can be calculated using the following methods.
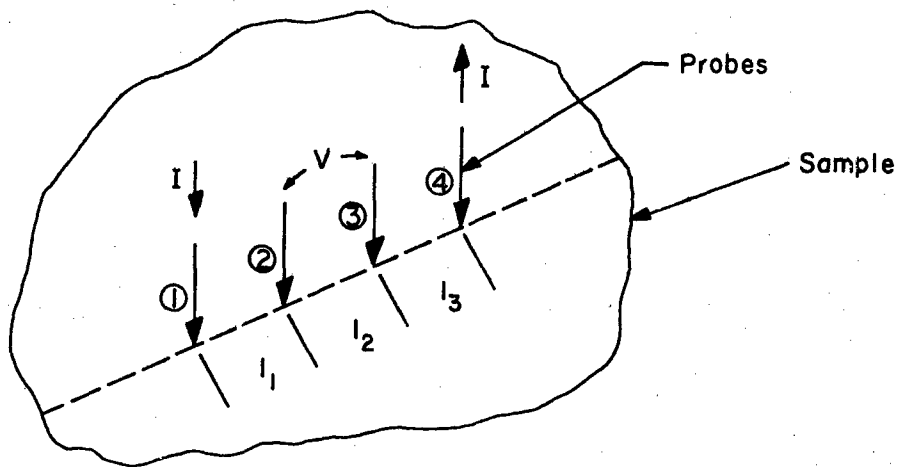
Figure 3-2. In-Line Four-Point Probe

In-Line Four-Point Probe Method -- The most common four-point probe method is the in-line type illustrated schematically in Figure 3-2. The resistivity for semi-infinite volume (Reference 3-10) is given by

$$\rho = \frac{V}{I} \frac{2\pi}{\dfrac{1}{\ell_1} + \dfrac{1}{\ell_3} - \dfrac{1}{\ell_1 + \ell_2} - \dfrac{1}{\ell_2 + \ell_3}}$$

If the material on which the probes are placed is an infinitely thin slice resting on an insulating support and $\ell_1 = \ell_2 = \ell_3 = \ell$, then the resistivity becomes

$$\rho = \frac{V}{I} \frac{\pi d}{\ell n 2} = 4.532 \left(\frac{V}{I}\right) d \tag{3-16}$$

37

Hence, the sheet resistance is expressed as

$$R_S = 4.532 \left(\frac{V}{I}\right)$$

(3-17)

Although Equations 3-16 and 3-17 are independent of the probe spacing, the resolution of any particular probe will depend on spacing. Thus, a probe of spacing ℓ centrally located inside a square of film measuring $6\ell \times 6\ell$ will give a reading that is about 20 percent too high if the square is surrounded by an insulating film and about 10 percent too low if it is surrounded by a film of infinite conductivity. More exact corrections for edge effects are described in Reference 3-10.

Square Four-Point Probe Method -- In a case where very high resolution is needed, a square-probe array such as shown in Figure 3-3,
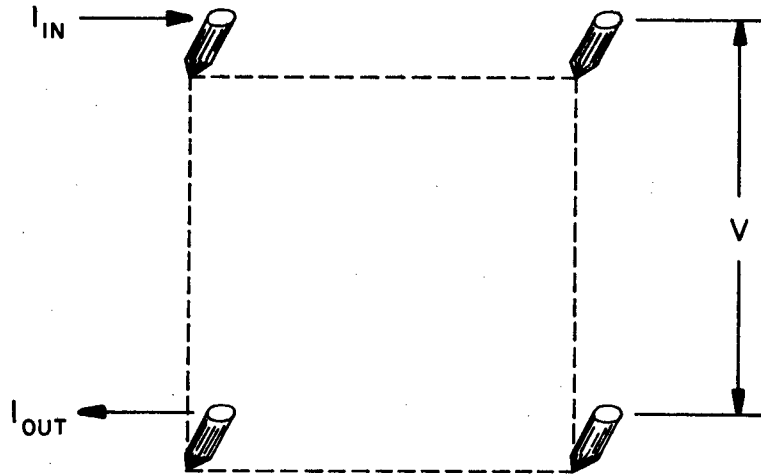
Figure 3-3. Square Four-Point Probe

rather than a linear one, may be used. To use such a probe, current I is fed through any two adjacent probes and the voltage V generated across the other two is measured. The resistivity and sheet resistivity are given by

$$\rho = \frac{2\pi d}{\ell n 2}\left(\frac{V}{I}\right) = 9.06d\left(\frac{V}{I}\right)$$

(3-18)

$$R_S = 9.06\left(\frac{V}{I}\right)$$

(3-19)

For very small probes, the average of two independent measurements using different pairs of current probes may be utilized. It is estimated that by this means a probe whose geometry deviates from a square by about 7 percent can be made to read to an accuracy of about 1 percent (Reference 3-11).

A flat disk of arbitrary shape with contacts 1, 2, 3, and 4 in successive order fixed at arbitrary places along the circumferences is considered and shown in Figure 3-4 (Reference 3-12). A resistance
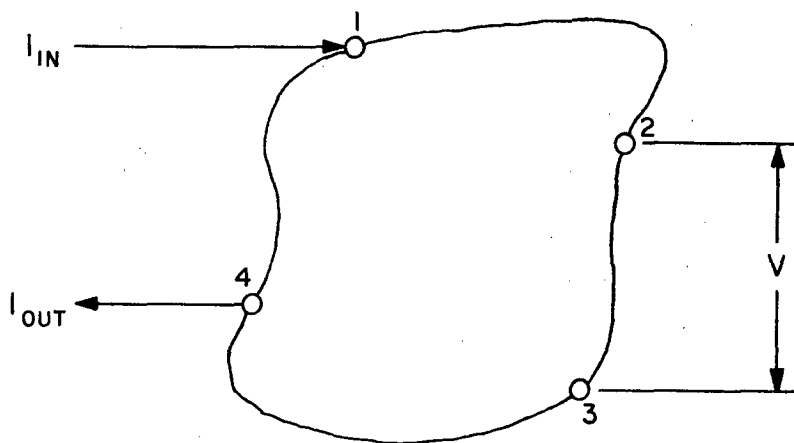
Figure 3-4. Disk of Arbitrary Shape

$R_{12,34}$ is defined as the potential difference V_{34} between contacts 3 and 4 divided by unit current through contacts 1 and 2. Similarly the resistance $R_{23,41}$ can be defined as the potential difference V_{41} between contacts 4 and 1 divided by unit current through contacts 2 and 3. The resistivity of the sample as derived by van der Pauw is then

$$\rho = \frac{\pi d}{\ell n 2} \frac{R_{12,34} + R_{23,41}}{2} f(R_{12,34}/R_{23,41})$$

where f is a function of the ratio $R_{12,34}/R_{23,41}$ only and satisfies the relation

$$f = \frac{R_{12,34} - R_{23,41}}{R_{12,34} + R_{23,41}} \left\{ \cosh^{-1} \frac{\exp\left(\frac{\ell n 2}{f}\right)}{2} \right\}^{-1}$$

For the square geometry, the resistivity becomes

39

$$\rho = \frac{\pi d}{\ln 2} R_{12,34} \qquad (3\text{-}20)$$

since $f = 1$ and $R_{12,34} = R_{23,41}$ for the square geometry.

Four-Point Probe Hall Effect Device

The Hall mobility can be determined by measuring the change of the resistance $R_{24,13}$ when a magnetic field is applied perpendicular to the sample, as shown in Figure 3-4 (Reference 3-13). The Hall mobility is then given by

$$\mu_H = \frac{d}{B_z} \frac{1}{\rho} \Delta R_{24,13}$$

where

$$\Delta R_{24,13} = \text{change of the resistance } R_{24,13} \text{ due to } B_z$$
$$= R_{24,13}(B_z) - R_{24,13}(0)$$

For the square geometry, the Hall mobility is expressed as

$$\mu_{H\diamond} = \frac{0.221}{B_z} \frac{(\Delta V_{24}/I_{13})}{(V_{12}/I_{34})}$$

If $I_{13} = I_{34}$, $V_{12} = (V_{12} + V_{23} + V_{34} + V_{41})/4 \equiv V_{\square}$ and $\Delta V_{24} = \Delta V_{H\diamond} = V_H(B_z) - V_H(0)$, then the Hall mobility is given by

$$\mu_H = 0.221 \frac{\Delta V_{H\diamond}}{B_z V_{\square}} \times 10^4 \text{ cm}^2/\text{V-sec} \qquad (3\text{-}21)$$

for B_z in Wb/m^2 and $\Delta V_{H\diamond}$ in volts.

Five-Point Probe Hall Effect Device

The Hall mobility of the five-point probe Hall device shown in Figure 3-5 is calculated by using the formula (Reference 3-13) from Equation 3-15

$$\mu_H = \left(\frac{L}{W}\right) \frac{V_H}{V_{ab} B_z} \qquad (3\text{-}22)$$
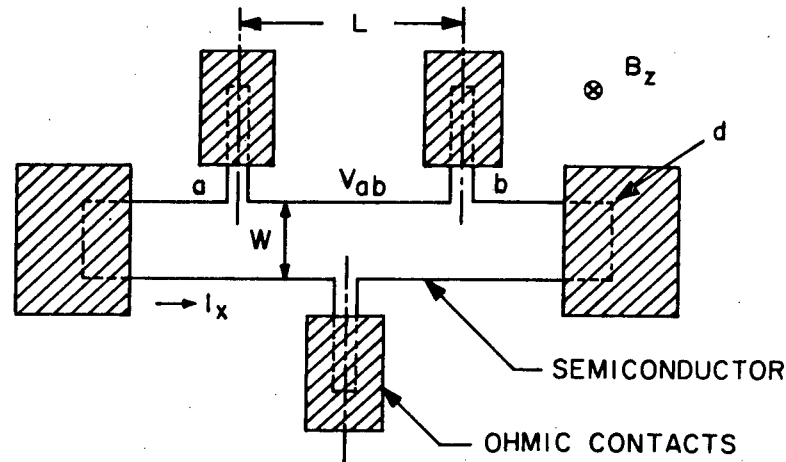
Figure 3-5. Five-Point Probe Hall Device

since

$$\mu_H = \left| R_H \sigma \right|$$

$$R_H = \frac{V_H d}{I_x B_z}$$

$$\sigma = \frac{I_x L}{V_{ab} W d}$$

The Magnetoresistance Effect

When a current-carrying rectangular slab is placed in a transverse magnetic field, the resistance (or resistivity) of the slab increases monotonically with increasing value of B_z, due to the curvature of the trajectories of the charge carriers. This is known as the transverse magnetoresistance effect. The transverse magnetoresistivity of a solid is defined as E_x/J_x for the standard geometry of Figure 3-1. In principle, the resistivity is independent of the magnetic field; however, experiments generally show a resistivity which increases as the magnetic field is increased (Reference 3-14).

The calculation of the magnetoresistance is somewhat complicated; however, the magnetoresistance of a rectangular isotropic slab was derived by Lippmann and Kuhrt (Reference 3-15) by conformal mapping and boundary value problem approach in terms of Hall angle, the resistivity

in a magnetic field, the corresponding resistivity in zero field, and a function of g(L/W), evaluated numerically and graphically. To derive the magnetoresistance coefficient, the following differential equations for the complex planes must be solved using the boundary conditions.

$$\tan\theta = -\frac{E_x}{E_y}\bigg|_{x=\pm\frac{W}{2}} = -\left[\frac{\frac{\partial\phi}{\partial x}}{\frac{\partial\phi}{\partial y}}\right]_{x=\pm\frac{W}{2}}$$

(3-23)

$$\tan\theta = \sigma R_H B$$

Because the conformal mapping is a standard method for solving boundary value problems in potential theory, the x-y coordinates in Figure 3-6 are transformed into the complex z-plane (z = x + iy) in Figure 3-7, the z-plane is transformed into the simple ζ-plane ($\zeta = \xi + i\eta$) in Figures 3-8 and 3-9, and then the ζ-plane is again transformed into the w-plane (w = u + iv) in Figure 3-10.

The boundary conditions are

1. Inside the slab,

    $$\Delta\phi(x,y) = 0$$

2. At electrodes,

    $$\phi(x,o) = V$$

    $$\phi(x,L) = 0$$

3. For the regions $-(W/2) \leq x \leq +(W/2)$ and y = 0,

    $$-1 \leq \xi \leq +1 \quad \text{and } \eta = 0$$

4. For the regions $-(W/2) \leq x \leq +(W/2)$ and y = L,

    $$\frac{1}{k} \leq \xi \leq \infty$$

    $$-\infty \leq \xi \leq -\frac{1}{k} \quad \text{and } \eta = 0$$

42
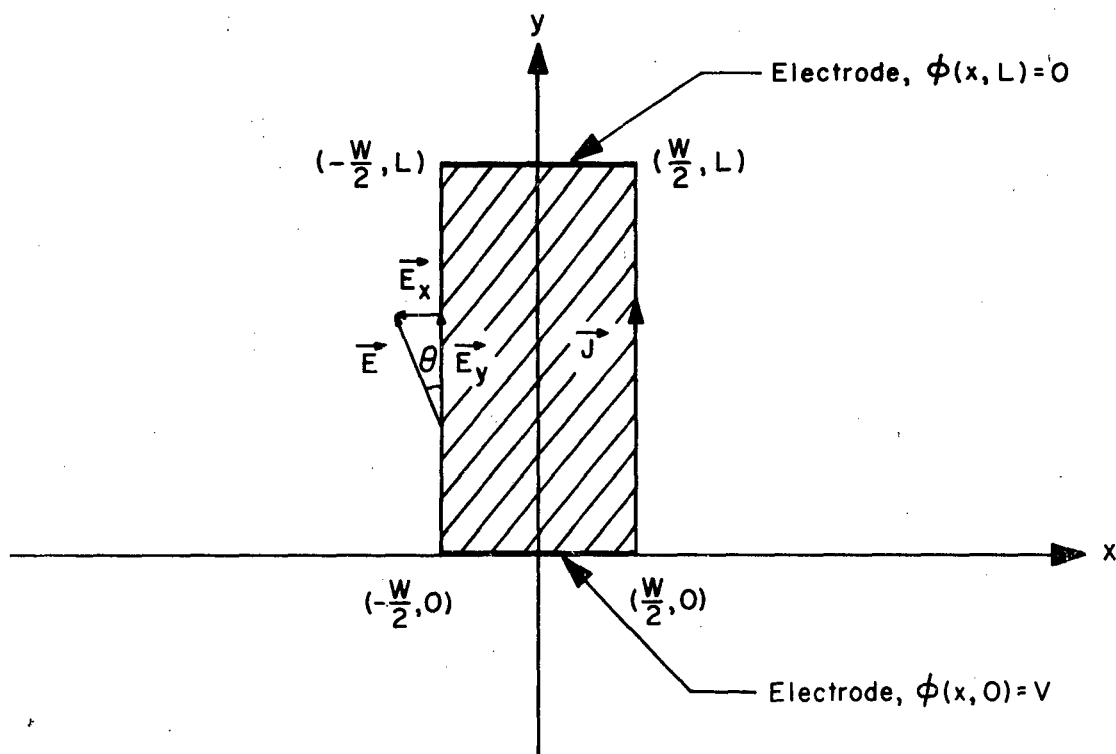
Figure 3-6. Electrodes and Geometry of a Rectangular Slab
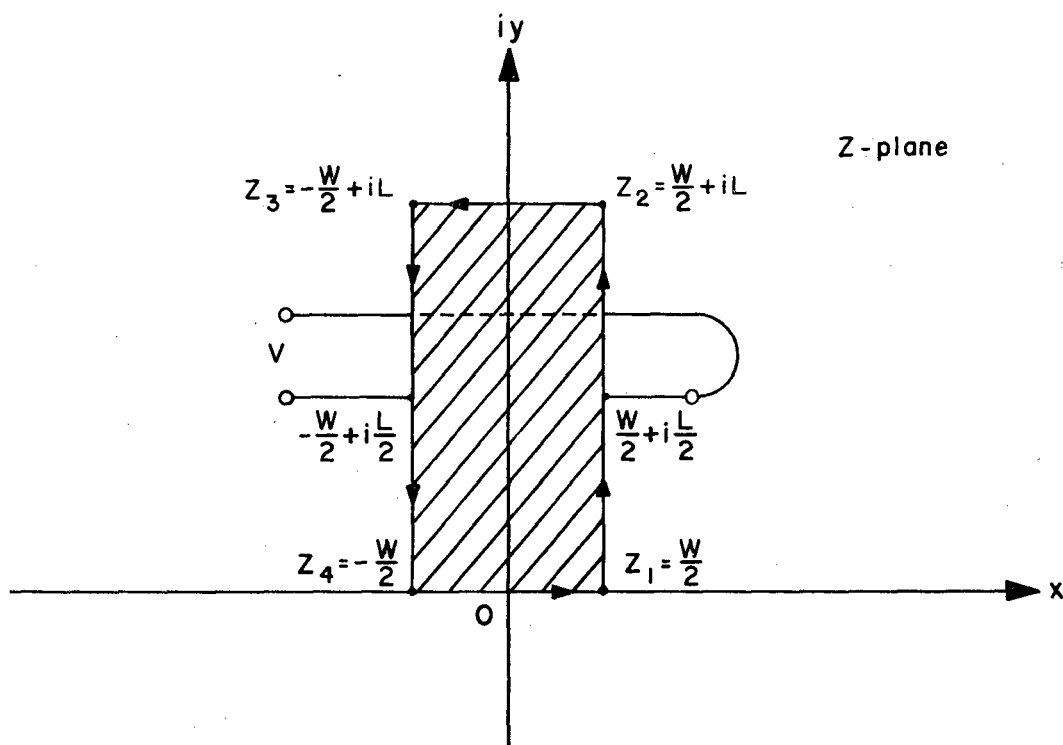
Figure 3-7. A Rectangular Slab Transformed into z-plane
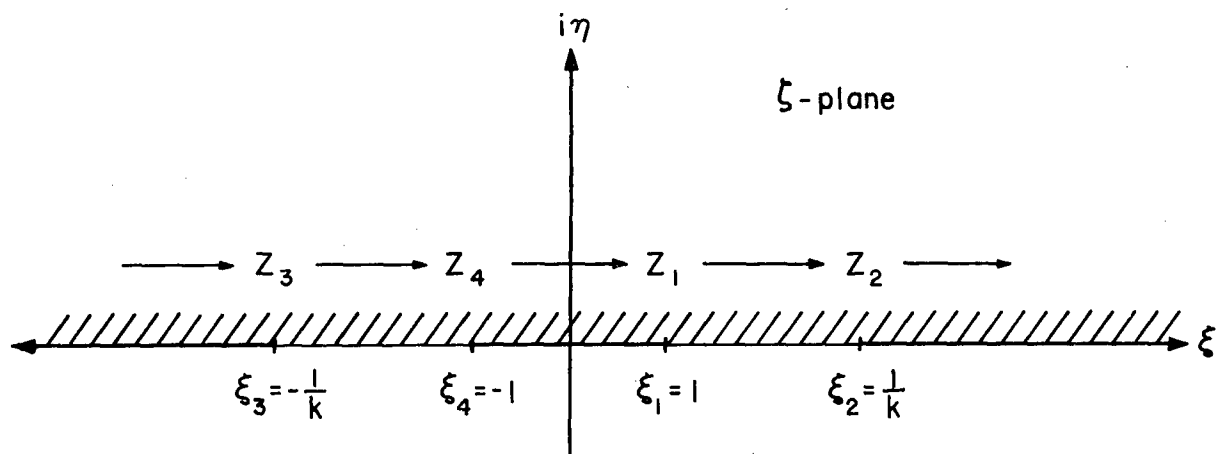
Figure 3-8. Representation of ζ-plane Transformation
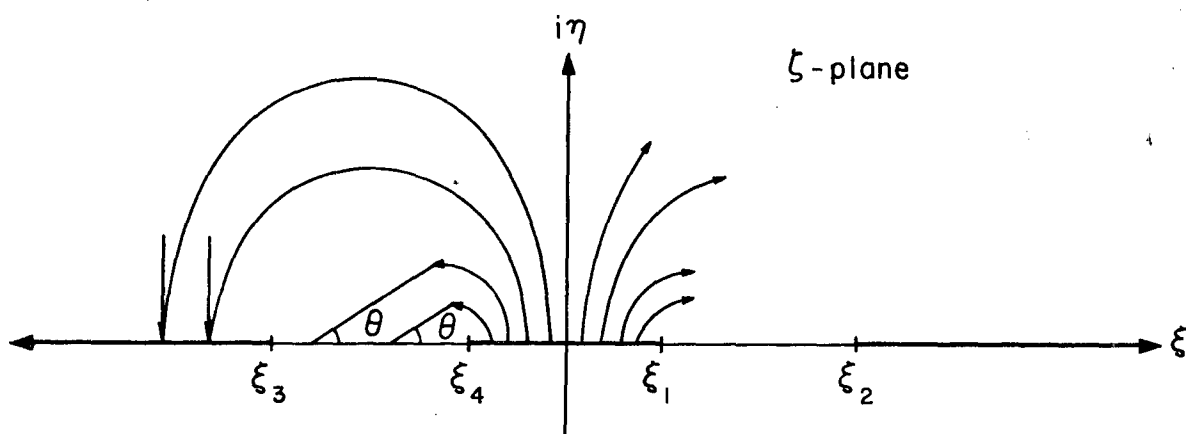
Figure 3-9. Sketch of Field Lines in the ζ-plane
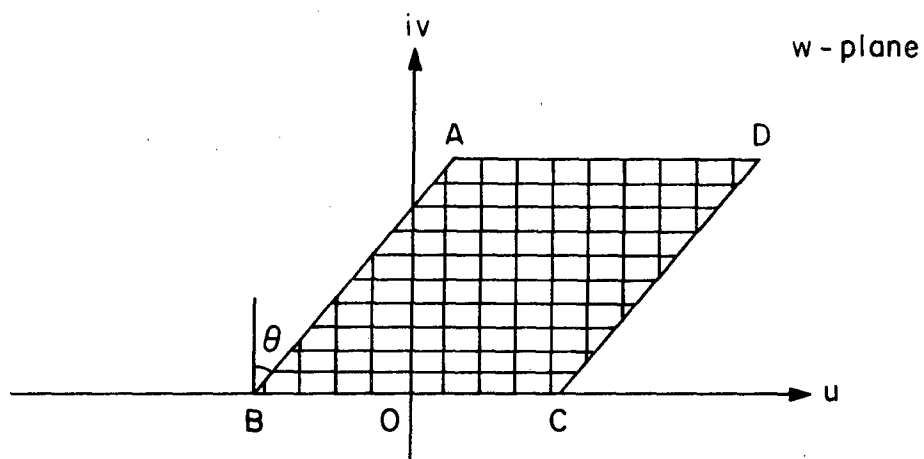
Figure 3-10. Field and Equipotential Lines in the ω-plane

where

  k = parameter decided by the geometry

5. For the region $-1 \leq \xi \leq 1$,

  $v(\xi, o) = V$

6. For the regions $1/k \leq \xi \leq \infty$ and $-\infty \leq \xi \leq -(1/k)$,

  $v(\xi, o) = 0$

7. For the regions $-(1/k) \leq \xi \leq -1$ and $1 \leq \xi \leq 1/k$,

$$- \begin{bmatrix} \dfrac{\partial v}{\partial \eta} \\ \dfrac{\partial v}{\partial \xi} \end{bmatrix} = \sigma R_H B$$

From the solution to the above equation, the transverse magnetoresistance can be derived as

$$R(B) = \frac{V}{I} = \frac{1}{d\sigma(B)} \frac{1}{\cos\theta} \frac{Z}{N} \qquad (3\text{-}24)$$

where

$$V = \int_1^{1/k} |E| \cos\theta d\xi = \cos\theta c'Z$$

$$|E| = \frac{c'}{\left| (\xi - 1)(\xi + \frac{1}{k}) \right|^{\frac{1}{2} - \frac{\theta}{\pi}} \cdot \left| (\xi + 1)(\xi - \frac{1}{k}) \right|^{\frac{1}{2} - \frac{\theta}{\pi}}}$$

$$Z = \int_1^{1/k} \frac{|E| d\xi}{c'}$$

$$I = d \int_{-1}^{+1} J d\xi = d\sigma \cos^2\theta \int_{-1}^{+1} |E| d\xi$$

$$J = \cos\theta |E| d$$

$$N = \int_{-1}^{+1} \frac{|E| d\xi}{c'}$$

d = thickness of the slab

c' = constant

For the cases of large L/W and small L/W, the parameter k is given by

$$k = 1 - 8 \, e^{-(\frac{\pi}{2})(\frac{W}{L})} \qquad \text{for } 0 \leq \frac{L}{W} \leq 0.35$$

$$k = 4 \, e^{-\pi(\frac{L}{W})} \qquad \text{for } 0.85 \leq \frac{L}{W} \leq \infty$$

The accuracy is 1 percent, and the relation between k and L/W is shown in Figure 3-11.
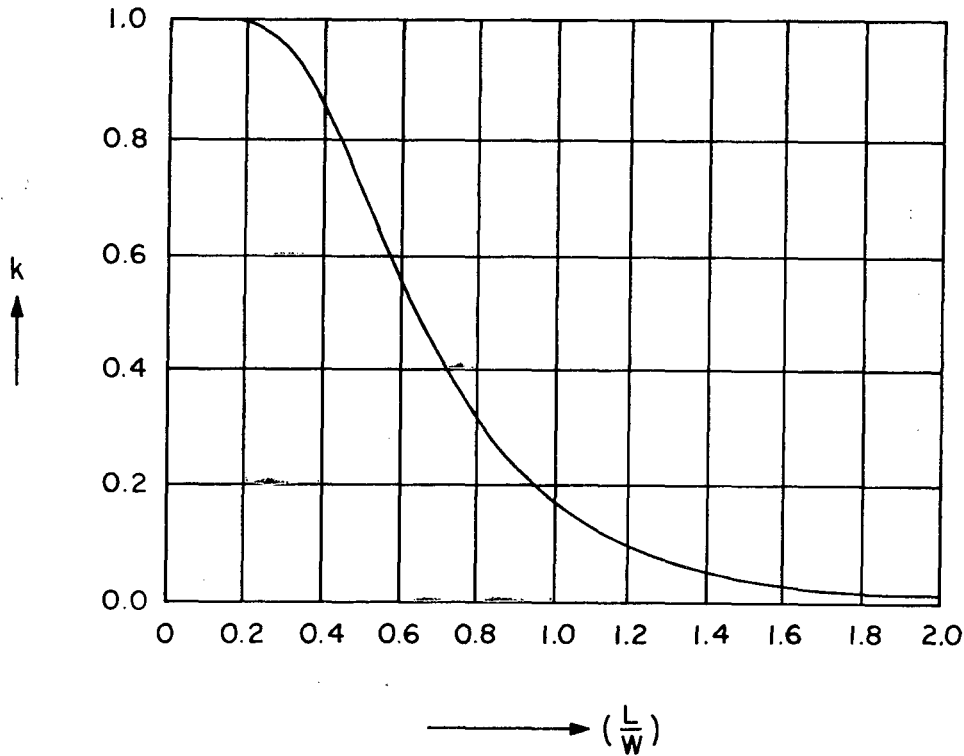
Figure 3-11. k vs. (L/W) Curve

It is important to evaluate Equation 3-24 and discuss the expressions derived from the above equations because they involve some of the significant results. In order to discuss the magnetoresistance effects, the magnetoresistance ratio r(B), the physical magnetoresistance ratio $r_\infty(B)$, the total magnetoresistance coefficient $(\Delta R/R_o)$, and the physical magnetoresistance coefficient $(\Delta R/R_o)_p$ are defined as

$$r(B) \equiv \frac{R(B)}{R(0)} \tag{3-25}$$

$$r_\infty(B) \equiv \frac{\sigma(0)}{\sigma(B)} = \frac{\rho(B)}{\rho(0)} \tag{3-26}$$

$$\left(\frac{\Delta R}{R_o}\right) = r(B) - 1 = \frac{R(B) - R_o}{R_o} \tag{3-27}$$

$$\left(\frac{\Delta R}{R_o}\right)_p = r_\infty(B) - 1 = \left(\frac{\Delta\rho}{\rho_o}\right)_p \tag{3-28}$$

The $r_\infty(B)$ and $\left(\Delta R/R_o\right)_p$ are in general determined by the material properties but not by the geometry.

Magnetoresistance of the Square Geometry

For the square geometry, the length-to-width ratio becomes unity and the k value is $3-\sqrt{8}$; therefore, the magnetoresistance R(B) is

$$R(B) = \frac{1}{d\sigma(B)} \sqrt{1 + \tan^2\theta}$$

$$r(B) = \frac{\sigma(0)}{\sigma(B)} \sqrt{1 + \tan^2\theta}$$

$$\left(\frac{\Delta R}{R_o}\right) = \frac{\sigma(0)}{\sigma(B)} \sqrt{1 + \tan^2\theta} - 1$$

For weak magnetic field $0 \leq \theta \leq 0.45$,

$$r(B) = \frac{\sigma_o}{\sigma_B}(1 + \frac{1}{2}\theta^2) \quad \text{(quadratic)}$$

$$\left(\frac{\Delta R}{R_o}\right) = \left(\frac{\Delta\rho}{\rho_o}\right) + \frac{1}{2}\frac{\sigma_o}{\sigma_B}\theta^2$$

For strong magnetic field $\tan\theta \gg 1$,

$$r(B) = \sigma_o R_H B \quad \text{(linear)}$$

$$\left(\frac{\Delta R}{R_o}\right) = \sigma_o R_H B - 1$$

Magnetoresistance for Low Magnetic Field ($0 \leq \theta \leq 0.45$)

For low magnetic field, the geometry-dependent magnetoresistance is expressed as

$$R(B) = \frac{1}{d\sigma_B} \frac{L}{W} \{1 + \theta^2 g(\frac{L}{W})\}$$

$$r(B) = \frac{\sigma_o}{\sigma_B} \{1 + \theta^2 g(\frac{L}{W})\}$$

$$\left(\frac{\Delta R}{R_o}\right) = \frac{\sigma_o}{\sigma_B} \{1 + \theta^2 g(\frac{L}{W})\} - 1$$

where

$g(\frac{L}{W})$ = geometric function determined by conformal mapping

$\tan\theta \simeq \theta$ for small θ

If $\sigma_o/\sigma_B = \mu_o/\mu_B$ and $\tan^2\theta = (\mu_B B)^2$ (Reference 3-16), then

$$r(B) = \frac{\mu_o}{\mu_B} + g(\frac{L}{W}) \mu_o \mu_B B^2 \tag{3-29}$$

$$\left(\frac{\Delta R}{R_o}\right) = \left(\frac{\Delta \mu}{\mu_B}\right)_p + g(\frac{L}{W}) \mu_o \mu_B B^2 \tag{3-30}$$

where $(\Delta\mu/\mu_B)_p$ is a physical magnetoresistance coefficient $(\Delta\rho/\rho_o)_p$ which may be considered negligible im small magnetic fields in comparison with the geometric magnetoresistance which is quadratic in B.

The geometric coefficient versus length-to-width ratio curves are plotted in Figure 3-12. Particularly, if the ratio (L/W) approaches zero, the magnetoresistances are equal to the Corbino disks.

$$r(B) = \frac{\mu_o}{\mu_B}(1 + \mu_B^2 B^2) \tag{3-31}$$
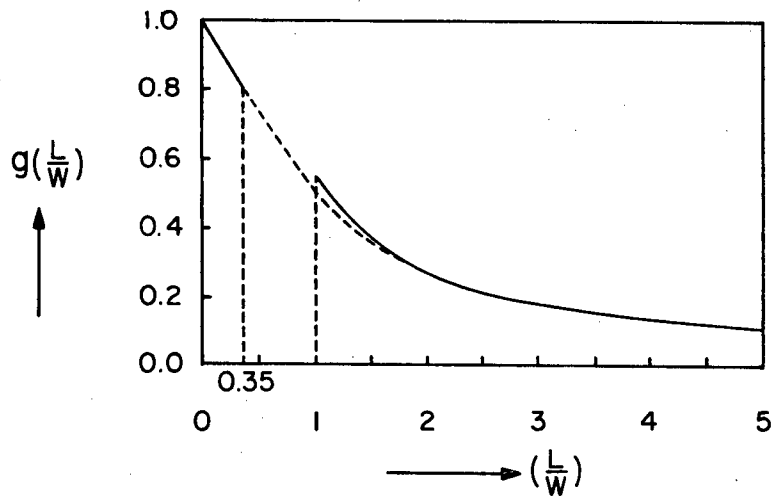
Figure 3-12. g(L/W) vs. L/W for Weak Magnetic Field

$$\left(\frac{\Delta R}{R_o}\right)_o = \left(\frac{\Delta \rho}{\rho_o}\right)_p + \mu_o \mu_B B^2 \qquad (3\text{-}32)$$

and if the ratio (L/W) approaches ∞, the magnetoresistances are equal to the values of the physical magnetoresistances.

$$r(B) \equiv r_\infty(B) = \frac{\mu_o}{\mu_B} \qquad (3\text{-}33)$$

$$\left(\frac{\Delta R}{R_o}\right)_o = \left(\frac{\Delta \rho}{\rho_o}\right)_p \qquad (3\text{-}34)$$

Magnetoresistance for Strong Magnetic Field (tanθ >> 1)

For strong magnetic field the magnetoresistance is expressed as

$$R(B) = \frac{1}{d\sigma_B \pi \varepsilon} \frac{1 + 2\varepsilon \ \ln \dfrac{1 + k}{2\sqrt{k}}}{1 + 2\varepsilon \ \ln \dfrac{1 + k}{1 - k}}$$

where

$$\varepsilon \equiv \frac{1}{2} - \frac{\theta}{\pi} \ll 1$$

49

With $\tan\theta = 1/\pi\varepsilon$,

$$R(B) = \frac{1}{d\sigma_B}\left(\tan\theta + \frac{2}{\pi}\ln\frac{1-k}{2\sqrt{k}}\right)$$

For $\pi\varepsilon < 0.24$, the error will be practically negligible.

$$r(B) = \frac{\sigma_o}{\sigma_B}\left\{\frac{W}{L}\tan\theta + g\left(\frac{L}{W}\right)\right\}$$

$$\left(\frac{\Delta R}{R}\right)_o = \frac{W}{L}\mu_o B + \frac{\mu_B}{\mu_o}g\left(\frac{L}{W}\right) - 1$$

The relation between the geometric coefficient $g(L/W)$ and ratio (L/W) is shown in Figure 3-13. Particularly, if the ratio (L/W) approaches ∞, the magnetoresistance is expressed as

$$r(B) = \frac{\sigma_o}{\sigma_B}\left\{1 + \frac{W}{L}\left(\tan\theta - \frac{4}{\pi}\ln 2\right)\right\}$$

$$\left(\frac{\Delta R}{R}\right)_o = \left(\frac{\Delta\rho}{\rho}\right)_o + \frac{W}{L}\left(\mu_o B - \frac{\mu_o}{\mu_B}\frac{4}{\pi}\ln 2\right)$$

Hall Potentials

The Hall voltage can be calculated using the same conformal mapping as shown in the previous section for magnetoresistance (Reference 3-17). The Hall voltage for the rectangular slab, illustrated in Figure 3-6, is given by

$$V_H = V_{H\infty}G\left(\frac{L}{W},\theta\right) \tag{3-35}$$

where

$V_{H\infty} \equiv$ Hall voltage when $L/W \rightarrow \infty$

$$V_{H\infty} = \frac{R_H I_x B}{d}$$

50

$$g(\tfrac{L}{W}) = \tfrac{2}{\pi}\left(\tfrac{W}{L}\right) \ln \tfrac{1-k}{2\sqrt{k}}$$
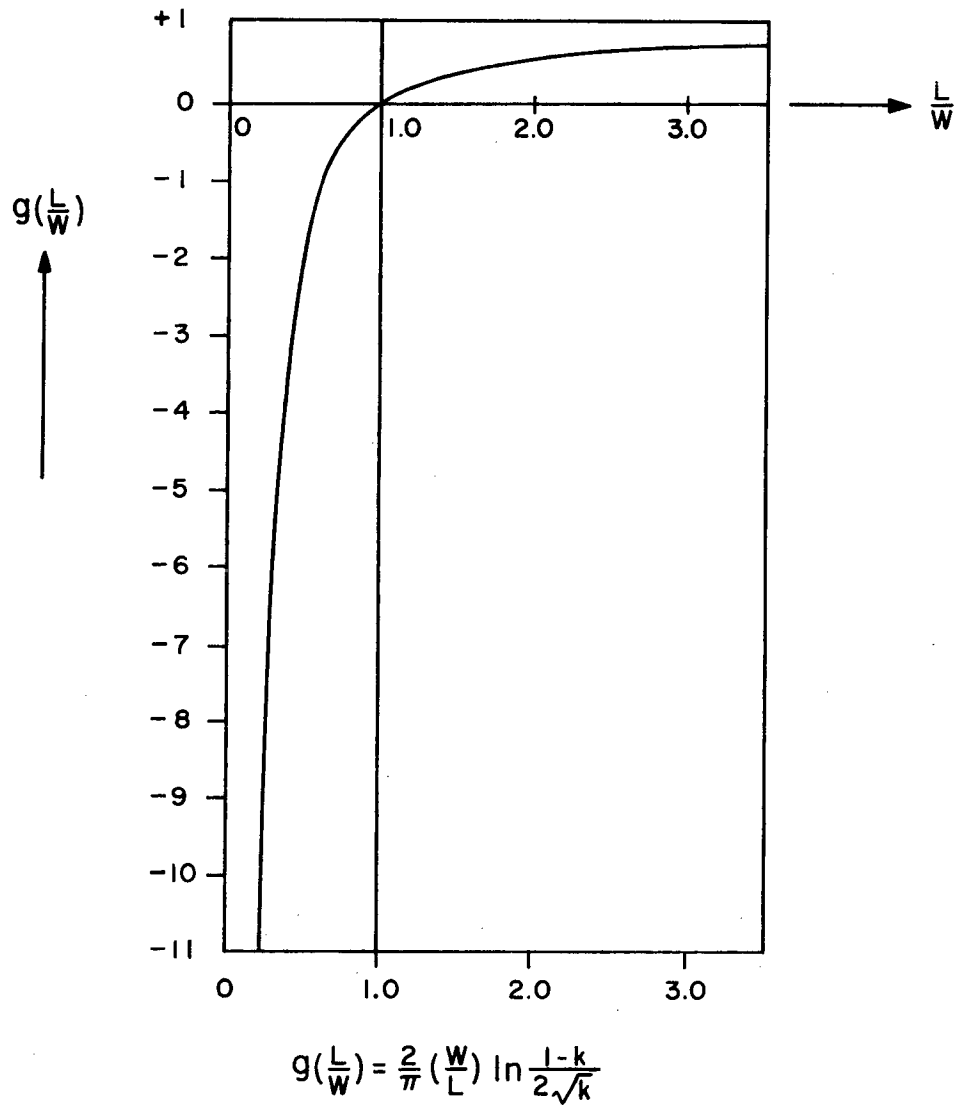
Figure 3-13. g(L/W) versus L/W for Strong Magnetic Field

51

The weak and strong magnetic field effects ($0 \leq \theta \leq 0.45$ and $\tan\theta \gg 1$) are clearly illustrated by showing the geometric function versus L/W with Hall angle in Figure 3-14.
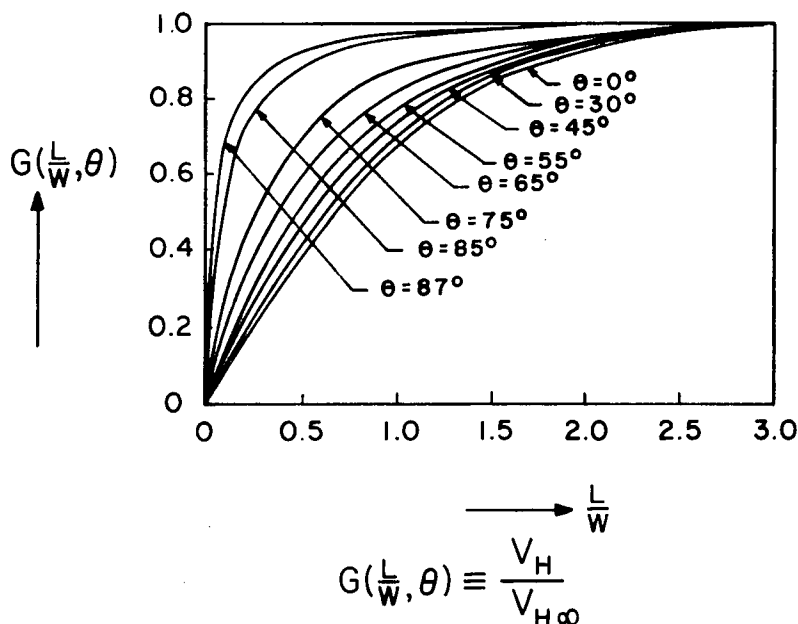
Figure 3-14. Geometric Function vs. Length-to-Width Ratio with Hall Angle as a Parameter (Reference 3-18)

The Corbino Disk Magnetoresistance Device--InSb Bulk and Thin-Film Magnetoresistors

The Corbino Disk Magnetoresistance

A semiconductor disk with coaxial center and peripheral electrodes has a circumferential current if it is subjected simultaneously to a steady, uniform, radial current and a transverse magnetic field. This phenomenon was observed by Corbino in 1911. This is due to the short circuiting of the circumferential Hall field induced in the disk by the orthogonal electric and magnetic field vectors. The magnetic-field-dependent magnetoresistance of a Corbino disk can be interpreted theoretically in terms of the generalized Hall-Ohm equations (References 3-18 and 3-19).

$$\vec{E} = \rho\vec{J} - R_H(\vec{J} \times \vec{B})$$

$$\vec{J} = \sigma\vec{E} + \sigma R_H (\vec{J} \times \vec{B})$$
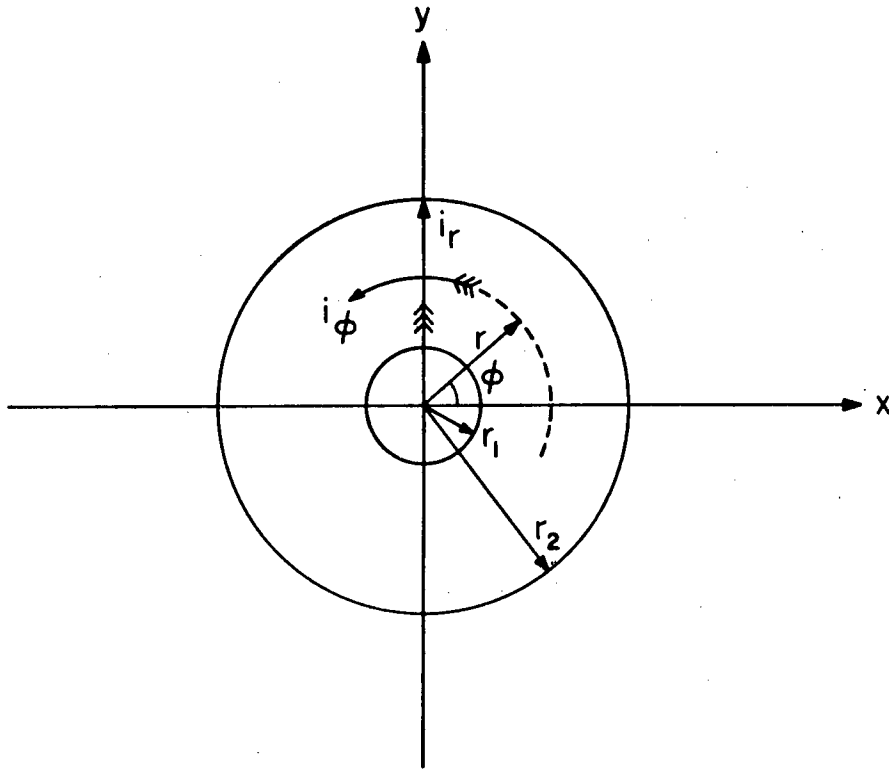
Figure 3-15. Current Flows in the Corbino Disk

Expressing the above equations in cylindrical coordinates (Figure 3-15) and solving for the field-dependent resistivity, the Corbino disk magnetoresistance is expressed as

$$\left(\frac{\Delta\rho}{\rho_o}\right)_c = \tan^2\theta = \mu_e^2 B_z^2 \tag{3-36}$$

for a single conduction band and a spherical energy surface of electrons. The electron mobility μ_e can be determined directly by measuring the $(\Delta\rho/\rho_o)_c$ versus B_z^2. In practice, Equation 3-36 does not hold, particularly in a high magnetic field. Beer (Reference 3-19) found the following relation to be in good agreement with experimental measurements.

$$\left(\frac{\Delta\rho}{\rho_o}\right)_c = \left[\left(\frac{\rho}{\rho_o}\right) - 1\right] + \frac{\rho}{\rho_o}\tan^2\theta \tag{3-37}$$

For two different conduction bands the magnetic-field-dependent DC conductivity tensor must be used and the effective Corbino disk magneto-resistance is expressed as

$$\left(\frac{\Delta\rho}{\rho_o}\right)_c = \frac{\left(\mu_1^2 \frac{\sigma_1}{\sigma_o} + \mu_2^2 \frac{\sigma_2}{\sigma_o}\right)B^2 + (\mu_1\mu_2 B^2)^2}{1 + B^2\left(\mu_1^2 \frac{\sigma_2}{\sigma_o} + \mu_2^2 \frac{\sigma_1}{\sigma_o}\right)}$$

where

$\sigma_o = \sigma_1 + \sigma_2$ (effective zero field conductivity)

subscripts 1 and 2 refer to band 1 and band 2

Beer (Reference 3-20) has evaluated the above equation for the different conditions as follows:

In InSb, the electron-to-hole mobility ratio is very large and defined as

$$b \equiv \frac{\mu_e}{\mu_h}$$

For a low magnetic field ($\mu_e B \ll 1$),

$$\left(\frac{\Delta\rho}{\rho_o}\right)_c = \frac{9\pi}{16}\mu_e^2 B^2 \tag{3-38}$$

In a stronger field region ($\mu_e B \geq 1$),

$$\left(\frac{\Delta\rho}{\rho_o}\right)_c = \frac{9\pi}{16}\mu_h^2 B^2 + b \tag{3-39}$$

In the very strong field ($\mu_e B \gg 1$),

$$\left(\frac{\Delta\rho}{\rho_o}\right)_c = \frac{9\pi}{32}\mu_e\mu_h B^2 \tag{3-40}$$

Thus $(\Delta\rho/\rho_o)_c$ follows a B^2 dependence in low fields, drops below the B^2 curve in higher fields, and eventually returns to a B^2 dependence in very high fields.

54

Two-Layer Corbino Disk Magnetoresistance

Experimentally, it was found that deviations of the thin-film Corbino disk magnetoresistance from a B^2 dependence in a strong magnetic field were evidence of the failure of the saturation of the ordinary magnetoresistance (References 3-18 and 3-20). The saturation of $(\Delta\rho/\rho_o)_c$ in a high magnetic field is the presence of a thin low-mobility surface layer in which electrons are subjected to strong scattering by surface-related lattice imperfections. In addition, impurities localized on the surface can be expected to produce a surface carrier density different from that of the major volume fraction of the film. The electron mobility in InSb films less than 1 μm in thickness decreases sharply with thickness (References 3-6 and 3-18). In InSb films, the thinner film data were given as d_s = 200 to 1,000 Å, μ_s = 500 cm^2/V-sec, n > 10^{17} cm^{-3}, and n-type surface property. For these reasons, the two-layer thin-film concept will be considered in the following.

The radial and circumferential currents per thickness in a thin-film Corbino disk are given by (from Figure 3-16)

$$d = d_s + d_b$$
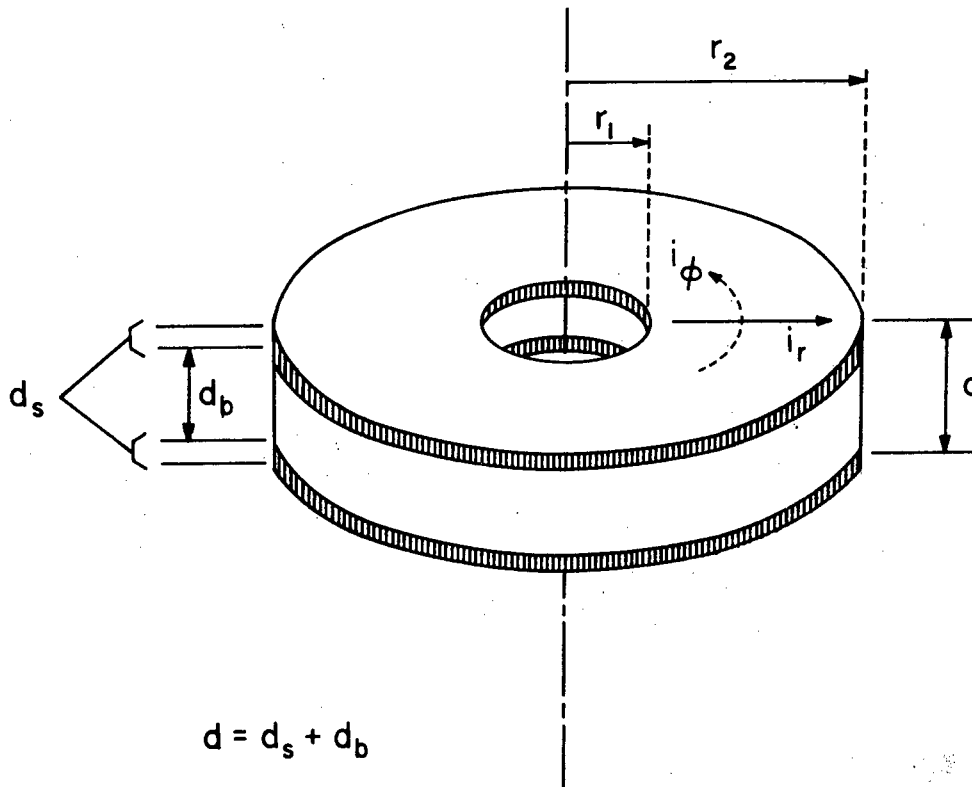
Figure 3-16. Thin-Film Two-Layer Corbino Disk

$$\frac{i_{rb}}{d_b} = \int_0^{2\pi} J_{rb} r d\phi \qquad\qquad (3\text{-}41)$$

$$\frac{i_{rs}}{d_s} = \int_0^{2\pi} J_{rs} r d\phi \qquad\qquad (3\text{-}42)$$

$$\frac{i_{\phi b}}{d_b} = \int_{r_1}^{r_2} J_{\phi b} dr$$

$$\frac{i_{\phi s}}{d_s} = \int_{r_1}^{r_2} J_{\phi s} dr$$

where

   subscripts b and s refer to bulk and surface

   subscripts r and ϕ refer to radial and circumferential components

Solving the above equations and taking the ratio of Equations 3-42 and 3-41,

$$\frac{i_{rs}}{i_{rb}} = \delta(1 + \mu_b^2 B^2) \qquad\qquad (3\text{-}43)$$

where

$$\delta \equiv \frac{\text{surface-like sheet conductivity}}{\text{bulk-like sheet conductivity}}$$

$$\delta = \frac{d_s \sigma_s}{d_b \sigma_b} = \frac{d_s \rho_b}{d_b \rho_s}$$

The magnetic field-dependent resistance and the magnetoresistance of the thin-film Corbino disk are given by

$$R_c(B) = \left(\frac{1}{2\pi d_b \sigma_b}\right)\left(\ell n \frac{r_2}{r_1}\right) \frac{1 + \mu_b^2 B^2}{1 + \delta(1 + \mu_b^2 B^2)} \qquad\qquad (3\text{-}44)$$

$$R_c(0) = \left(\frac{1}{2\pi d_b \sigma_b}\right)\left(\ell n \frac{r_2}{r_1}\right) \frac{1}{1 + \delta}$$

$$\left(\frac{\Delta R}{R_o}\right)_c = \frac{\mu_b^2 B^2}{1 + \delta(1 + \mu_b^2 B^2)} \tag{3-45}$$

Equation 3-45 indicates evidence of saturation of $(\Delta R/R_o)_c$ in high magnetic fields. The required field B_{sat} for the onset of saturation can be determined by taking the second derivative with respect to B of $(\Delta R/R_o)_c$, equating it to zero, and solving for the B_{sat}.

$$B_{sat} = \frac{1}{\mu_b} \sqrt{\frac{1 + \delta}{3\delta}} \tag{3-46}$$

Galvanomagnetic Coefficients of Two-Layer Rectangular Films

To obtain the galvanomagnetic coefficient of the two-layer Corbino disk, a rectangular film on an insulating substrate $(L/W \geq 3)$ may be considered. For a single conduction band of electrons, a homogeneous isotropic carrier concentration n and mobility μ in the x-y plane of the film, and respective z-dependent quantities n(z) and $\mu(z)$ along the film thickness d, the components of the current density vector are (Reference 3-18)

$$J_x = \frac{\sigma}{1 + \mu^2 B^2}(E_x + \mu B E_y)$$

$$J_y = \frac{\sigma}{1 + \mu^2 B^2}(E_y - \mu B E_x)$$

from which effective conductivity σ_{eff}, effective Hall mobility μ_{eff}, and effective Hall coefficient $R_{H_{eff}}$ can be calculated.

$$\sigma_{eff} = \frac{1}{E_x d} \int_0^d J_x dz = \alpha(1 + \mu_{eff}^2 B^2)$$

$$\mu_{eff} = \frac{\beta}{\alpha} = \frac{1}{B} \tan\theta_{eff} = \frac{1}{B}\left(\frac{E_y}{E_x}\right)$$

$$R_{H_{eff}} = \frac{\beta}{\alpha^2 + \beta^2 B^2}$$

57

where

$$\alpha \equiv \frac{1}{d} \int_0^d \frac{\sigma dz}{1 + \mu^2 B^2}$$

$$\beta \equiv \frac{1}{d} \int_0^d \frac{\sigma \mu dz}{1 + \mu^2 B^2}$$

$$\theta_{eff} = \text{effective Hall angle}$$

If $\mu_b \gg \mu_s$ and $\mu_s^2 B^2 \ll 1$, then

$$\mu_{eff} = \frac{g\mu_b}{1 + g + \mu_b^2 B^2} = \frac{\mu_b}{1 + \delta(1 + \mu_b^2 B^2)}$$

where

$$g \equiv \frac{\tilde{\sigma}_b}{\tilde{\sigma}_s} \equiv \frac{1}{\delta}$$

$$\tilde{\sigma}_b \equiv \sigma_b d_b$$

$$\tilde{\sigma}_s \equiv \sigma_s d_s$$

and the effective Hall coefficient is expressed as

$$R_{Heff} = R_{Hb} \left[\frac{g^2 \left(\frac{d}{d_b}\right)}{(1 + g)^2 + \mu_b^2 B^2} \right]$$

where

$$R_{Hb} \equiv \frac{\mu_b}{\sigma_b}$$

The physical magnetoresistance is

$$\left(\frac{\Delta\rho}{\rho_o}\right)_p = \frac{g(\mu_b B)^2}{(1 + g)^2 + \mu_b^2 B^2}$$

Since g includes a surface-layer sheet conductivity term, the surface layer is responsible for a physical magnetoresistance component and for a magnetic field dependence of the Hall coefficient.

Theoretical and Experimental Data for InSb Devices

Bulk Corbino Disk Magnetoresistance Devices

Given: At $T = 80°K$, $\mu_e = 300{,}000$ cm^2/V-sec, $n = 5 \times 10^{14}$ cm^{-3},
$R_H = 13{,}750$ cm^3/coul, and $\sigma = 21.8$ (ohm-cm)$^{-1}$.
At $T = 300°K$, $\mu_e = 78{,}000$ cm^2/V-sec, $n = 2.22 \times 10^{16}$ cm^{-3},
$R_H = 310$ cm^3/coul, and $\sigma = 252$ (ohm-cm)$^{-1}$
(References 3-16 and 3-21).

The ratio ρ_H/ρ_o versus B is shown in Table 3-1 (Reference 3-16).

Table 3-1

Comparison of (ρ_H/ρ_o) versus B

$\dfrac{\rho_H}{\rho_o} = \dfrac{\mu_o}{\mu_H}$ B (KGauss)	0	2	4	6	8	10
Weiss and Walker	1.00	1.05	1.14	1.25	1.36	1.48
Simmons	1.00	1.04	1.10	1.20	1.34	1.49

The relationship between Corbino disk magnetoresistance coefficients and magnetic field is shown in Figure 3-17.

Galvanomagnetic Coefficients of Bulk Rectangular Hall Devices

Given: $L/W = 2$ and 4
$d = 1$ mm
$I_x = 50$ mA

Since the analysis under the strong magnetic field introduces error, the low field analysis is used and the Hall voltage will be calculated graphically (Reference 3-17).
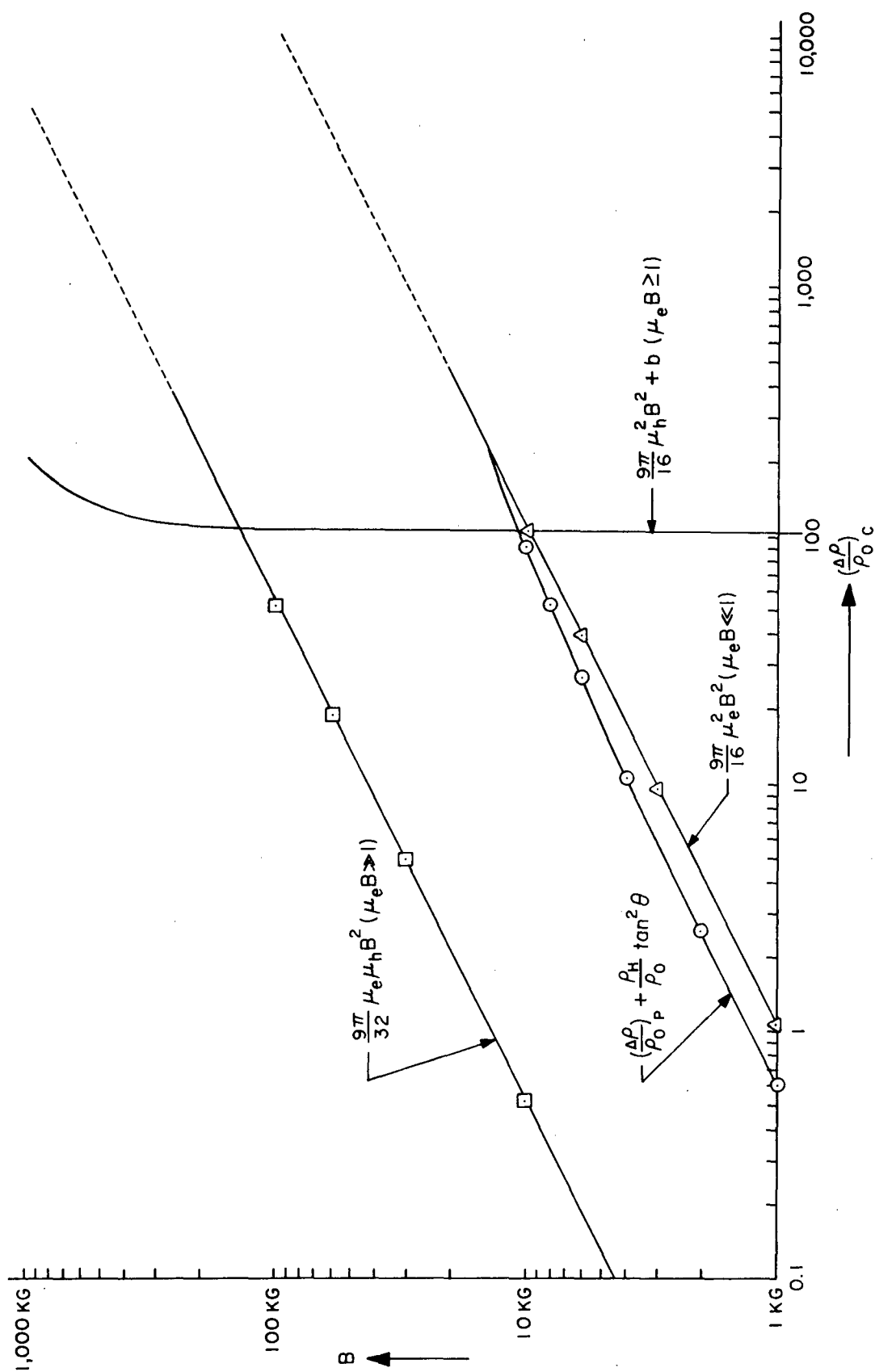
Figure 3-17. Corbino Disk Magnetoresistance Coefficients versus Magnetic Field in InSb Bulk

$$V_{H\infty} = 15.5 \times 10^{-3} B \text{ in volts}$$

for $L/W = 4$ and $B = 0.1$ Wb/m^2, the following coefficients are obtained.

$$R_H = 310 \text{ cm}^3/\text{coul}$$

$$\sigma = 252 \text{ (ohm-cm)}^{-1}$$

$$\mu_H = 78,000 \text{ cm}^2/\text{V-sec}$$

$$\langle n \rangle = 2.22 \times 10^{16} \text{ cm}^{-3}$$

For $L/W = 2$ and $B = 0.1$ Wb/m^2, V_{ab} is equal to 0.397 V, and results similar to those above were obtained. The Hall voltage curves for different geometries are plotted in Figure 3-18.

Galvanomagnetic Coefficients of Square Hall Devices

Given: $L = W = 1$ cm

$d = 1$ mm

$I_x = 50$ mA

For $V_\square = 0.438$ mV, $V_{H\diamondsuit} = 1.55$ mV, and $B = 0.1$ Wb/m^2, the galvanomagnetic coefficients are obtained.

$$\sigma = 252 \text{ (ohm-cm)}^{-1}$$

$$R_H = \frac{d \Delta V_{H\diamondsuit}}{B I_x} = 310 \text{ cm}^3/\text{coul}$$

$$\mu_H = \sigma R_H = 78,000 \text{ cm}^2/\text{V-sec}$$

$$\langle n \rangle = \frac{1.1}{e R_H} = 2.22 \times 10^{16} \text{ cm}^{-3}$$

The Hall voltage curves are plotted in Figure 3-18.

Galvanomagnetic Coefficients of Two-Layer Rectangular Films

Given: At $T = 300°K$, $\sigma_{eff} = 200$ $(\text{ohm-cm})^{-1}$, $\mu_{eff} = 66,000$
$cm^2/\text{V-sec}$, $R_{Heff} = 330 \text{ cm}^3/\text{coul}$, $L/W = 4$, $d = 4$ µm,
$d_s = 0.1$ µm, $\sigma_s = 234$ $(\text{ohm-cm})^{-1}$, $\mu_s = 1,000 \text{ cm}^2/\text{V-sec}$,
$R_{Hs} = 4.28 \text{ cm}^3/\text{coul}$, $n_s = 1.605 \times 10^{18} \text{ cm}^{-3}$,
$I_x = 1$ mA, $g = 33.33$ and $\mu_b \gg \mu_s$ (References 3-18,
3-22, and 3-23).
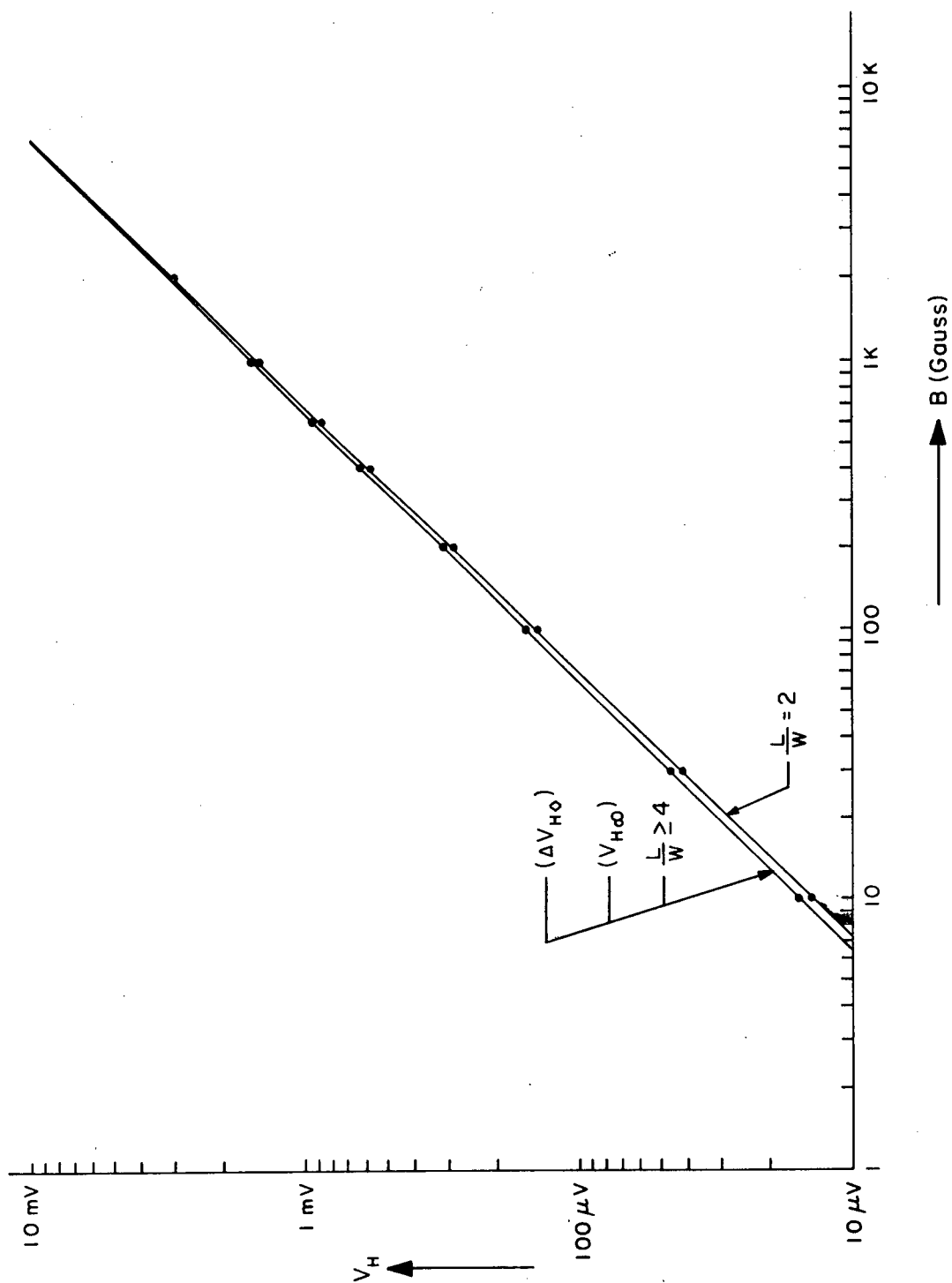
Figure 3-18. Hall Voltages versus Magnetic Field for Different
Length-to-Width Ratio and Square Diamond Geometry

62

In the low magnetic field region, the following coefficients are obtained from the experimental measurement of the Hall voltage.

$$\sigma_b = 195 \text{ (ohm-cm)}^{-1}$$

$$\mu_b = 68,000 \text{ cm}^2/\text{V-sec}$$

$$R_{Hb} = 349 \text{ cm}^3/\text{coul}$$

$$<n_b> = 1.97 \times 10^{16} \text{ cm}^{-3}$$

The curves for the physical magnetoresistance versus magnetic field are plotted in Figure 3-19.

Galvanomagnetic Coefficients of Two-Layer Corbino Disks

Given: At $T = 300°K$, $d_b = 3.9 \ \mu\text{m}$, $\sigma_b = 195 \text{ (ohm-cm)}^{-1}$, $R_{Hb} = 349$ cm^3/coul, $\mu_{eb} = 68,000 \text{ cm}^2/\text{V-sec}$, $n_b = 1.97 \times 10^{16} \text{ cm}^{-3}$, $d_s = 0.1 \ \mu\text{m}$, $\sigma_s = 234 \text{ (ohm-cm)}^{-1}$, $R_{Hs} = 4.28 \text{ cm}^3/\text{coul}$, $\mu_{es} = 1,000 \text{ cm}^2/\text{V-sec}$, $n_s = 1.605 \times 10^{18} \text{ cm}^{-3}$, and $\delta = 0.03$ (Reference 3-24).

The saturation value of the magnetic field is obtained using Equation 3-46 showing $B_{sat} = 4.96 \times 10^{-1} \text{ Wb/m}^2$. The magnetoresistance coefficients versus magnetic field of the two-layer Corbino disk are plotted in Figure 3-20.

The Effects of Radiation on Indium Antimonide

The effects of electromagnetic radiation and high-energy particles on semiconductors include changes of semiconductor properties. Both ionization and neutron radiation on semiconductors will be studied. Ionization radiation induces a transient effect in a short time after radiation while neutron radiation results in permanent stable defects.

The Interaction of Electromagnetic Radiation with Matter

Electromagnetic radiation includes effects produced by the photons which are classified according to their mode of origin, not their energy. Thus, gamma rays are the electromagnetic radiations accompanying nuclear transitions. Bremsstrahlung (or continuous X rays) are the result of the acceleration of free electrons or other charged particles. Characteristic X rays are emitted in atomic transitions of bound electrons
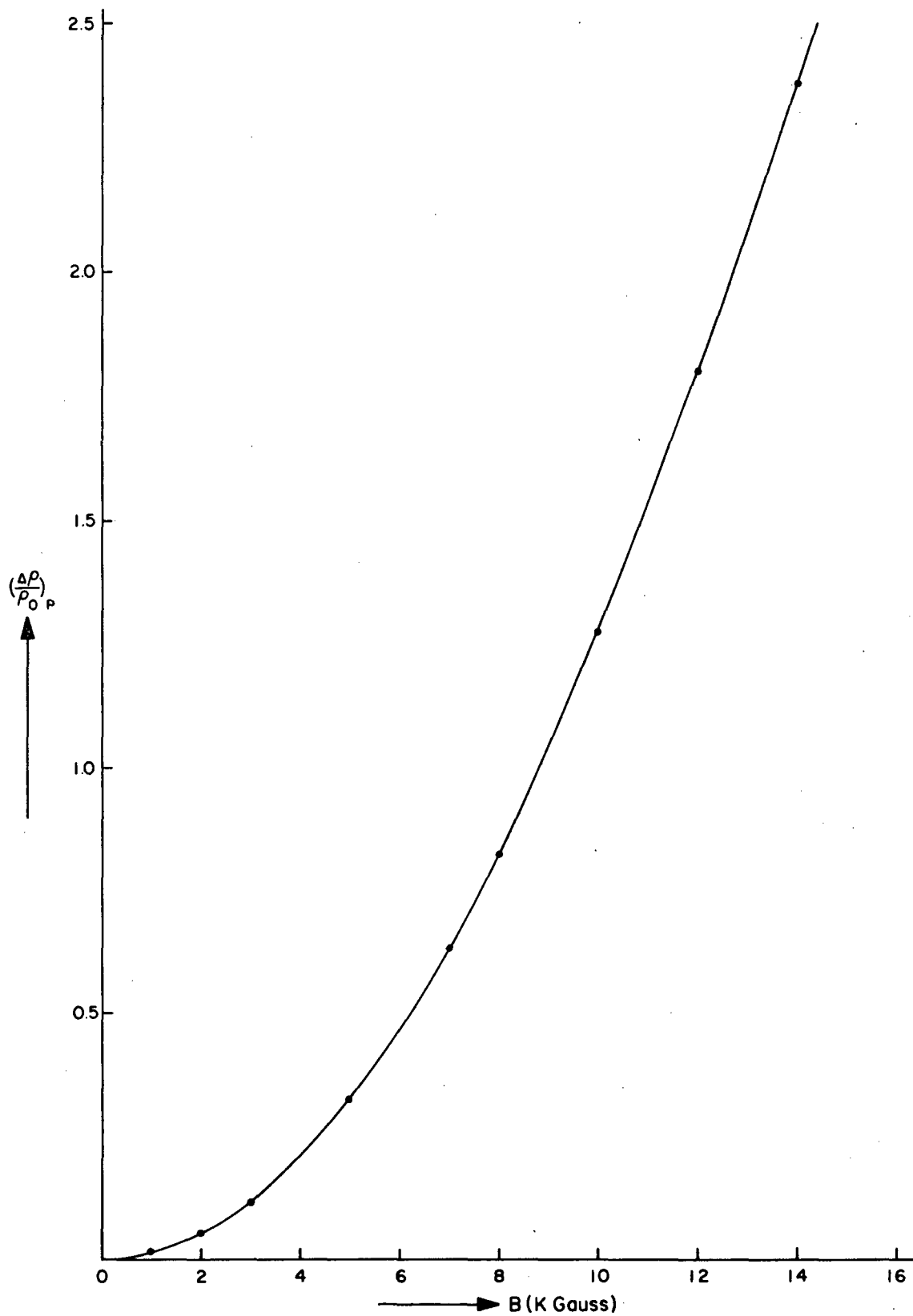
Figure 3-19. Physical Magnetoresistance Coefficients versus
Magnetic Field for InSb Rectangular Film Device
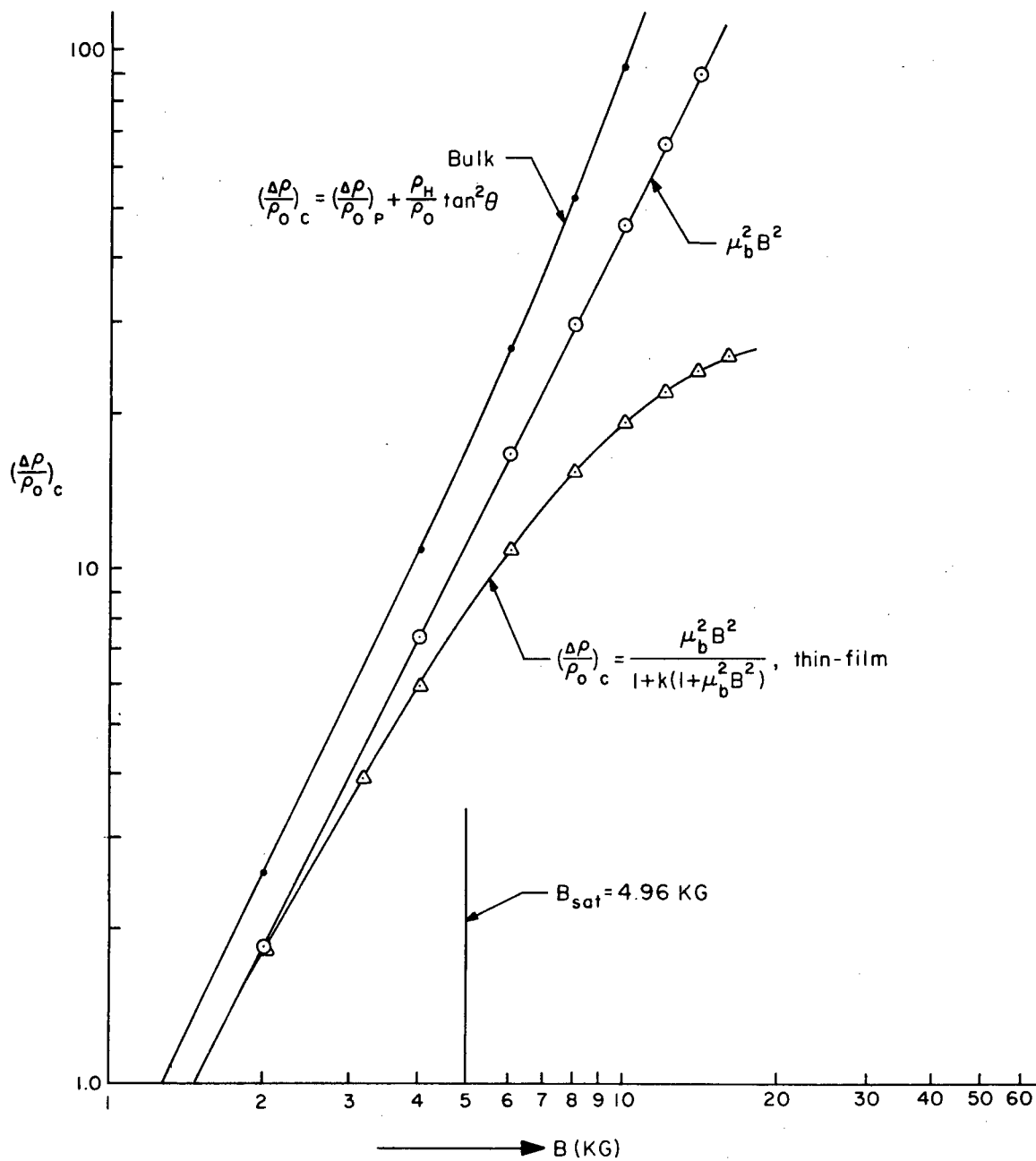
Figure 3-20.   Magnetoresistance versus Magnetic Field
of the Two-Layer Corbino Disks

between the K, L, M, ··· shells in atoms. Annihilation radiation is emitted when a positron and negatron combine. The quantum energy of any of these radiations can be expressed as $E = h\nu$. Interactions of these photons with matter are thought to be independent of the mode of origin of the photon and dependent only upon its quantum energy (Reference 3-25).

The three major types of gamma-ray interaction are photoelectric effect, Compton effect, and pair production. The relative importance of these interactions is clearly illustrated in Figure 3-21.
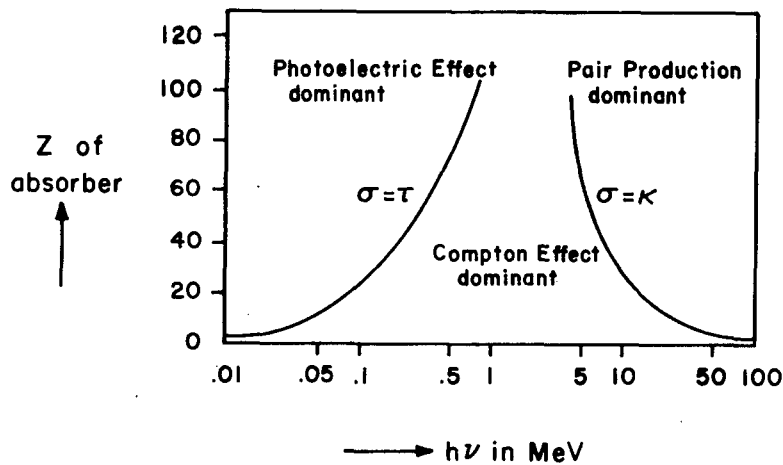
Figure 3-21. Relative Importance of the Three Major Types
of Gamma-Ray Interaction

The effects which photons produce in matter are actually almost exclusively due to the secondary electrons. A photon produces primary ionization only when it removes an electron from an atom by a photoelectric collision or by a Compton collision, but the swift secondary electron which is produced from each primary ionization collision may have nearly as much kinetic energy as the primary photon. This secondary electron dissipates its energy mainly by producing ionization and excitation of the atoms and molecules in the medium. For electrons of the order of 1 MeV, an average of about 1 percent of the electron energy is lost as bremsstrahlung. The one primary ionization is completely negligible in comparison with the very large amount of secondary ionization. The net result of successive generations of interactions is the production of low-energy electrons which no longer have enough energy to

66

produce any further ionization and whose final energy distribution is essentially independent of the primary process. These electrons will then lose energy by scattering until they are either captured or thermalized.

Effects of Ionization Radiation upon Semiconductors

In semiconductors, the ionization process is studied by assuming low photon energy and by neglecting pair production. The transient effect of secondary electrons by the ionization process is of primary interest.

The ionization produces free electrons in the conduction band and free holes in the valence band of the semiconductors. The incident photons into gases create electron-ion pairs; an energy deposited is equal to approximately twice the ionization potential. However, in semiconductors, energy of approximately three to four times the bandgap (E_g) is necessary to create an electron-hole pair. Both holes and electrons contribute to the conduction process significantly in the semiconductor since the current density is expressed as (Reference 3-26)

$$J = J_e + J_h = e[\mu_h(P + bn)E - D_h \text{grad}(P - bn)]$$

where

μ_h = hole mobility

E = electric field

D_h = hole diffusion constant

$b = \mu_e/\mu_h$

$\sigma = e\mu_h(P + bn)$

From the above expressions, it is evident that the material conductivity can be increased by irradiation (transient ionization) because of excess carrier generation. In semiconductors, the excess carrier lifetime is important in determining material properties. The dependence of the excess carrier lifetime upon the recombination centers in the forbidden gap is particularly significant in discussing displacement radiation effects. The conduction process is also limited by traps which are defects

67

with a large capture cross section for one type of the mobile carriers. The trap captures a carrier, holds it for a finite length of time, and then releases it so that it may again contribute to conduction.

Effects of Stable Fast Neutron Radiation

The effects of energetic neutrons on the physical properties of semiconductors will be considered. Effects on the electrical properties of semiconductors are of particular interest because of the relatively large changes induced by small amounts of irradiation and the technological importance (Reference 3-27). The major effects are carrier removal, a decrease in excess carrier lifetime, and a decrease in carrier mobility.

In stable fast neutron irradiation, neutrons with energies in excess of 10 KeV (which will be designated as fast neutrons) will displace atoms from their normal lattice positions into an interstitial position. This creates vacant lattice sites (vacancies) and interstitial atoms (interstitials).

One important aspect of radiation damage is the spatial distribution of the defects. The damage introduced by a very energetic primary knock-on will occur in a rather small localized region containing a high density of defects. The total damage produced by a recoil atom bombarded with fission neutrons will lie within a region of about "range" radius (Reference 3-28). The "range" of a particle is an experimental concept, relating to the thickness of an absorber which the particle can just penetrate. The electrical size of the damaged regions may be considerably larger than their physical size; they are thus expected to play an important role in the transport properties of a semiconductor. The defect regions may be of opposite conductivity type relative to the bulk semiconductor. More direct evidence for the inhomogeneous nature of fast neutron damage is provided by electron microscope studies (References 3-29 and 3-30). A thorough discussion of damaged regions of semiconductors is given by Vook (Reference 3-31).

The recombination centers created in the forbidden energy gap of the semiconductor capture conducting carriers thus removing them from the valence and conduction bands. The defect cluster intrinsic voids

and defect carrier removal determine the carrier removal rate. The mobility changes in the semiconductor are primarily due to reduction in active volume by the intrinsic voids (References 3-32, 3-33, and 3-34). Since the excess minority-carrier lifetime decreases with neutron bombardment and the lifetime is a very strong function of the defect concentration, it is considered as a sensitive parameter of neutron bombardment.

Much of the radiation damage research on semiconductor materials has been concerned with detecting bombardment-produced energy levels. Many levels have been detected in germanium and silicon, fewer in compounds. Clear-cut explanations which relate the levels to the defects and their geometrical arrangement have been generally lacking (Reference 3-27).

Using the results of silicon and germanium, the radiation effects in compound materials can be predicted since the carrier removal rates, for instance, are of the same order of magnitude in different compounds and since the results for monatomic semiconductors (Si, Ge) do not differ greatly from those of compounds (Reference 3-32).

Effects of Radiation upon Indium Antimonide

The electrical properties of irradiated InSb are very sensitive to the temperature and type of irradiation. This fact is reflected by the final Fermi level position values (E_{ff}) for different irradiation conditions. At liquid nitrogen temperature, E_{ff} is close to or below E_v for 1-MeV electron radiation, it is about $E_v + 0.03$ eV for 4.5-MeV electrons (References 3-35, 3-36, and 3-37), and is closer to the middle of the gap or above it for fast neutron irradiation (References 3-38 and 3-39). For room temperature neutron irradiation (References 3-40 and 3-41), E_{ff} is equal to $E_c - 0.015$ eV. Thus, increasing the temperature of irradiation also causes E_{ff} to increase. An increase in E_{ff} corresponds to the creation of additional donors or the shifting of energy levels toward the conduction band.

The energy levels found in irradiated InSb at 300°K are determined from temperature dependence of the Hall coefficient ($E_c - 0.02$ eV, References 3-40 and 3-41) and from photoelectromagnetic (PEM) and

photoconduction (PC) measurements (E_v + 0.12 eV and E_v + 0.055 eV, Reference 3-42). Fast neutron bombardment at liquid nitrogen temperature creates what might be the same level as room temperature electron bombardment at about 0.056 eV.

The estimated introduction rates by 4.5-MeV electron irradiations are 3.5, 1.5, and 1.5 (1/cm) for the levels at 0.03, 0.04, and 0.055 eV, at 80, 200, and 300°K, respectively (References 3-35, 3-36, and 3-42).

One of the most striking differences between III-V compounds and group IV (e.g., Si and Ge) shows up in the response of lattice expansion to irradiation. The specific lattice strain for structural defects is much greater in InSb than in Ge or Si (Reference 3-31). This is due to a greater lattice strain per defect rather than a greater introduction rate. The lattice strain per Frenkel pair in InSb is about one atomic volume, and in Ge only about 0.02 atomic volume. The physical reason for this result most probably involves the partially ionic character of the III-V semiconductors. It is believed that the strain arises from repulsion between the four charged nearest neighbors to a vacancy.

The electrical resistivity increases suddenly with irradiation and then slowly decreases. The initial increase is probably due to the generation of point defects. The gradual decrease is due to the amorphous regions, which should have a metallic-like conductivity.

The effects of 2-MeV electron radiation at about 50°K on the thermal resistivity of high impurity InSb have been studied (References 3-31, 3-43, and 3-44). The added thermal resistance (cm-degree/watt) increases as the 3/4 power of the integrated flux, ϕ in electrons/cm^2.

The most thorough annealing experiments on InSb are those carried out by Eisen (References 3-45, 3-46, 3-47, 3-48, and 3-37). The isochronal annealing of n-type and p-type InSb after 1-MeV electron irradiation is illustrated in Figure 3-22. Annealing studies on n-type InSb irradiated with 4.5-MeV electrons show the same general future, except that stages III and IV apparently were not resolved. In both stages nearly all the observable damage in n-type InSb is removed after stage V is completed. The monitoring property is carrier density from Hall measurements. Reactor irradiation carried out under the condition of a
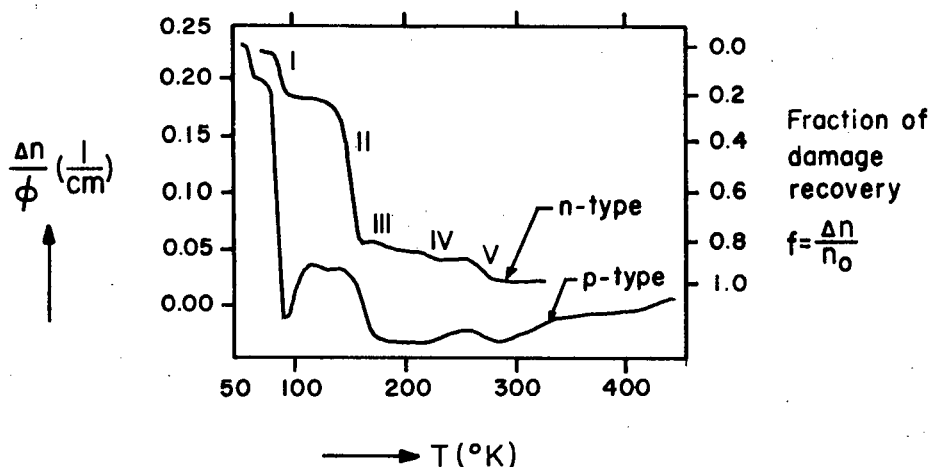
Figure 3-22.   Isochronal Annealing of n-Type and p-Type
InSb After 1-MeV Electron Irradiation

rather large accompanying gamma-flux produced essentially the same an-
nealing characteristics, except that stages III, IV, and V are relatively
more prominent.

It was found that, for electron-irradiated specimens, the anneal-
ing of mobility slightly precedes the annealing of carrier density.
One-MeV electron irradiation of p-type InSb with a carrier density in
the 10^{16} cm^{-3} range, at 80°K, increases the carrier density and de-
creases the mobility. The first two annealing stages decrease the car-
rier density and increase the mobility. The higher temperature anneal-
ing stages are quite complex, some of them temporarily reversing the an-
nealing trend in carrier density. There are actually two energy levels
associated with stage II annealing; one at E_v + 0.04 eV and one at E_c -
0.03 eV. The recovery of InSb irradiated with 1-MeV electrons appears
to be considerably more complicated for p-type than for n-type.

The annealing of fast neutron pulsed reactor irradiated n- and p-
type InSb differs considerably from that of electron- or gamma-irradiated
specimens (Reference 3-38). In the temperature range 100 to 250°K, a
remarkable increase in the net donor concentration occurs in both p- and
n-type samples. Near room temperature, this trend is reversed, but com-
plete recovery is not observed up to the highest temperature of anneal-
ing, 400°K. For instance, the initially n-type specimen of InSb was
converted to p-type by the irradiation.

Kurdiani (Reference 3-49) found that the recovery of the original electron density in n-type InSb single crystals, $n_o = 1.3 \times 10^{14}$ cm^{-3} and $\mu_o = 400,000$ cm^2/V-sec at 77°K, irradiated with fast neutrons of 10^{17} neutrons/cm^2 at 50°C, took place in three stages: I--60-120°C, II--120-160°C, and III--160-300°C. The recovery of the electron density is complete after annealing at 300°C. The electron mobility also increases as the isochronal annealing temperature is raised. However, a complete recovery of the electron mobility requires additionally several annealing cycles in the 300-360°C range. A comparison of the results of annealing, represented by changes in the electron density and mobility, indicated that the fast-neutron bombardment of InSb produced some imperfections in addition to other defects, which did not alter the electron density but affected the electron mobility because of additional scattering. The bombardment of InSb with fast neutrons may generate oppositely charged centers forming composite neutral complexes of the dipole type. The annealing of the irradiated crystals shows that these complexes are very stable, probably because of the Coulomb interaction of neighboring oppositely charged centers. The changes in carrier density, brought about by stage I and II annealing, imply the removal of acceptors, since the electron concentration increases and the hole concentration decreases in n-type and p-type, respectively. Fast neutron irradiation also produces a more donor-like distribution of energy levels. Reverse annealing in both properties (n- and p-types) was observed near 105 and 310°K (Reference 3-43). This would seem to imply an actual increase in the number of defects (scattering centers) during these two annealing stages.

Effects of Radiation upon Indium Antimonide Thin Films

The thin films prepared by vacuum deposition and recrystallization are normally polycrystalline in structure. These films have many imperfections in crystalline structure by nature; therefore, radiation effects on these films involve complexity as well as uncertainty. For instance, it can be said that single-crystal semiconductors have linear characteristics, while thin-film semiconductors are nonlinear. The electrical characteristics of thin films may be studied through the experiments

because theoretical analysis of the thin films is very complicated, and it is impossible to model the complete polycrystalline films.

Since there are many imperfections in the polycrystalline films, effects of radiation of low energy are not detectable; therefore, thin films are subjected to radiation-hardened device studies. These films, when irradiated with electron dose rates of 6×10^9 rads(InSb)/sec at 1.3 MeV and 2×10^{11} rads(InSb)/sec at 2.3 MeV as well as when irradiated with neutron fluences of 10^{14}, 10^{15}, and 10^{16} nvt (neutrons/cm^2) did not indicate any change in electron mobilities. However, at 10^{17} nvt, electron mobilities of all these films dropped below 20,000 cm^2/V-sec (Figure 3-23). The change in carrier concentration per unit of fluence, $-\Delta n/\Delta\phi$ (cm^{-1}) due to the neutron radiation should not be expected to be significant until the neutron fluence is of the same order of magnitude as the carrier concentration. For fast neutron bombardment of compound semiconductors (Reference 3-32), the carrier removal rate is between 2 and 6 (Reference 3-33). However, for the thin films, the carrier removal rates range from 0.247 to 3.350 cm^{-1}. Sometimes, because of insufficient recrystallization of InSb thin films, the carrier concentration of the films increases after irradiation at very high neutron fluence levels. For this case, the opposite sign of the carrier removal rate may be used.

Although some comments indicate that the experimental results fit into a fairly consistent pattern, it must not be assumed that all radiation effects in InSb are well understood. On the contrary, very little is actually understood, although InSb is probably somewhat further along in this respect than any other III-V compound. There are some unanswered questions concerning which defects give rise to which energy levels, what processes are involved in the various annealing stages, and why there is no evidence of donor creation by 1-MeV electrons at low temperature; therefore, the radiation effects on polycrystalline InSb films are studied by experiments.
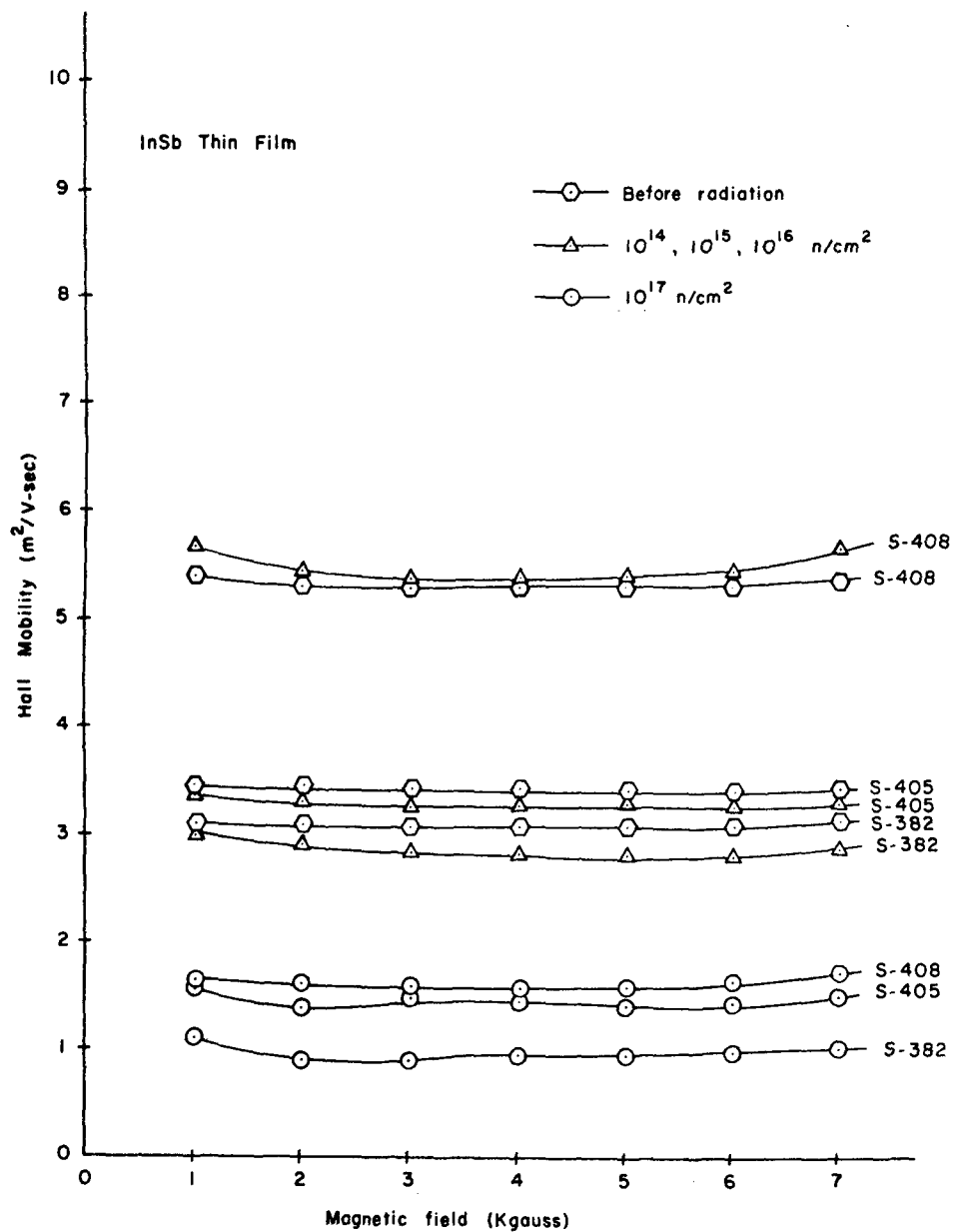
Figure 3-23. Variation of Hall Mobility with
Magnetic Field for Three Different Films

References

3-1.   E. H. Putley, *The Hall Effect and Related Phenomena*, Butterworth, London, 1960.

3-2.   W. Shockley, *Electrons and Holes in Semiconductors*, Van Nostrand, Princeton, 1950.

3-3.   A. C. Beer, "The Hall Effect and Related Phenomena," *Solid-State Electronics*, Vol. 9, p. 339, 1966.

3-4.   R. A. Smith, *Semiconductors*, University Press, Cambridge, 1961.

3-5.   A. C. Beer, *Galvanomagnetic Effects in Semiconductors: Supplement 4 to Solid-State Physics Series*, p. 6, Academic Press, N.Y., 1963.

3-6.   N. F. Teede, "Single Crystal InSb Thin Films by Electron Beam Re-crystallization," *Solid-State Electronics*, Vol. 10, p. 1069, 1967.

3-7.   T. C. Harman and J. M. Honig, *Thermoelectric and Thermomagnetic Effects and Applications*, McGraw-Hill, N.Y., 1967.

3-8.   J. P. McKelvey, *Solid-State and Semiconductor Physics*, Harper and Rowe, N.Y., 1966.

3-9.   A. C. Smith, J. F. Janak, and R. B. Adler, *Electronic Conduction in Solids*, McGraw-Hill, N.Y., 1967.

3-10.   L. B. Valdes, "Resistivity Measurements on Germanium for Transistors," *Proc. IRE*, Vol. 42, p. 420, 1954.

3-11.   L. I. Maissel and R. Glang, *Handbook of Thin Film Technology*, McGraw-Hill, N.Y., 1970.

3-12.   L. J. van der Pauw, "A Method of Measuring Specific Resistivity and Hall Effect of Discs of Arbitrary Shape," Philips Research Reports, Vol. 13, February 1958.

3-13.   T. W. Kim, H. Y. Yu, and W. W. Grannemann, *Metal-Insulator-Semiconductor (MIS) Magnetoresistance Devices Using the Thick Films of the InSb Compound Semiconductor Material*, Bureau of Engineering Research Technical Report PR-96(70)NASA-028, The University of New Mexico, September 1970.

3-14.   C. Kittel, *Introduction to Solid-State Physics*, 3rd Ed., John Wiley & Sons, N.Y., 1968.

3-15.   H. J. Lippmann and F. Kuhrt, "Der Geometrieeinfluss auf den transversalen magnetischen Widerstandseffekt bei rechteckförmigen Halbleiterplatten," *Z. Naturforschg.*, Vol. 13a, p. 462, 1958.

3-16. C. A. Simmons, "Influence of the Hall Effect upon the Transverse Magnetoresistance in Indium Antimonide," *Journal of Applied Physics*, Vol. 32, No. 10, October 1961.

3-17. H. J. Lippmann and F. Kuhrt, "Der Geometrieeinfluss auf den Hall-Effekt bei rechteckigen Halbleiterplatten," *Z. Naturforschg.*, Vol. 13a, p. 474, 1958.

3-18. H. H. Wieder, "Anomalous Transverse Magnetoresistance of InSb Films," *Journal of Applied Physics*, Vol. 40, No. 8, p. 3320, July 1969.

3-19. A. C. Beer, "Galvanomagnetic Effects in III-V Compound Semiconductors," *Journal of Applied Physics*, Vol. 32, No. 10, p. 2107, October 1961.

3-20. A. C. Beer, *Galvanomagnetic Effects in Semiconductors: Supplement 4 to Solid-State Physics Series*, p. 159, Academic Press, N.Y., 1963.

3-21. H. H. Wieder, "Galvanomagnetic Properties of Recrystallized Dendritic InSb Films," *Solid-State Electronics*, Vol. 9, p. 373, 1966.

3-22. C. Juhasz and J. C. Anderson, "Field-Effect Studies on Indium-Antimonide Films," *British Journal of the Institute of Radio and Electronic Engineers*, Vol. 33, p. 223, 1967.

3-23. V. L. Frantz, "Indium Antimonide Thin Film Transistor," *Proceedings of the IEEE*, Vol. 53, p. 760, July 1965.

3-24. A. R. Clawson and H. H. Wieder, "Electrical and Galvanomagnetic Properties of Single Crystal InSb Dendrites," *Solid-State Electronics*, Vol. 10, p. 57, 1967.

3-25. R. D. Evans, *The Atomic Nucleus*, McGraw-Hill, N.Y., 1955.

3-26. A. K. Jonscher, *Principles of Semiconductor Device Operation*, G. Bell and Sons, Ltd., London, 1960.

3-27. L. W. Aukerman, "Radiation Effects" in *Semiconductors and Semimetals*, Vol. 4 (ed. Willardson and Beer), Academic Press, N.Y., 1968.

3-28. V. A. J. van Lint, M. E. Wyatt, R. A. Schmitt, C. S. Saffredidi, and D. K. Nichols, "Range of Photoparticle Recoil Atoms in Solids," *Physical Review*, Vol. 147, No. 1, p. 242, 1966.

3-29. J. R. Parsons, R. W. Balluffi, and J. S. Koehler, "Direct Observation of Neutron Damage in Germanium," *Applied Physics Letters*, Vol. 1, No. 3, p. 57, 1962.

3-30. D. P. Miller and H. L. Taylor, "Nuclear Particle Tracks in Silicon," *Applied Physics Letters*, Vol. 2, No. 2, p. 33, 1963.

3-31.   F. L. Vook, *Radiation Effects in Semiconductors*, Plenum Press,
        N.Y., 1968.

3-32.   V. S. Vavilov, *Effects of Radiation on Semiconductors*, Consultant
        Bureau, N.Y., 1965.

3-33.   L. W. Aukerman, "Radiation-Produced Energy Levels in Compound
        Semiconductors," *Journal of Applied Physics*, Vol. 30, p. 1239,
        August 1959.

3-34.   E. I. Blount, "Energy Levels in Irradiated Germanium," *Journal of*
        Applied Physics, Vol. 30, p. 1218, August 1959.

3-35.   L. W. Aukerman, "Electron Irradiation of Indium Antimonide,"
        Physical Review, Vol. 115, No. 5, p. 1125, 1959.

3-36.   L. W. Aukerman and K. Lark-Horovitz, "Electron Bombardment of In-
        dium Antimonide," *Bulletin, American Physical Society*, Vol. 1,
        p. 332, 1956.

3-37.   F. H. Eisen, "Recovery of Electron-Radiation Damage in p-type
        InSb," *Bulletin, American Physical Society*, Vol. 7, p. 187, 1962.

3-38.   H. J. Stein, "Fast Neutron Radiation of InSb," *Bulletin, American*
        Physical Society, Vol. 7, p. 543, 1962.

3-39.   L. K. Vodopyanov and N. I. Kurdiani, "Electrical Properties of
        Indium Antimonide Irradiated by Neutrons at 77°K and by Electrons
        at 300°K," *Soviet Physics--Solid State*, Vol. 7, p. 2224, 1966.

3-40.   J. W. Cleland and J. H. Crawford, "Neutron Irradiation of Indium
        Antimonide," *Physical Review*, Vol. 95, No. 5, p. 1177, 1954.

3-41.   J. W. Cleland and J. H. Crawford, "Radiation Effects in Indium
        Antimonide," *Physical Review*, Vol. 93, p. 894, 1954.

3-42.   R. A. Laff and H. Y. Fan, "Carrier Lifetime in Indium Antimonide,"
        Physical Review, Vol. 121, p. 53, 1961.

3-43.   F. L. Vook, "Change in Thermal Conductivity upon Low-Temperature
        Electron Radiation: InSb," *Physical Review*, Vol. 135, No. 6A, p.
        A1750, 1964.

3-44.   F. L. Vook, "Thermal Conductivity of Electron-Irradiated InSb,"
        Physical Review, Vol. 149, No. 2, p. 631, 1966.

3-45.   F. H. Eisen, "Recovery of Electron Radiation Damage in n-Type
        InSb," *Physical Review*, Vol. 123, No. 3, p. 736, 1961.

3-46.   F. H. Eisen, "Orientation Dependence of Electron Radiation Damage
        in InSb," *Physical Review*, Vol. 135, No. 5A, p. A1394, 1964.

3-47. F. H. Eisen, "Model for Stage II Defects in InSb," *Bulletin, American Physical Society*, Vol. 9, p. 290, 1964.

3-48. F. H. Eisen, "Carrier-Concentration Dependence of Recovery in Electron-Irradiated InSb," *Bulletin, American Physical Society*, Vol. 8, p. 235, 1963.

3-49. N. I. Kurdiani, "Annealing of Radiation Defects and the Electron Mobility in Indium-Antimonide Irradiated with Fast Neutrons," *Soviet Physics--Semiconductors*, Vol. 3, No. 11, p. 1415, 1970.

3-50. T. W. Kim, V. D. Deokar, and W. W. Grannemann, "Radiation Effects on Electron-Beam Evaporated High Mobility Indium Antimonide Thin Films," 142nd National Meeting, The Electrochemical Society, Electronics Division, Miami Beach, Florida, October 12, 1972.

SILICON AND GaAsP METAL-INSULATOR-SEMICONDUCTOR CAPACITORS
AND Te THIN-FILM TRANSISTORS

The metal-insulator-semiconductor (MIS) capacitor is the most useful device in the study of semiconductor surfaces. Since the reliability and stability of all semiconductor devices are intimately related to their conditions, an understanding of the surface physics with the help of MIS capacitors is of great importance to device operations.

The insulated-gate thin-film transistor (IGTFT) was fabricated by Weimer (Reference 4-1) in 1961. These devices used evaporated semiconductor, metal, and insulator layers to form an IGTFT, and all processes had been done in the vacuum system with the help of precisely designed metal masks. Since the semiconductor layer is formed by deposition, more defects and crystalline imperfections in the layer than in the corresponding single-crystal semiconductor are expected. This results in more complicated transport processes in the TFT.

Metal-Insulator-Semiconductor Capacitors

Ideal MIS Capacitor

The ideal MIS capacitor theory serves as a foundation to understand practical MIS structures and to explore the physics of semiconductor surfaces. The MIS structure is shown in Figures 4-1 and 4-2, and the energy band diagram is shown in Figure 4-3. An ideal MIS capacitor is defined as follows:

(a) at $V_G = 0$ there is no energy difference between the metal work function ϕ_m and the semiconductor work function ϕ_s, or the work function difference ϕ_{ms} is zero:

$$\phi_{ms} \equiv \phi_m - \phi_s \equiv \phi_m - \left(\chi_s + \frac{E_G}{2q} - \phi_B\right) = 0 \text{ for n-type}$$

$$\phi_{ms} \equiv \phi_m - \left(\chi_s + \frac{E_G}{2q} + \phi_B\right) = 0 \text{ for p-type}$$
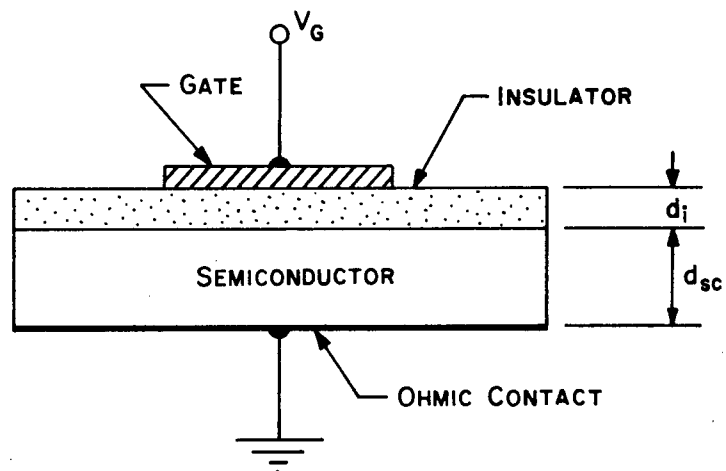
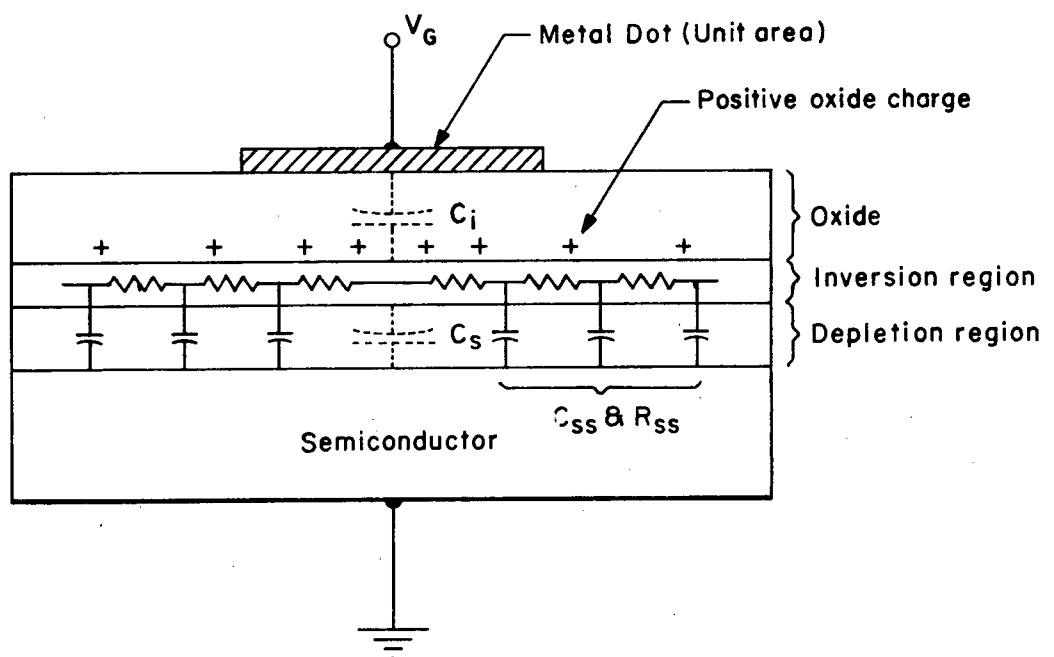Figure 4-1.   Metal-Insulator-Semiconductor Structure

Figure 4-2.   MIS Model with an Extrinsic Inversion Layer
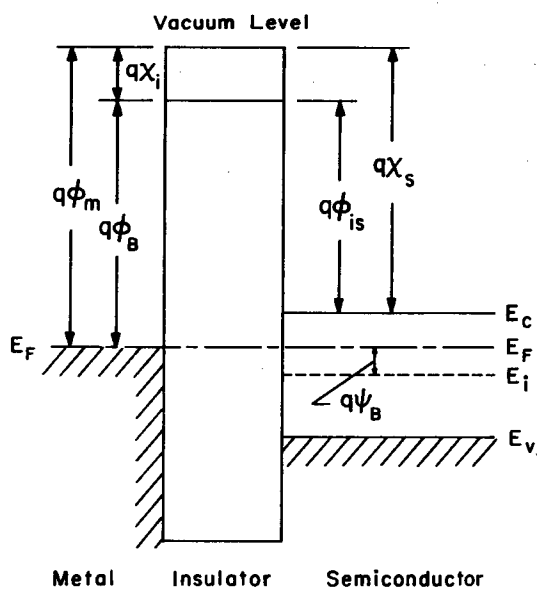Coupled Conductively to the Intrinsic Layer

(a) MIS diode at $V_G = 0$
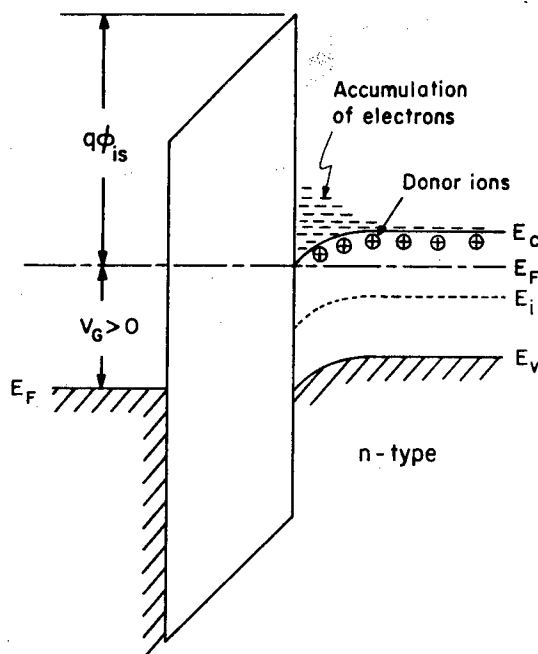
(b) $V_G > 0$
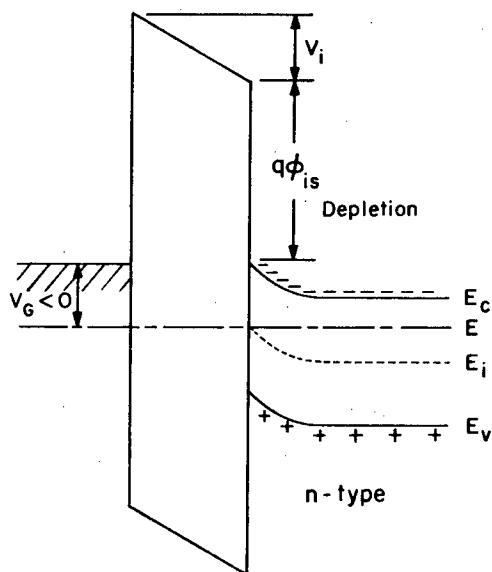
(c) $V_G < 0$
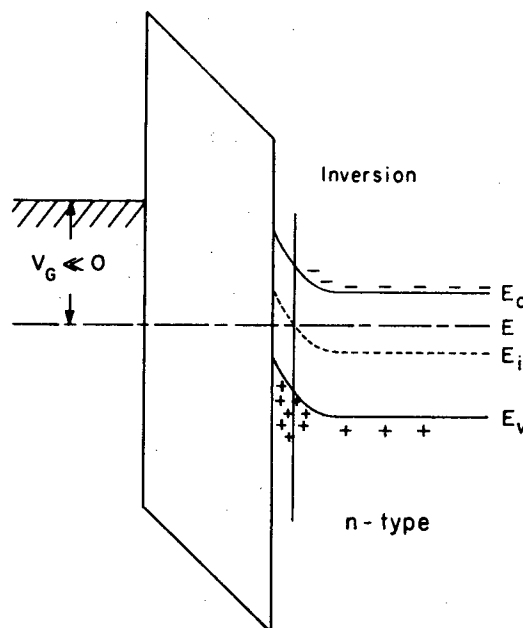
(d) $V_G \ll 0$

Figure 4-3. Energy Band Diagrams of the Metal-Insulator-
Semiconductor n-Type Device for Different Gate Voltages

81

$$\phi_m = \phi_B + \chi_i$$

$$\chi_s = \phi_{is} + \chi_i$$

$$\phi_s = \chi_s + \frac{E_G}{2q} \pm \phi_B$$

where

ϕ_m = metal work function

χ_s = semiconductor electron affinity

χ_i = insulator electron affinity

E_G = energy gap

ϕ_B = potential barrier between the metal and the insulator

ϕ_B = potential difference between the Fermi level E_F and the in-
trinsic Fermi level E_i

ϕ_s = semiconductor work function

ϕ_{is} = potential difference between the insulator and semiconduc-
tor conduction band edges

(b) the only charges which can exist in the structure under any
biasing conditions are those in the semiconductor and those
with the equal but opposite sign on the metal surface adja-
cent to the insulator

(c) there is no carrier transport through the insulator under DC
biasing conditions, or the resistivity of the insulator is
infinity.

Clean Surface Study—(Surface Potential, Electric Field, Surface Charges, Space Charges, and Surface States)

In the MIS study, the relation between the surface potential,
space charge, and electric field is very important and will be used to
derive the capacitance-voltage characteristics of the ideal MIS struc-
ture. The band diagram at the surface of an n-type semiconductor is
shown in Figure 4-4.

(I) Accumulation : $\psi_s > 0$

(II) Depletion : $|\psi_B| > |\psi_s| > 0$

(III) Inversion : $|\psi_s| > |\psi_B|$

(IV) Flat band : $\psi_s = 0$

(a)

Band Diagram

E_F

$V_G < 0$

$q\psi_s$

n_{n_o}

E_c

E_F

$q\psi_B$

E_i

$+$
$++$
$++$

p_{n_o}

E_v

$\rho(x)$

$+Q_p$

Q_s

$+qN_D$

$-d$

o

W

x

$-Q_M$

(b)

Charge Distribution

$\mathcal{E}(x)$

$-d$

o

W

x

$\dfrac{|Q_s|}{\epsilon_i}$

(c)

Electric Field

$\psi(x)$

$-d$

o

W

x

ψ_s

V_G

V_i

(d)
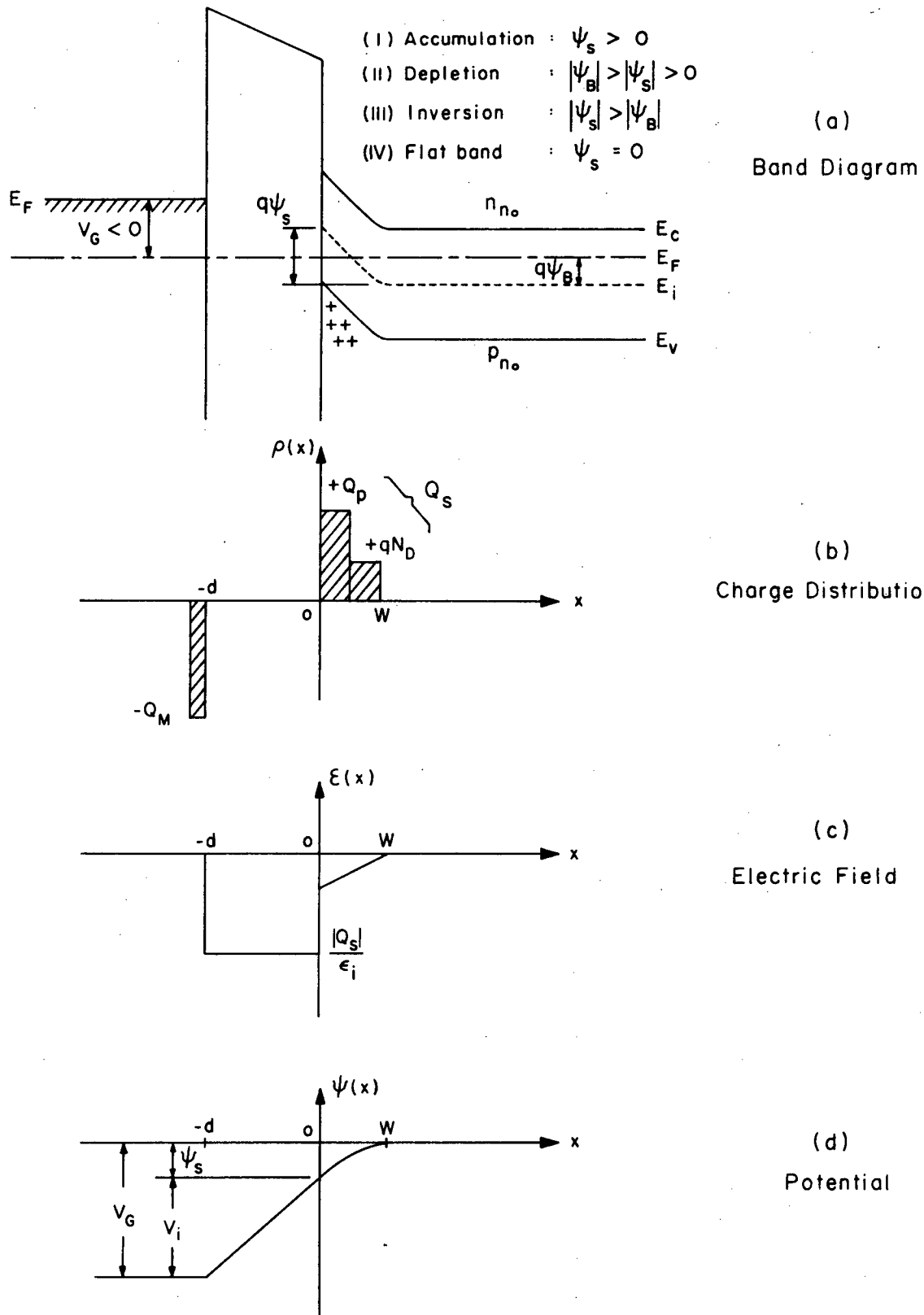
Potential

Figure 4-4. Electrical Diagrams Obtained in the MIS Device

The potential near and at the surface as a function of distance can be obtained by using the Poisson's equation (References 4-2 and 4-3)

$$\frac{\partial^2 \phi}{\partial x^2} = -\frac{\rho(x)}{\varepsilon_s}$$

where

ϕ = potential function

ε_s = permittivity of the semiconductor

$\rho(x)$ = total space charge density

$\rho(x) = q(N_D^+ - N_A^- + P_n - n_n)$

N_D^+ = ionized donor density

N_A^- = ionized acceptor density

$P_n = P_{no} e^{-\beta\phi}$

$n_n = n_{no} e^{\beta\phi}$

P_{no} = equilibrium densities of holes in the n-type bulk

n_{no} = equilibrium densities of electron in the n-type bulk

$\beta \equiv \frac{q}{kT}$

Solving the Poisson's equation, the following important set of results is obtained:

(a) Electric field at the surface

$$E = -\frac{2kT}{qL_D} F\left(\beta\phi, \frac{P_{no}}{n_{no}}\right)$$

$$E_s = -\frac{2kT}{qL_D} F\left(\beta\phi_s, \frac{P_{no}}{n_{no}}\right)$$

where

L_D $\equiv$ extrinsic Debye length

ϕ_s = surface potential

84

$$L_D = \sqrt{\frac{2kT\varepsilon_s}{n_{no}q^2}} = \sqrt{\frac{2\varepsilon_s}{qn_{no}\beta}}$$

$$F\left(\beta\phi, \frac{P_{no}}{n_{no}}\right) \equiv \left[\frac{P_{no}}{n_{no}}(e^{-\beta\phi} + \beta\phi - 1) + (e^{\beta\phi} - \beta\phi - 1)\right]^{1/2}$$

(b) Space charge per unit area

$$Q_s = \varepsilon_s E_s = \frac{2\varepsilon_s kT}{qL_D} F\left(\beta\phi_s, \frac{P_{no}}{n_{no}}\right)$$

(c) Change of hole and electron densities

$$\Delta P = P_{no} \int_0^\infty (e^{-\beta\phi} - 1)\,dx$$

$$\Delta P = \frac{qP_{no}L_D}{2kT} \int_{\phi_s}^0 \frac{(e^{-\beta\phi} - 1)}{F\left(\beta\phi, \frac{P_{no}}{n_{no}}\right)}\,d\phi \quad (cm^{-2})$$

$$\Delta n = n_{no} \int_0^\infty (e^{\beta\phi} - 1)\,dx$$

$$\Delta n = \frac{qn_{no}L_D}{2kT} \int_{\phi_s}^0 \frac{(e^{\beta\phi} - 1)}{F\left(\beta\phi, \frac{P_{no}}{n_{no}}\right)}\,d\phi \quad (cm^{-2})$$

(d) Strong inversion at a surface potential

$$\phi_s = 2\phi_B = \frac{2kT}{q} \ln\left(\frac{N_D}{n_i}\right)$$

(e) Differential capacitance of the space charge region

$$C_D \equiv \frac{\partial Q_s}{\partial \phi_s} = \frac{\varepsilon_s}{L_D} \frac{\left[1 - e^{-\beta\phi_s} + \frac{P_{no}}{n_{no}}(e^{\beta\phi_s} - 1) \right]}{F\left(\beta\phi_s, \frac{P_{no}}{n_{no}}\right)} \; \text{farad/cm}^2$$

At flat-band, $\phi_s = 0$

$$C_D \text{ (flat band)} = \frac{\varepsilon_s}{L_D} \sqrt{2} \; \text{farad/cm}^2$$

(f) Charge neutrality of the system

$$Q_M = Q_s = Q_p + qN_DW$$

where

Q_M = charges per unit area on the metal

Q_s = total charges per unit area in the semiconductor

Q_p = inversion region charge per unit area

qN_DW = ionized donor charge per unit area in the space charge region
with space-charge width W

(g) Potential distribution

$$V_G = V_i + \phi_s = -\frac{Q_s}{C_i} + \phi_s$$

where

V_i = potential across the insulator

$$V_i \equiv -\frac{Q_s d_i}{\varepsilon_i} = -\frac{Q_s}{C_i}$$

$$C_i \equiv \frac{\varepsilon_i}{d_i}, \text{ insulator capacitance}$$

(h) Total capacitance of the system

$$C = \frac{C_i C_D}{C_i + C_D}$$

where

C_i = constant capacitance of insulator or maximum capacitance of the system

C_D = space-charge capacitance or depletion region capacitance

For flat-band condition,

$$C_{FB}(\phi_s = 0) = \frac{\varepsilon_i}{d_i + \frac{L_D}{\sqrt{2}}\left(\frac{\varepsilon_i}{\varepsilon_s}\right)} = \frac{\varepsilon_i}{d_i + \left(\frac{\varepsilon_i}{\varepsilon_s}\right)\sqrt{\frac{kT\varepsilon_s}{n_{no}q^2}}}$$

The equation for the normalized MIS capacitance under depletion conditions is expressed as

$$\left(\frac{C}{C_i}\right) = \left(1 - \frac{2C_i^2 V_G}{qN_D \varepsilon_s}\right)^{-1/2}$$

This equation explains that the normalized capacitance will fall with the square root of the gate voltage, for sufficiently negative values of V_G, as the surface is being depleted. The (C/C_i) value for high frequency is given by

$$\left(\frac{C}{C_i}\right) = \left(1 - \frac{2C_i^2 V_G'}{qN_D \varepsilon_s}\right)^{-1/2}$$

where

$$V_G' = V_G - \phi_{ms} + \frac{Q_{ss}}{C_i} = V_G - V_{FB}$$

$$V_{FB} \equiv \phi_{ms} - \frac{Q_{ss}}{C_i} \quad \text{(flat-band voltage)}$$
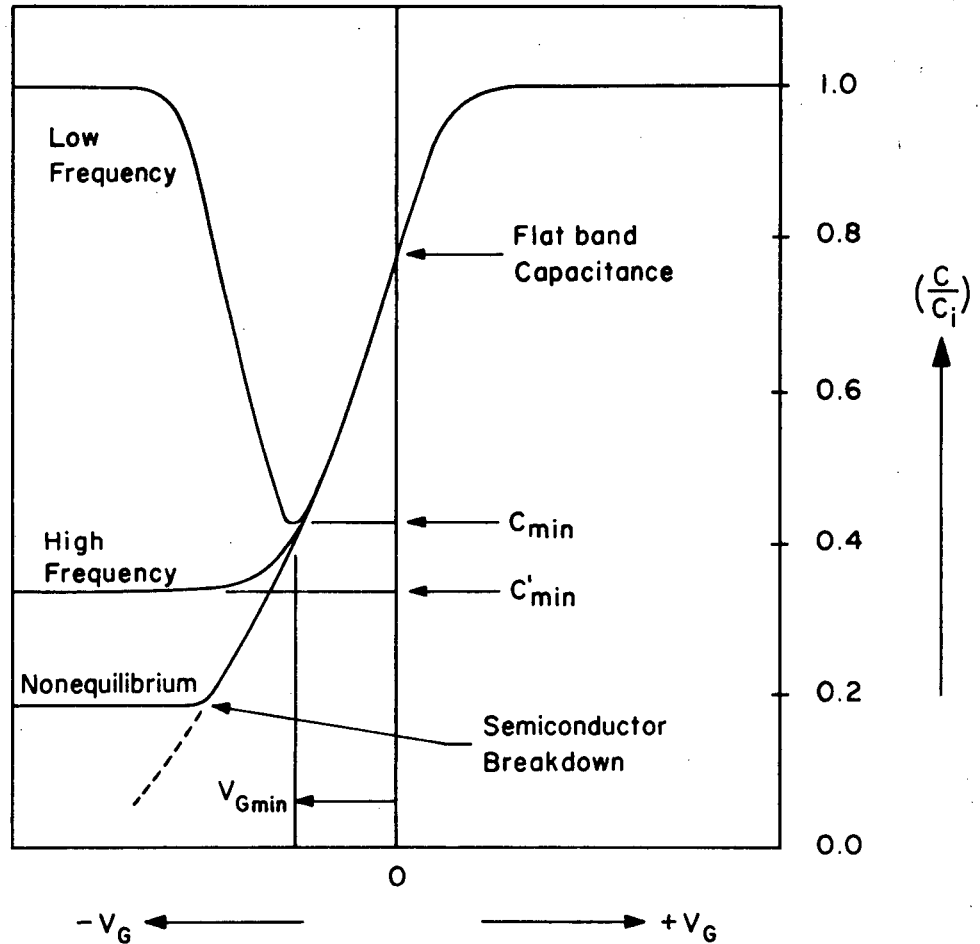
Figure 4-5. MIS Capacitance-Voltage Curves for n-Type Semiconductor

The capacitance-voltage curves for the MIS device are shown in Figure 4-5. In describing this curve, at the right side (positive voltage) where there is an accumulation of electrons, a high differential capacitance of the semiconductor is observed. As a result the total capacitance is close to the insulator capacitance, C_i. As the positive voltage V_G is reduced sufficiently, a depletion region acting as a dielectric in series with the insulator is formed near the semiconductor surface, and the total capacitance decreases. The capacitance goes through a minimum and then increases again as the inversion layer of holes forms at the surface. The increase of the capacitance is dependent on the ability of the hole (or electron) concentration to follow the

applied AC signal. This is only possible at low frequencies where the recombination-generation rates of minority carriers (holes in n-type) can keep up with the small signal variation and lead to charge exchange with the inversion layer in step with the measurement signal. As a consequence, MIS curves measured at higher frequencies do not show the increase of capacitance on the left side. The capacitance curve under a nonequilibrium condition is one of pulse condition.

Surface State Study

In a practical MIS device, there exist many other states and charges which affect the ideal MIS characteristics. They are shown in Figure 4-6 and are as follows:

(a)   Surface states or interface states

(b)   Fixed surface charges

(c)   Mobile ions

(d)   Ionized traps

In a practical system the following charge neutrality holds

$$Q_G + Q_s + Q_{ss} = 0$$

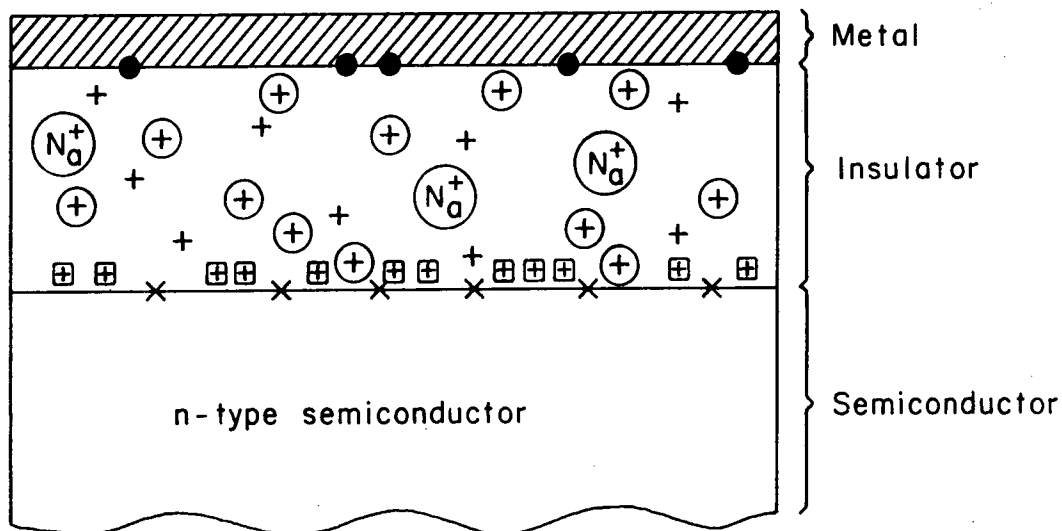where

Q_{ss} = surface state (inter-state) charge

Q_s = space charge

From Figure 4-2, the input admittance is expressed as (Reference 4-3)

$$Y_{in} \equiv G_{in} + j\omega C_{in}$$

where

$$G_{in} = \frac{\omega^2 C_{ss} \tau C_i^2}{(C_i + C_s + C_{ss})^2 + \omega^2 \tau^2 (C_i + C_s)^2}$$

Figure 4-6. Basic Classification of States and Charges in a non-Ideal MIS Device (Reference 4-4)

$$C_{in} = \frac{C_i}{C_i + C_s + C_{ss}} \left[C_s + C_{ss} \frac{(C_i + C_s + C_{ss})^2 + \omega^2 \tau^2 C_s (C_i + C_s)}{(C_i + C_s + C_{ss})^2 + \omega^2 \tau^2 (C_i + C_s)^2} \right]$$

$$C_s = -\frac{\partial Q_s}{\partial \phi_s}, \text{ space charge capacitance}$$

$$C_{ss} = -\frac{\partial Q_{ss}}{\partial \phi_s}, \text{ surface state capacitance}$$

τ = time constant of surface state

Since C_{ss} is independent of the V_G, the C_{ss} can be set equal to zero for the ideal MIS device. Hence

$$C_{in} = \frac{C_i C_s}{C_i + C_s}$$

To evaluate the surface-state density, the capacitance measurement or the conductance measurement can be used since both C_{in} and G_{in} contain similar information about the surface states. For MIS devices with relatively low surface-state densities ($\sim 10^{10}$ states/cm^2/eV) the conductance method can give the most accurate results. By differentiation, integration, or temperature procedures, the evaluation of surface-state density using capacitance measurement can be achieved (References 4-3 and 4-4).

$$Q_{ss} = C_i \Delta V_G \quad \text{coul/cm}^2$$

$$N_{ss} = \frac{1}{q} \left(\frac{\partial Q_{ss}}{\partial \phi_s} \right)_{V_G} \quad \text{states/cm}^2/\text{eV}$$

where

ΔV_G = gate voltage shift

N_{ss} = surface-state density per unit energy

In the capacitance measurement, the difficulty arises from the fact that the surface-state capacitance must be extracted from the

measured capacitance which consists of C_i, C_s, and C_{ss}. Since both the capacitance and conductance as functions of voltage and frequency contain identical information about surface state, greater inaccuracies arise in extracting this information from the measured capacitance. This difficulty does not apply to the measured conductance which is measured simultaneously in a standard capacitance bridge, because it is directly related to the surface states. Thus conductance measurements yield more accurate and reliable results, particularly when N_{ss} is low. The frequency-dependent capacitance in parallel with a frequency-dependent conductance, the frequency-independent capacitance of the insulator, and their relation are expressed as (Figure 4-7)
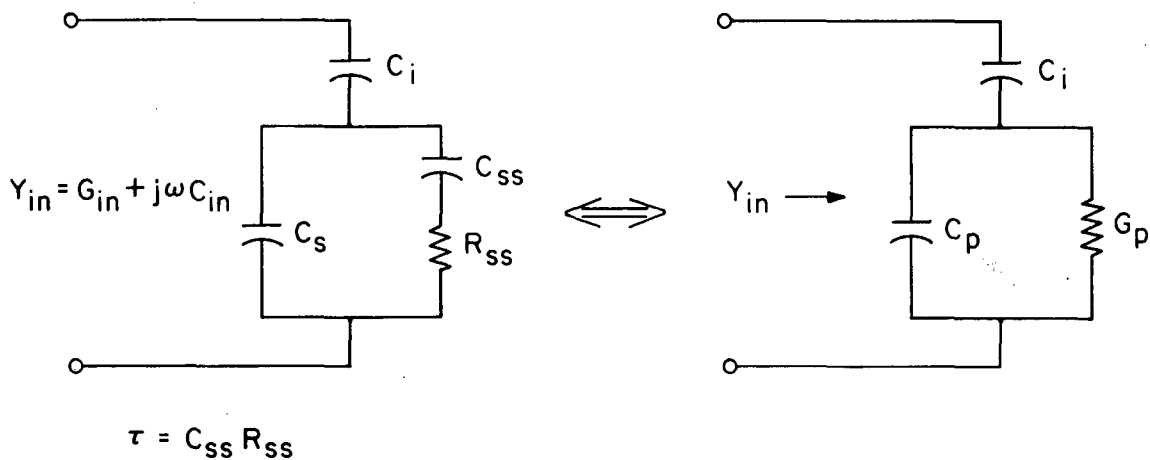

$$\tau = C_{ss} R_{ss}$$

Figure 4-7. Equivalent Circuits of MIS Devices

$$C_p = C_s + \frac{C_{ss}}{1 + \omega^2 \tau^2}$$

$$G_p = \frac{C_{ss} \omega^2 \tau}{1 + \omega^2 \tau^2}$$

where

$$\tau \equiv C_{ss} R_{ss}$$

R_{ss} = resistance associated with surface states

Since the G_p expression does not contain C_s and depends only on the surface-state branch of the equivalent circuit (Figure 4-7), the C_{ss} can be obtained directly from G_p measurement.

$$N_{ss} = \frac{C_{ss}}{qA}$$

where

A = gate plate area

C-V Characteristics of GaAsP and Silicon MIS Capacitors

Commercially available (100) $GaAs_{1-x}P_x$ material with a phosphorus mole fraction of x = 50±2 percent was used. The 4-mil-thick GaAsP epitaxial layer was tellurium doped to a donor concentration of 2×10^{15} atoms/cc or 3×10^{15} atoms/cc. The energy gap of GaAsP is 1.95 eV. The epitaxial layer was grown on a 15-mil-thick GaAs substrate. The substrate dopant was tellurium ($N_D \approx 7 \times 10^{17}$ atoms/cc) and the resistivity was 0.003 Ω-cm. The energy gap of GaAs is 1.4 eV. The intrinsic carrier concentration, n_i, is ~3×10^{15} carriers/cc. The electron mobility for real $GaAs_{1/2}P_{1/2}$ samples lies in the range of 326 to 1,200 cm^2/V-sec, while the hole mobility lies in the range of 60 to 250 cm^2/V-sec. A very rough estimation of electron-to-hole mobility ratios of 10 was made (Reference 4-5). The dielectric constant of $GaAs_{1/2}P_{1/2}$ is 11.35 and a value of ϵ_s for $GaAs_{1/2}P_{1/2}$ is 10^{-12} F/cm. Unfortunately, the properties of GaAsP are not well known.

The GaAsP MIS capacitors were fabricated on electron-beam evaporated Al_2O_3 by evaporating aluminum gate and following with helium and oxygen annealing. The fabrication processes are detailed in Appendix B.

The C-V characteristics of stable GaAsP MIS capacitors are shown in Figure 4-8. The hysteresis loop is also recorded to evaluate the stability of the capacitor. The depletion characteristic rather than inversion is measured for GaAsP MIS capacitors. This characteristic could be caused by a shortage of minority carriers in the bulk or at the
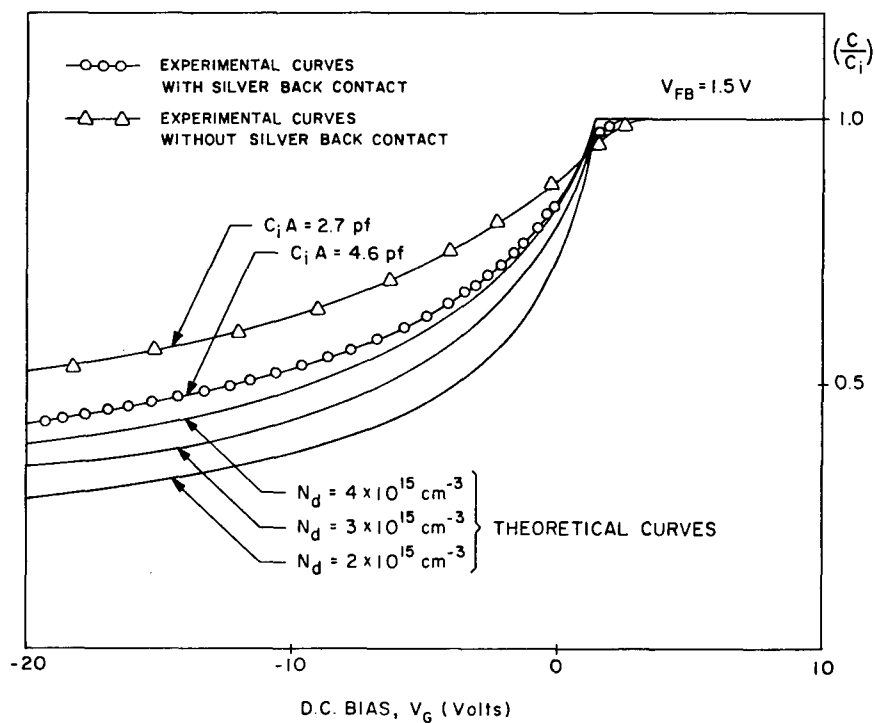
Figure 4-8. C-V Characteristics of Al-Al$_2$O$_3$-GaAs$_{1/2}$P$_{1/2}$ Capacitors by Using Electron-Beam Evaporation Technique
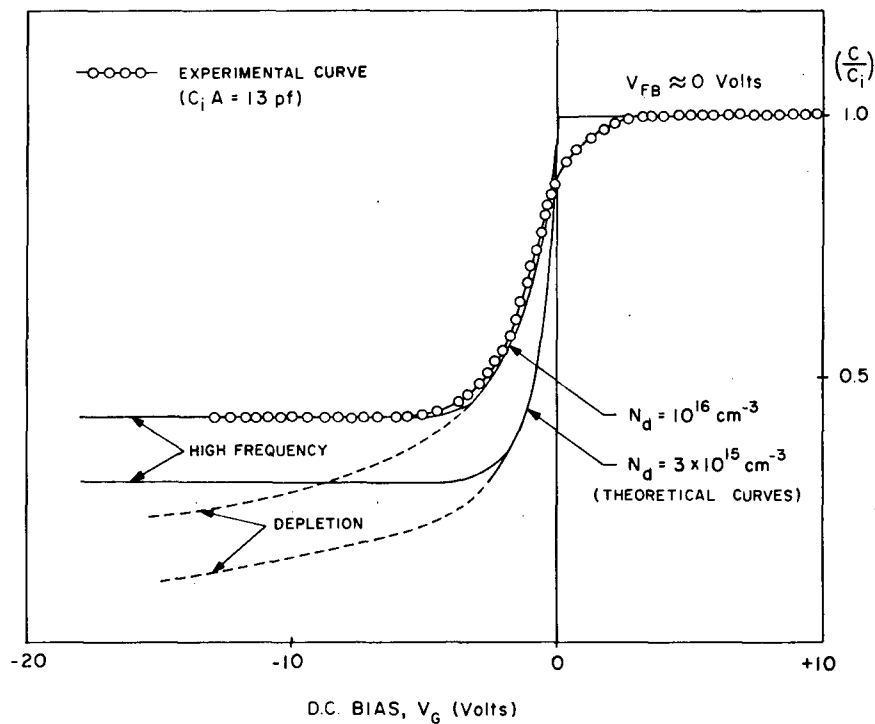

Figure 4-9. C-V Characteristics of Al-Al$_2$O$_3$-Si Capacitors by Using Electron-Beam Evaporation Technique

interface and/or by ineffectiveness of the minority carriers because of their low mobility (Reference 4-5). It is instructive to relate the results of GaAsP MIS capacitors to the silicon. The C-V characteristics of the Al-Al$_2$O$_3$-Si capacitors do not show the depletion behavior (Figure 4-9).

In order to evaluate the fabricated MIS capacitors, the surface-state charge density, Q_{ss}, and the surface-state density, $\tilde{N}_{ss}$, should be calculated. If a value of $\chi_s = 4$ is assumed for GaAs$_{1/2}$P$_{1/2}$ and the value of ϕ_m is 4.25 for aluminum, ϕ_{ms} is estimated to be 0.25 volt. From the flat-band voltage of $V_{FB} = 1.5$ V (Figure 4-8) and $C_i = 9.4 \times 10^{-9}$ F/cm^2 (Al$_2$O$_3$), the Q_{ss} can be obtained as

$$Q_{ss} = -(V_{FB} - \phi_{ms})C_i = -1.175 \times 10^{-8} \text{ coul/cm}^2$$

From the above value, the surface-state density $\tilde{N}_{ss}$ is calculated as

$$\tilde{N}_{ss} = \frac{|Q_{ss}|}{q} = 7.35 \times 10^{10} \text{ states/cm}^2$$

For the Al-Al$_2$O$_3$-Si capacitor (Figure 4-9), the value of χ_s is 4, the ϕ_{ms} value is 0.25, and the V_{FB} is 0.8; therefore

$$Q_{ss} = -5.21 \times 10^{-9} \text{ coul/cm}^2$$

$$\tilde{N}_{ss} = 3.26 \times 10^{10} \text{ states/cm}^2$$

The stability of the capacitors was excellent because there is no change in C-V curves even after several to several dozen sweeps. The small area of hysteresis loop also indicates good drifting characteristics.

The theoretical C-V curves are plotted in Figure 4-8, using the following formula:

$$\left(\frac{C}{C_i}\right)_D = \left[1 - \frac{2C_i^2(V_G - V_{FB})}{q\varepsilon_s N_D}\right]^{-1/2}$$

95

For the inversion regime (e.g., Si-Al$_2$O$_3$-Al), the value of (C/C$_i$) for high frequency can be calculated by using the formula

$$\left(\frac{C}{C_i}\right)_{INV} = \frac{1}{1 + \frac{\varepsilon_i d_d}{\varepsilon_s d_i}}$$

where

$$d_{dmax} \approx \sqrt{\frac{10^{15}}{|N|}} \quad \text{in microns}$$

The electron-beam evaporated Al$_2$O$_3$ insulator has been evaluated through thermal annealing and electrical measurement. Before thermal annealing, a large number of charged ions in the insulator was observed by measuring the C-V curves. Annealing in helium ambient (1 liter/min) for 20 minutes and in oxygen (1 liter/min) for 40 minutes at 225-250°C resulted in excellent C-V characteristics as shown in Figures 4-10(a) and 4-11 (References 4-6, 4-7, and 4-8). The hysteresis loop was almost completely removed, and the C-V curve was very stable even after several hundred sweeps. Annealing in O$_2$ at 420°C for 15 minutes introduced many pinholes on the insulator and the C-V characteristic was worse as shown in Figure 4-10(b). A temperature of 250°C is the maximum limit for attaining good results. An evaporation rate of 60 Å/min showed excellent results consistently; however, 200 Å/min resulted in increasing the capacitance value near the bending point (C/C$_i$ = 1) as shown in Figure 4-10(c). An insulator thickness of 2,500 Å (rate 60 Å/min) induced good resistivity and breakdown voltage characteristics; however, the capacitance change in C-V curves was not sufficient (Figure 4-10(d)). The typical values of resistivity and breakdown voltage of the electron-beam evaporated Al$_2$O$_3$ films ranged from 10^{13} to 10^{14} ohm-cm and from 2.2 x 10^6 to 2.8 x 10^6 V/cm, respectively.

(C/C₀)

Left plot:
$C_o = 5.2$ pf
1.0

0.5

Sample S-1922, n-type GaAs$_{1/2}$P$_{1/2}$
on GaAs Substrate

Insulator: E-beam deposited Al$_2$O$_3$
(1,600 Å thick)
Gate: Aluminum

Sweep Time: 100 seconds

Test Frequency: 1 MHz

Rate of Deposition: 60 Å/min

-15 -10 -5 0 5 10
V (volts)

Right plot:
(C/C₀)
$C_o = 5.9$ pf
1.0

shift

Sample S-1922, n-type GaAs$_{1/2}$P$_{1/2}$
on GaAs substrate

Insulator: E-beam deposited Al$_2$O$_3$
(1,600 Å thick)
Gate: Aluminum

Sweep Time: 100 seconds

Test Frequency: 1 MHz

Annealed at 420°C for 15 minutes
in O$_2$

-15 -10 -5 0 5 10 15
V (volts)

Figure 4-10. Capacitance-Voltage Characteristics of GaAs$_{1/2}$P$_{1/2}$-Al$_2$O$_3$-Al Capacitors

(C/C_o)

$C_o = 4.5\ \text{pf}$

1.0

0.5

V (volts)

−15   −10   −5   0   +5   +10   +15

Sample S-1403, n-type $GaAs_{1/2}\ P_{1/2}$
on GaAs substrate

Insulator: E-beam deposited Al_2O_3
      (2,500 Å thick)

Gate: Aluminum

Sweep Time: 100 seconds

Test Frequency: 1 MHz

Rate of Deposition: 60 Å/min

(C/C_o)

1.0

0.5

V (volts)

−15   −10   −5   0   +5   +10   +15

Sample S-1702, n-type $GaAs_{1/2}\ P_{1/2}$
on GaAs substrate

Insulator: E-beam deposited Al_2O_3
      (1,600 Å thick)

Gate: Aluminum

Sweep Time: 100 seconds

Test Frequency: 1 MHz
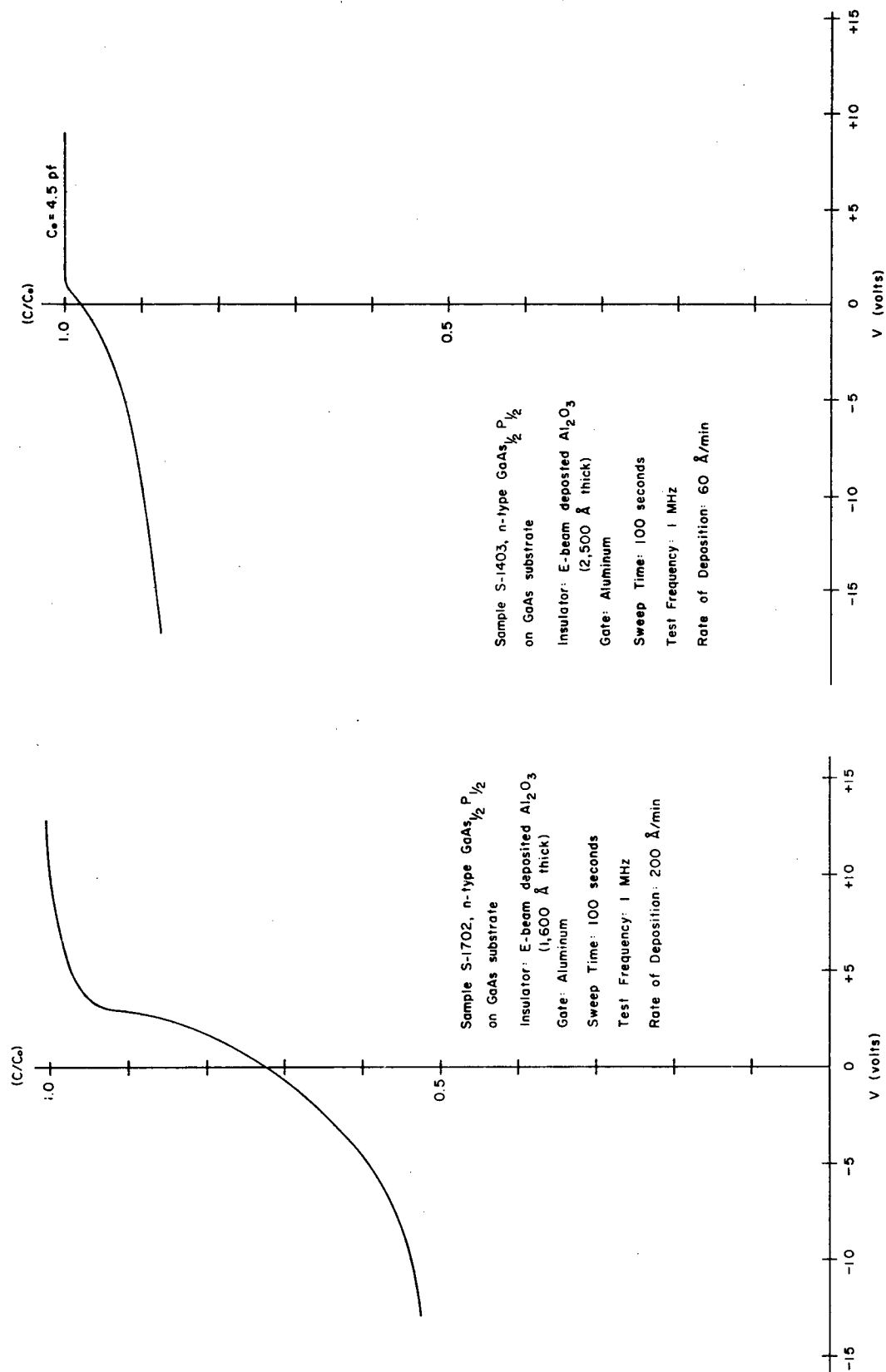
Rate of Deposition: 200 Å/min
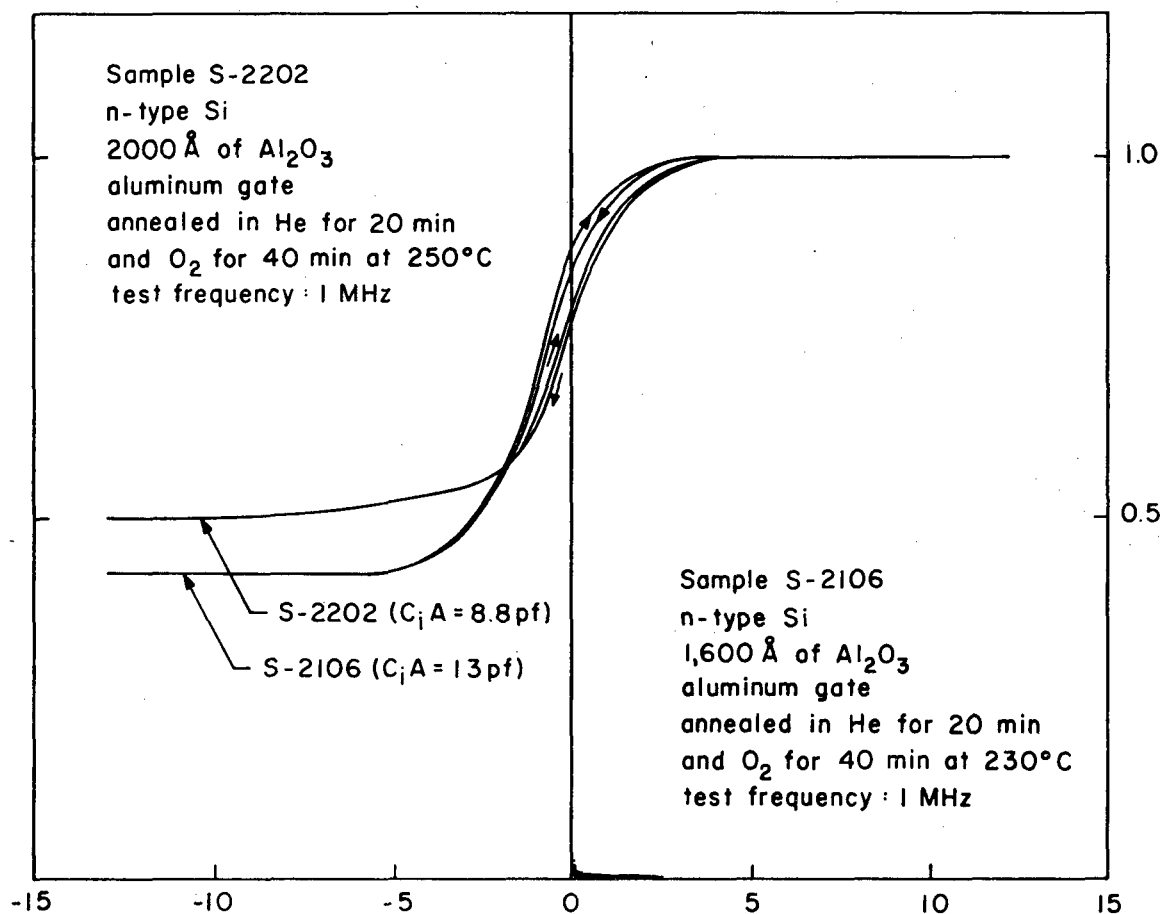
Figure 4-10. continued

98

Figure 4-11. Capacitance-Voltage Characteristics
of Si-Al$_2$O$_3$-Al Capacitors

Metal-Insulator-Semiconductor Thin-Film Transistor (MISTFT)

MIS Thin-Film Transistors

The metal-insulator-semiconductor thin-film transistor can be con-
structed in a variety of forms which are

(a) Staggered-electrode structure having the gate on top

(b) Staggered-electrode structure having the gate at the bottom

(c) Coplanar-electrode structure having the gate on top

(d) Coplanar-electrode structure having the gate at the bottom

Typically, glass, quartz, or sapphire is used as the insulating sub-
strate, CdS or CdSe as the semiconductor, gold or aluminum as the metal

electrodes, and silicon oxide (SiO_x) or aluminum oxide as the gate insulator. However, the MIS tellurium thin-film transistor with Al_2O_3 dielectric will be described. A simplified structure of the thin-film transistor is shown in Figure 4-12.
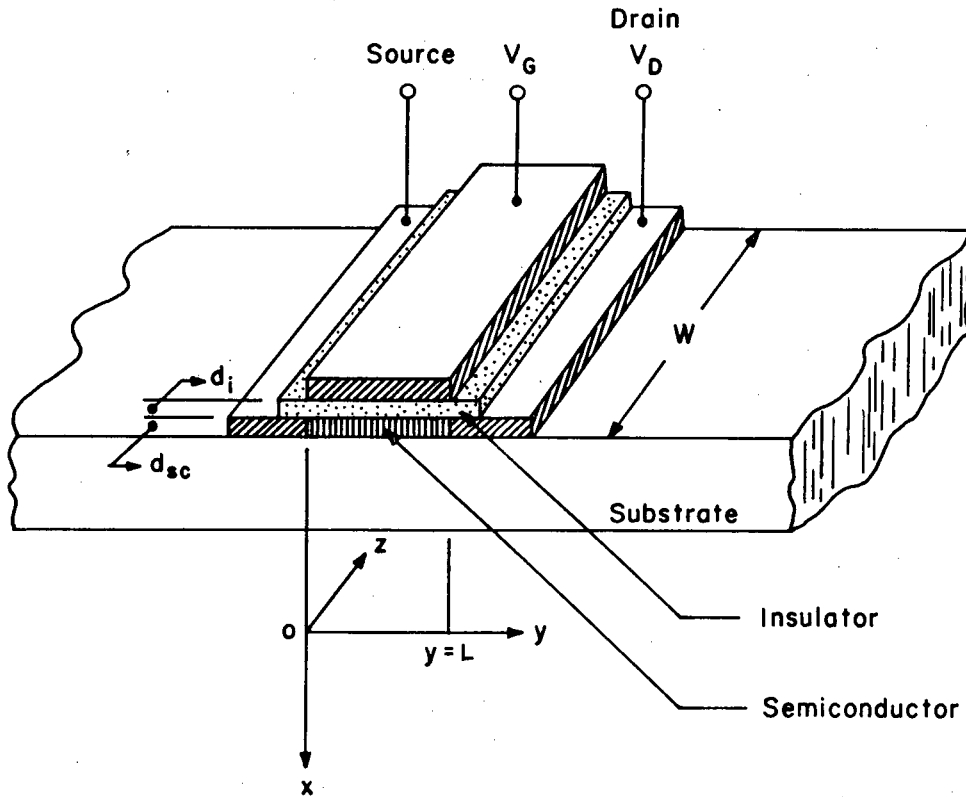

Figure 4-12.   Structure of the MISTFT

For the MISTFT without surface state, the drain current can be expressed as (Figure 4-13)

$$I_D = \left(\frac{W}{L}\right)\mu_e^* C_i \left[(V_G - V_T)V_D - \frac{V_D^2}{2} \right]$$

where

$$V_T \equiv - \frac{qn_o d_{sc}}{C_i}, \text{ threshold voltage}$$

C_i = insulator capacitance
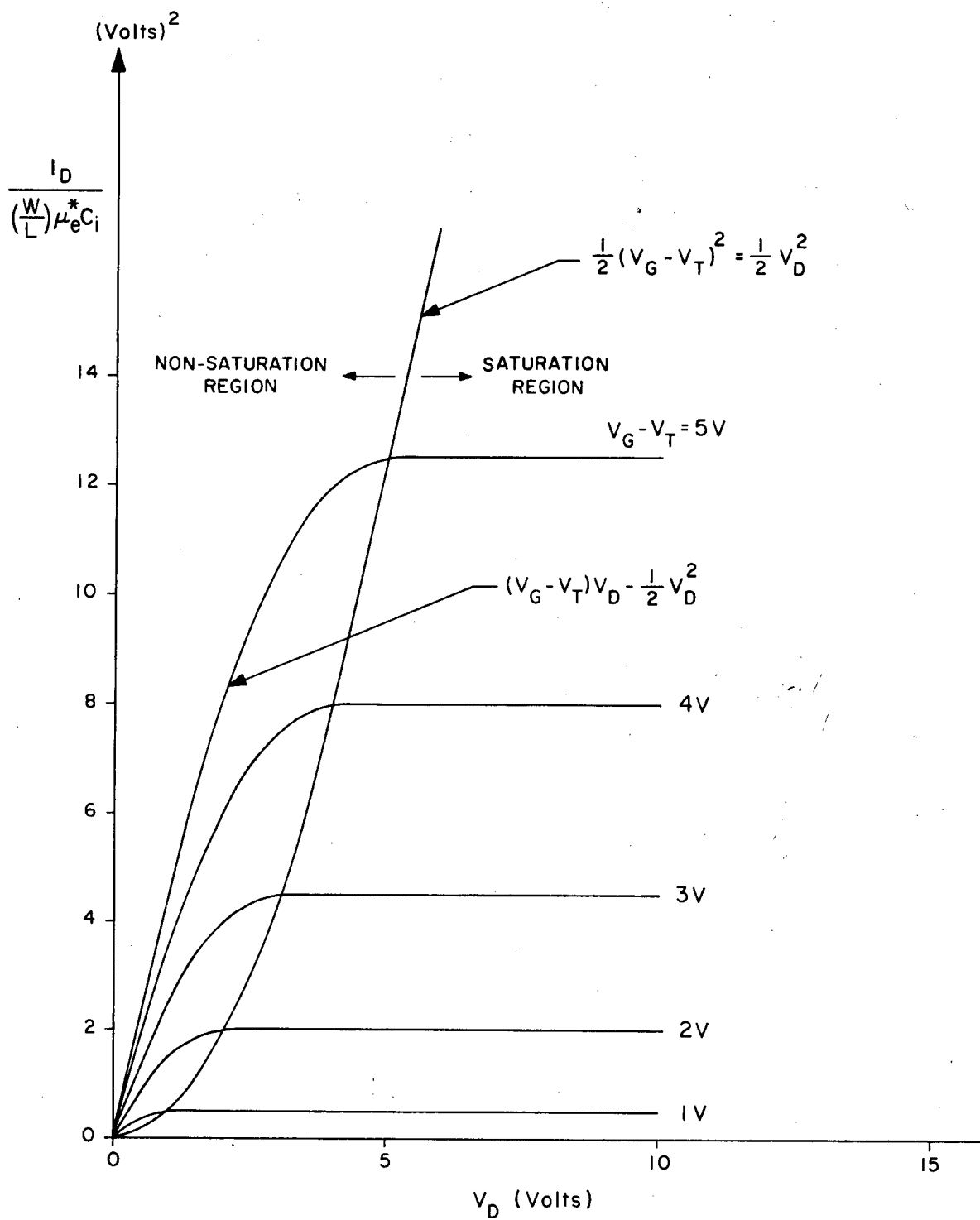
d_{sc} = semiconductor thickness

100

Figure 4-13.   Theoretical TFT Characteristic Curves

n_o = initial charge density in the semiconductor

μ_e^* = effective channel mobility

In the nonsaturation region, the drain conductance and the transconductance are given by

$$g_D \equiv \left.\frac{\partial I_D}{\partial V_D}\right|_{V_D \to 0} = \left(\frac{W}{L}\right)\mu_e^* C_i (V_G - V_T)$$

$$g_m \equiv \left.\frac{\partial I_D}{\partial V_G}\right|_{V_D} = \left(\frac{W}{L}\right)\mu_e^* C_i V_D$$

(4-1)

In the saturation region, the saturation drain current and the saturation transconductance are expressed as

$$I_{Dsat} = \left(\frac{W}{L}\right)\frac{\mu_e^* C_i}{2}(V_G - V_T)^2$$

$$g_{msat} = \left(\frac{W}{L}\right)\mu_e^* C_i (V_G - V_T) = \sqrt{\frac{2W\mu_e^* C_i I_{Dsat}}{L}}$$

since

$$V_D = V_G - V_T = V_{Dsat}$$

In the depletion-type TFT, the saturation drain current at $V_G = 0$ is

$$I_{Dsat}(V_G = 0) = \left(\frac{W}{L}\right)\left(\frac{\mu_e^* C_i}{2}\right)V_T^2 = \frac{W\mu_e^*}{2LC_i}(qd_{sc}n_o)^2$$

A figure of merit which characterizes the high-frequency performance of the TFT is the gain-bandwidth product which is equivalent to the maximum operating frequency:

$$f_m \equiv \frac{g_m}{2\pi C_i WL}$$

(4-2)

From Equations 4-1 and 4-2,

$$f_m \simeq \frac{\mu_e^* V_{Dsat}}{2\pi L^2}$$

For the nonsaturation region $(V_D < V_G - V_T)$,

$$f_m \simeq \frac{\mu_e^*}{2\pi L^2}(V_G - V_T)$$

Hofstein (Reference 4-6) presented a theoretical qualitative analysis of the behavior of the junctionless or deep depletion type MIS thin-film transistors which are different from the surface inversion conducting channel devices. This type of device is basically a depletion type transistor, although it may of course be operated in an enhancement mode. The model is illustrated in Figure 4-14. It was also shown that if an inversion layer formed at the insulator-semiconductor interface before the channel was completely depleted, then complete pinch-off of drain current by the gate would not be observed.

Deal, et al. (Reference 4-10), Heiman (Reference 4-11), and Grove, et al. (Reference 4-12) showed that saturation of drain current and pentode-like characteristics might be maintained with channels substantially deeper than the maximum depletion region depth obtainable with the drain voltage set at zero (i.e., operated as an MIS capacitor). A curve of the maximum depletion depth versus donor concentration (doping) is shown in Figure 4-15, on the basis that the maximum depletion depth is on the order of 4 to 6 Debye lengths where the Debye length is defined by

$$L_D = \sqrt{\frac{2kT\epsilon_o \epsilon_s}{e^2 N_D}}$$

Effects of Traps and Surface States on MISTFTs

The electrical characteristics of a TFT are basically identical to those of an insulated gate field effect transistor. The detailed transport processes in a TFT are more complicated. The major complication
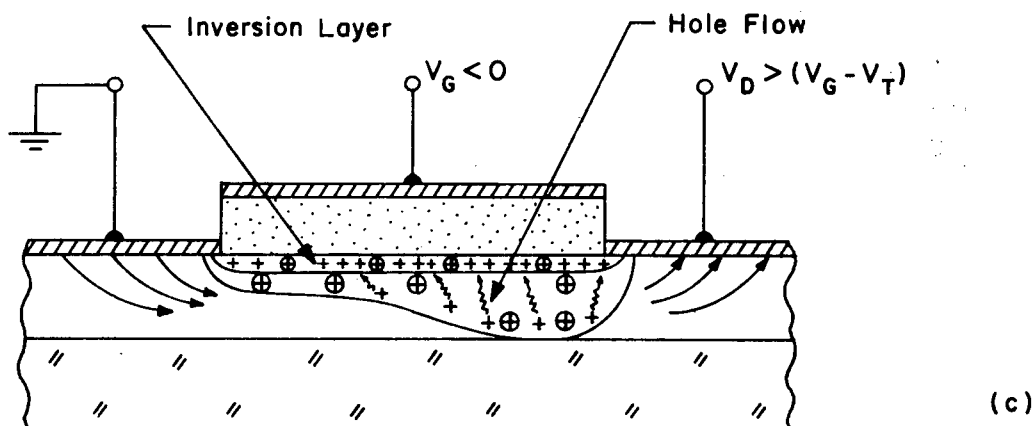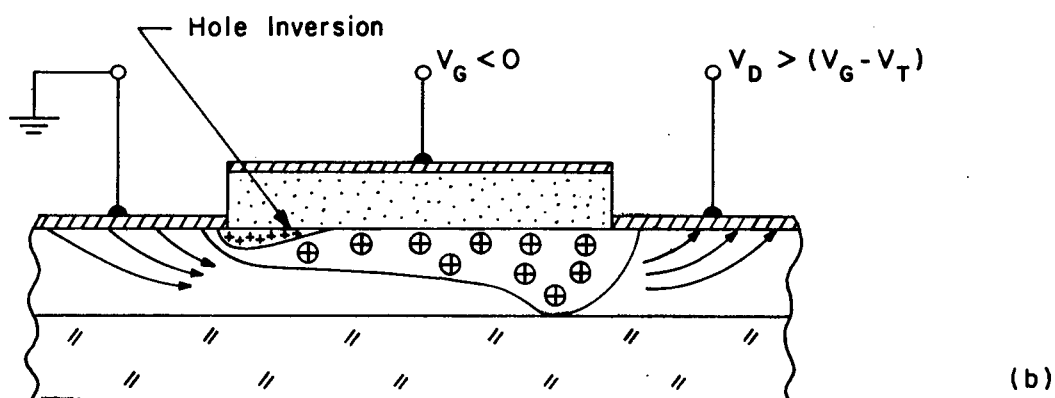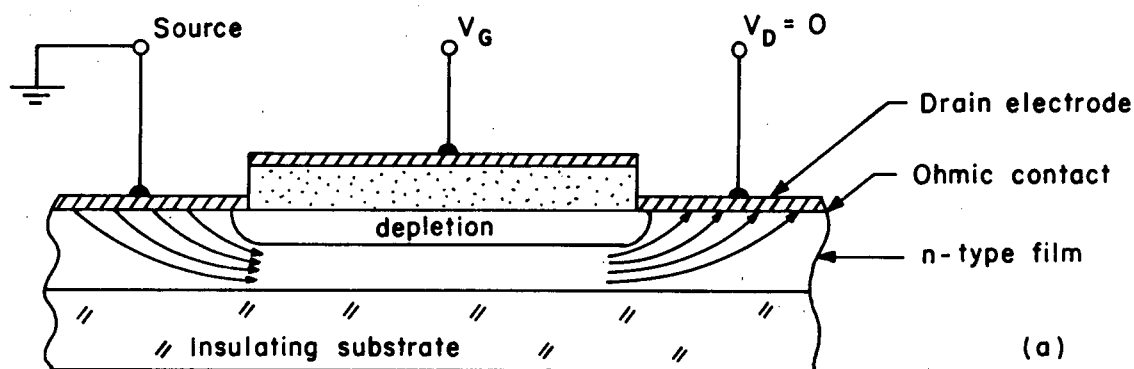
103

Figure 4-14. Deep Depletion Thin-Film Transistor Structures

(a) Qualitative illustration for V_D = 0.
(b) Deep depletion structure showing shape of depletion region under operating bias.
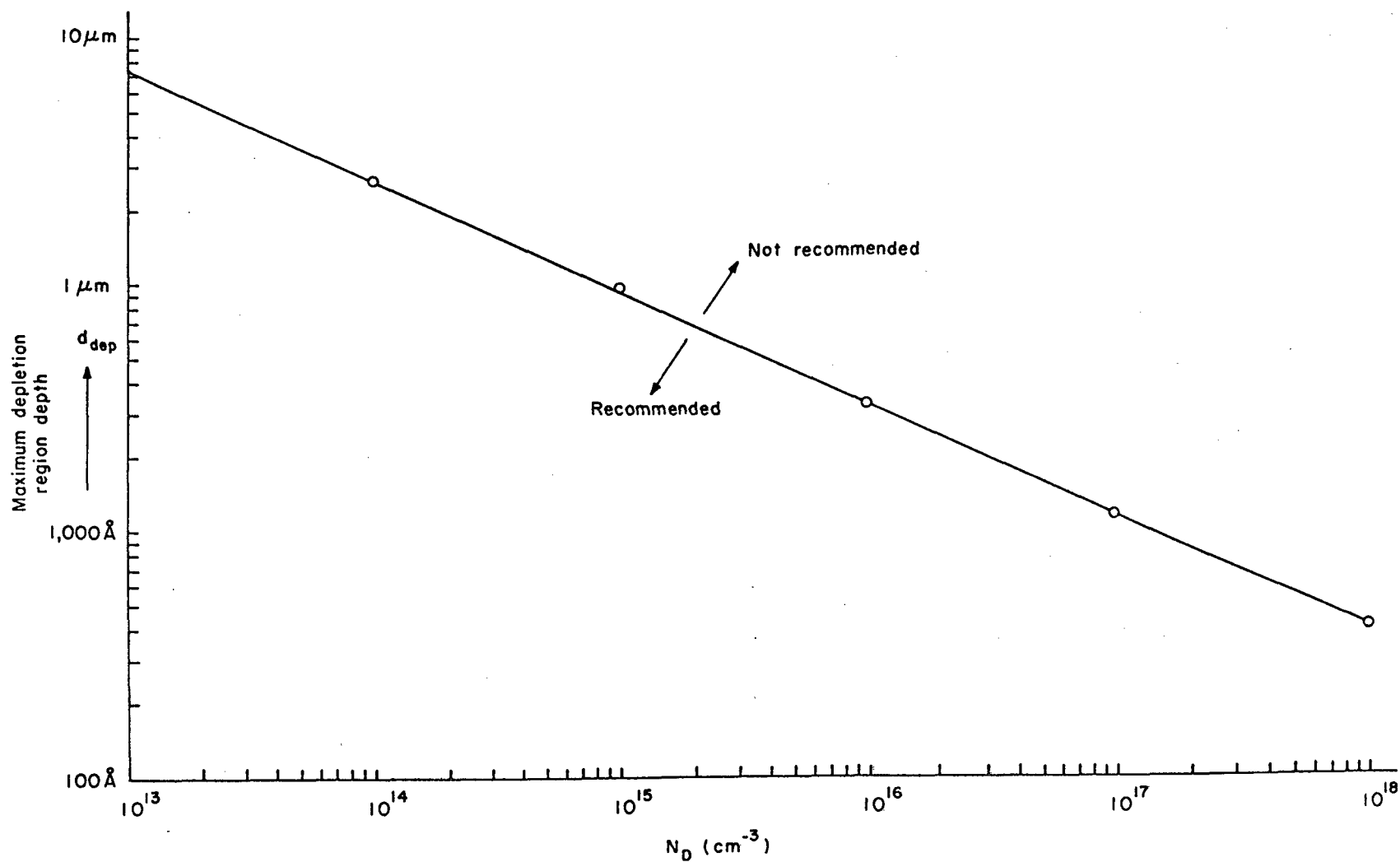(c) Minority carriers (holes) are conducted down the surface inversion layer to the source, when they recombine.

Figure 4-15.   Maximum Depletion Region Depth versus N_D for Silicon
(References 4-7, 4-8, and 4-9)

arises from the fact that the semiconductor layer is formed by vacuum deposition and a deposited layer contains many more defects and crystalline imperfections than the corresponding single-crystal semiconductor. Thus the trapping centers in the semiconductor layer will have a profound effect on the device characteristics. In addition, the trapping centers in the deposited insulator, the surface states and surface charges near or at the semiconductor-insulator interface, and the metal contacts to the semiconductor will influence the device performance. Actually the rectifying contacts in a TFT result in a low transconductance; large densities of traps and states can cause a reduction of the channel mobility and can affect the reliability, reproducibility, and performance of the TFT (Reference 4-3).

The interaction and effect of the surface trapping centers on a TFT will be considered. The source-drain conductance at zero source-drain voltage, g_D, and the small-signal AC transconductance in the saturation region, g_m, is given by (References 4-3 and 4-13)

$$g_D = \left(\frac{W}{L}\right) C_i \mu_e^* V_c \tag{4-3}$$

$$g_m = \left(\frac{W}{L}\right) C_i \mu_e^* (V_G - V_T) \left(\frac{dn_c}{dn} + \beta \frac{dn_t}{dn}\right) \tag{4-4}$$

$$g_m(\omega) = g_o \left\{ \frac{(\omega_1 + \beta\omega_2)^2 + \omega^2}{(\omega_1 + \omega_2)^2 + \omega^2} \right\}^{1/2} e^{j\theta} \tag{4-5}$$

where

$$\mu_e^* = \left(\frac{L}{W}\right) \frac{2}{C_i} \left[\frac{\partial}{\partial V_G} \sqrt{I_{Dsat}} \right]^2 \Bigg|_{V_D} , \text{ effective carrier mobility in the channel}$$

$$V_c \equiv \frac{q d_{sc}}{C_i} \cdot n_c , \text{ effective conducting channel voltage}$$

$$V_c = \frac{1}{2}[(V_G - V_T) - (V_t + V_1)] + \frac{1}{2}\{[(V_G - V_T) - (V_t + V_1)]^2$$

$$+ 4V_1(V_G - V_T)\}^{1/2}$$

$$V_T \equiv -\frac{qd_{sc}}{C_i}(n_{co} + n_{to}) \ , \ \text{threshold voltage}$$

$$V_t \equiv \frac{qd_{sc}}{C_i}N_t \ , \ \text{effective voltage drop due to traps}$$

$$V_1 \equiv \frac{qd_{sc}}{C_i}n_1 \ , \ \text{effective voltage drop due to } n_1$$

$$g_o \equiv \left(\frac{W}{L}\right)C_i\mu_e^*(n_{tdc})(V_G - V_T)$$

$$\beta \equiv \frac{n_c}{\mu_e^*}\left(\frac{d\mu_e^*}{dn_t}\right)$$

$$\omega_1 \equiv \frac{n_1\sigma_n\bar{v}}{\left(1 - \frac{n_{tdc}}{N_t}\right)}$$

$$\omega_2 \equiv N_t\sigma_n\bar{v}\left(1 - \frac{n_{tdc}}{N_t}\right)$$

$$\tan\theta = \frac{\omega_2(1 - \beta)\omega}{(\omega_1 + \omega_2)(\omega_1 + \beta\omega_2) + \omega^2}$$

$$\frac{dn_c}{dn} = \frac{\omega_1 + j\omega}{\omega_1 + \omega_2 + j\omega}$$

$$\frac{dn_t}{dn} = \frac{\omega_2}{\omega_1 + \omega_2 + j\omega}$$

$$n_1 = N_c e^{-\frac{E_t}{kT}}$$, available density of carrier present in the semiconductor if the Fermi level were at the trap level

$n = n_c + n_t$, total carrier density

$N_t - n_t$ = density of empty traps

n_c = density of conduction carriers

n_{co} = initial density of conduction carriers

n_t = density of filled traps

n_{to} = initial density of filled traps

N_t = total effective density of traps

N_c = effective density of states in the conduction band

E_t = ionization energy level of traps measured from conduction band edge

d_{sc} = semiconductor thickness or effective inversion depth

σ_n = capture cross section

$\bar{v}$ = average velocity of mobile carriers

$n_c = n_{cdc} + n_{cac} e^{j\omega t}$ for DC and AC parts of the gate voltage

$n_t = n_{tdc} + n_{tac} e^{j\omega t}$ for DC and AC parts of the gate voltage

For the small trap densities and large trap ionization energy (i.e., ideal case), Equations 4-3, 4-4, and 4-5 become

$$g_D = \left(\frac{W}{L}\right) C_i \mu_e^* (V_G - V_T)$$

$$g_m = \left(\frac{W}{L}\right) C_i \mu_e^* (V_G - V_T) \equiv g_o$$

since

$$V_G - V_T \gg V_t + V_1$$

V_1 is very small for small n_1

$$\frac{dn_c}{dn} \simeq 1 \quad \text{for small } n_t$$

$$\frac{dn_t}{dn} \simeq 0 \quad \text{for small } n_t$$

As $\omega \to 0$ and as $\omega \to \infty$, the transconductances are expressed by

$$g_{m, \omega \to o} = g_o \left(\frac{\omega_1 + \beta \omega_2}{\omega_1 + \omega_2} \right)$$

$$g_{m, \omega \to \infty} = g_o$$

For different values of β, the $|g_m(\omega)|$ can be classified as

if $\beta = 0$, $|g_m(\omega)|$ = an increasing function of frequency,

if $\beta = 1$, $|g_m(\omega)|$ = g_o (constant), and

if $\beta > 1$, $|g_m(\omega)|$ = a decreasing function of frequency

The trapping centers in the insulator can cause additional effects of drift and instability in the TFT. The kinetics of carrier transfer are given by

$$\frac{\partial n_t}{\partial t} = \bar{v} \sigma_n (N_t - n_t) n_c - \bar{v} \sigma_n n_t n_1$$

where all values are those for the insulator.

In a TFT, it is evident that the detailed transport processes are very complicated because of the large densities of traps which exist in the semiconductor, in the insulator, and at the surface. Therefore, in order to improve device reliability, reproducibility, and performance, the trap densities are to be reduced.

109

Thermal Limitations of the Thin-Film Transistor

In the simple treatment of the TFT, the gain-bandwidth product of the device is proportional to the carrier mobility and inversely proportional to the square of the source-drain spacing, L; therefore, to obtain high frequency operation the source-drain spacing should be reduced and a high mobility semiconductor should be used. However, power dissipation in the TFT is related to channel dimension as well as to the physical dimension of the device; thus the power dissipation will be introduced into the basic theoretical characteristics (Reference 4-14).

At the knee of the I_D versus V_D plot, the power dissipation per unit area is

$$P = \frac{I_{Dsat} \cdot V_{Dsat}}{WL}$$

where

$$I_{Dsat} = \left(\frac{W}{L}\right) \mu_e^* C_i \frac{(V_G - V_T)^2}{2}$$

$$V_{Dsat} = V_G - V_T = \left(\frac{2L^2 P}{\mu_e^* C_i}\right)^{1/3}$$

The gain-bandwidth product at the knee is then

$$[G \cdot BW] = f_m \simeq \frac{g_m}{2\pi C_i WL}$$

$$f_m \simeq \frac{\mu_e^* V_{Dsat}}{2\pi L^2} = \frac{1}{2\pi}\left(\frac{2}{C_i}\right)^{1/3}\left(\frac{\mu_e^*}{L^2}\right)^{2/3} P^{1/3}$$

The heat flow from the center of the heated region can be expressed as shown in Figure 4-16 by

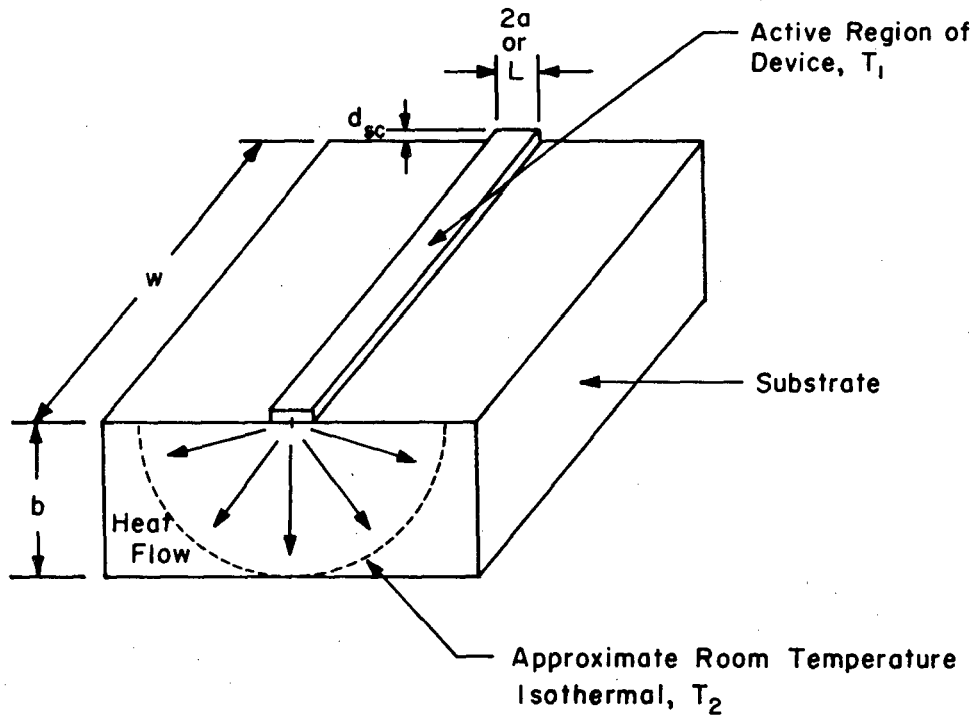$$H_{subs} = -\pi r \kappa W \frac{dT}{dr}$$

Figure 4-16. Heat Flow Pattern from a TFT

$$H_{subs} = \frac{\pi \kappa W (T_1 - T_2)}{\ell n \left(\frac{b}{a}\right)}$$

$$H_{el} = \frac{2d'_{el} \kappa' W (T_1 - T_2)}{b}$$

$$H_{rad} = 2.74 \times 10^{-12} E_1 \left(T_1^4 - T_2^4\right) WL \ \text{cal/sec}$$

where

H_{subs} = heat flow through an element distance r from channel

H_{el} = heat flow conducted away from the channel through the source and drain electrodes

H_{rad} = heat loss by radiation

r = radial distance from channel

κ = thermal conductivity of the insulating substrate

T_1 = temperature at the channel

T_2 = approximate room temperature isothermal

$a \equiv \dfrac{L}{2}$

b = substrate thickness

d'_{el} = metal electrode thickness

κ' = electrode thermal conductivity

E_1 = emissivity, $\approx$5-70 depending on metal and surface

The total power dissipation is then given by

$$P_{tot} = \frac{H_{subs} + H_{el} + H_{rad}}{WL}$$

The most important heat loss in solid-state materials is due to the substrate conduction. For a temperature rise of 75°C (T_1 = 100°C and T_2 = 25°C), the maximum power dissipation is about 300 W/cm^2 on a glass substrate and 10 KW/cm^2 on a sapphire substrate (Reference 4-14). Considering the power dissipation, the operation of a TFT is limited to the condition that the ($V_G - V_T$) and V_D values must be within the maximum permitted for the substrates used.

Evaluation of Fabricated MIS Thin-Film Transistors

Elemental tellurium has advantages over III-V and II-VI compound semiconductors since it is easily evaporated. Dissociation and stoichiometric problems as encountered with materials such as CdS, GaAs, InSb, do not exist for evaporated tellurium.

The starting source material was semiconductor grade p-type tellurium of 99.999% purity from Electronic Space Products, Inc. The gate electrode was deposited upon the Al_2O_3 coated glass substrate, followed by the electron-beam evaporated Al_2O_3 or anodized Al_2O_3 insulator, the gold source and drain electrodes, the tellurium, and the Al_2O_3 protective overcoating, in that order. The fabrication processes are detailed in Appendix B. The resulting TFTs exhibited both depletion and enhancement type characteristics. Drain current versus voltage characteristics for a typical Al-Al_2O_3-Au-Te transistor are shown in Figure 4-17.
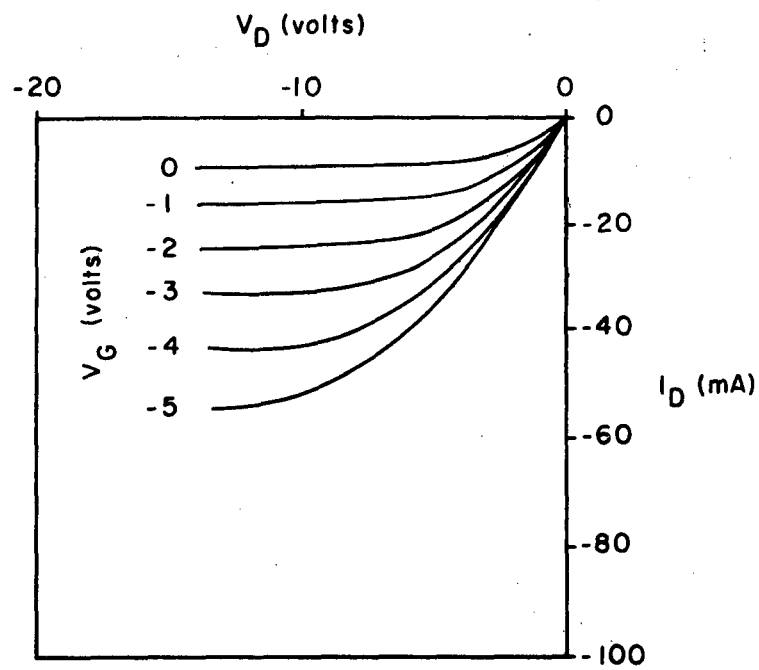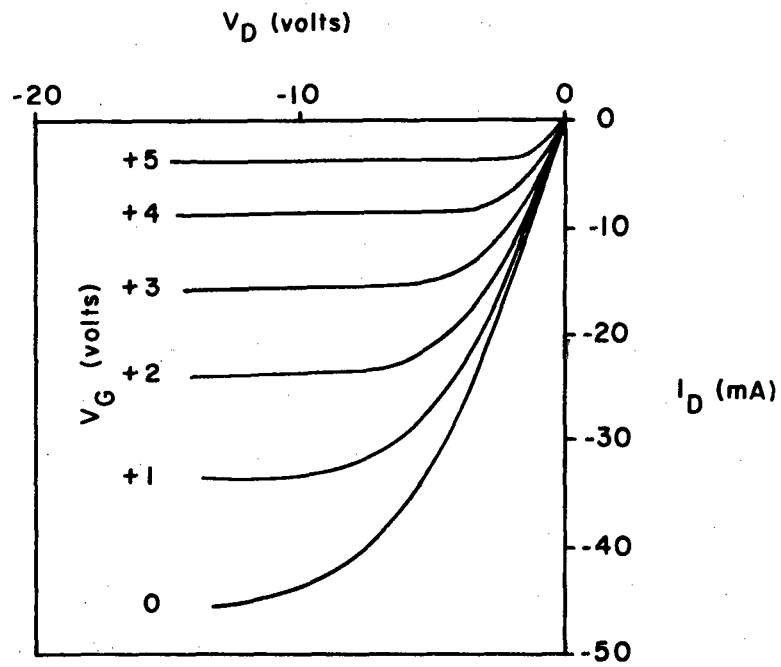
Figure 4-17. I_D-V_D Characteristics of Al-Al$_2$O$_3$-Te TFTs

Data which will be used for evaluation of the fabricated Te TFTs are the following:

Geometry: $W = 600{-}750$ mils, $L = 3{-}5$ mils, and $W/L = 120{-}250$

Mobility: 42.5 cm^2/V-sec for 100 Å (UNM data)

65.0 cm^2/V-sec for 130 Å (Reference 4-16)

130 cm^2/V-sec for 200 Å (Reference 4-16)

250 cm^2/V-sec for 400 Å (Reference 4-16)

200 cm^2/V-sec for 150 Å (Reference 4-15)

Carrier density: 1 to 3 x 10^{18} atoms/cm^3 (Reference 4-16)

Insulator: Al_2O_3 (400 Å or 1,500 Å thick)

For the values of $W/L = 200$, $C_i = 1.6$ x 10^{-7} F/cm^2, $V_T = 4$ V, and $\mu^* = 42.4$ cm^2/V-sec, the drain characteristic curves can be plotted. The theoretical and experimental characteristics of the $Al{-}Al_2O_3{-}Te$ thin-film transistors are shown in Figure 4-18.

In order to investigate the effect of traps and surface states on the thin-film transistors, the following calculations are needed. For $d_{sc} = 100$ Å, $V_T = 4$ V, $n_{co} = 3$ x 10^{18} cm^{-3}, and initial occupancy of 80% ($f_{to} \equiv n_{to}/N_t = 0.8$), the important data are obtained as

$$n_o = \frac{V_T C_i}{q d_{sc}} = 4 \times 10^{18} \text{ cm}^{-3}$$

$$n_{to} = n_o - n_{co} = 10^{18} \text{ cm}^{-3}$$

$$N_t = \frac{n_{to}}{f_{to}} = 1.25 \times 10^{18} \text{ cm}^{-3}$$

$$V_t = \frac{q d_{sc}}{C_i} N_t = 1.25 \text{ volt}$$

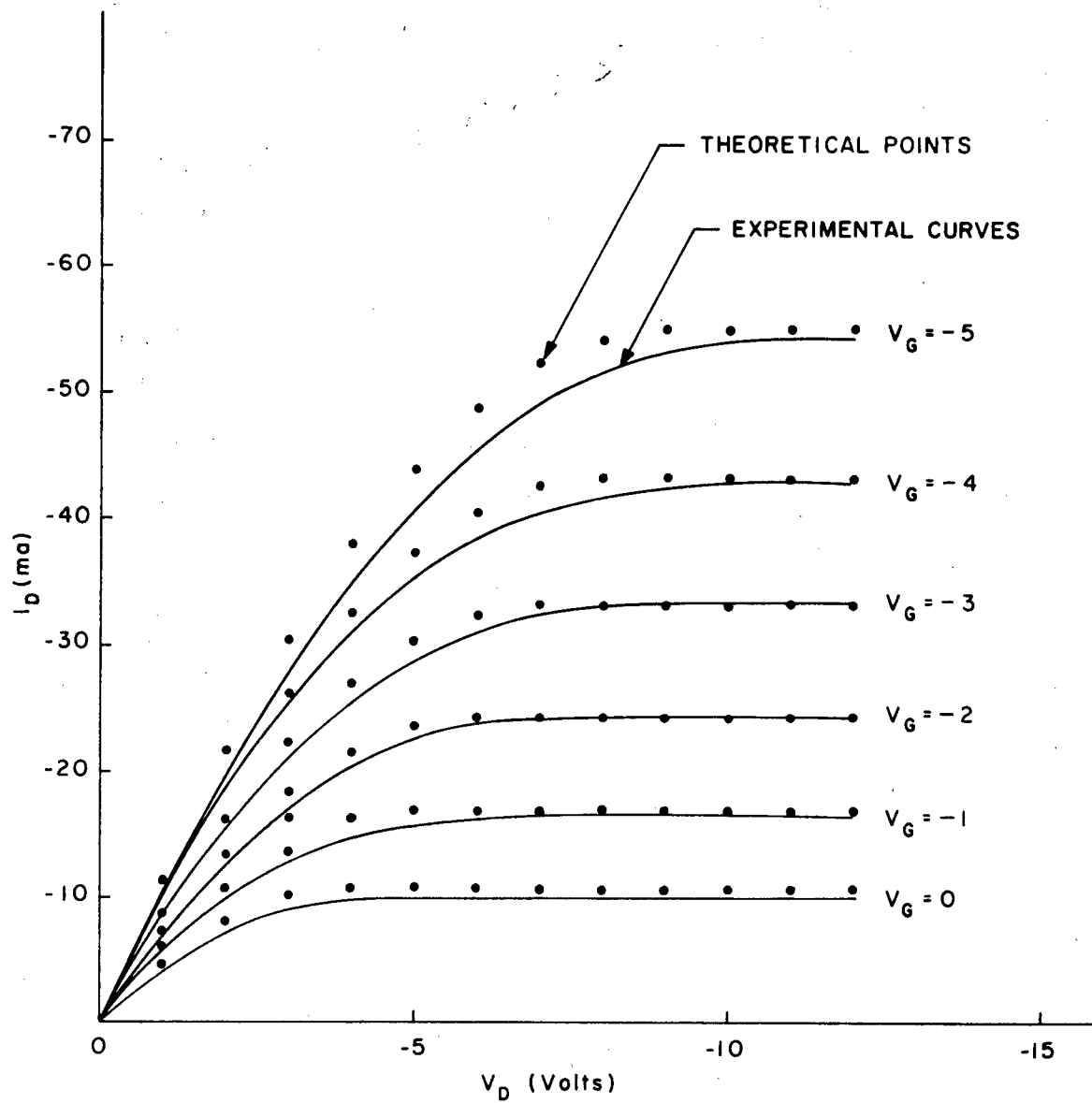$$n_1 = \frac{1 - f_{to}}{f_{to}} n_{co} = 7.5 \times 10^{17} \text{ cm}^{-3}$$

Figure 4-18. Output Characteristics of p-Type
Te TFTs with Al_2O_3 Insulator

$$V_1 = \frac{n_1 q d_{sc}}{C_i} = 0.75 \text{ volt}$$

$$V_C = \frac{1}{2}\{(V_G - 2) - [(V_G - 2)^2 - 3(V_G - 4)]^{1/2}\}$$

The V_C and g_D versus V_G curves are shown in Figure 4-19. For $V_G - V_T = 1$ volt and $V_D = 1$ volt, the transconductance is $g_m = 9$ mmhos, and the gain-bandwidth product, f_m, is obtained as

$$f_m \approx \frac{g_m}{2 \, C_i WL} = 0.77 \times 10^6 \text{ Hz}$$

Since the operating temperature of the TFTs is higher than the ambient (e.g., $\Delta T = T_1 - T_2 = 75°C$), the thermal conductivity of the substrate material and the dimensions of the device are used for calculating the power dissipation and maximum gain-bandwidth product. For $\Delta T = 75°C$, $\kappa = 8.4 \times 10^{-3}$ watt/cm^2-°C for glass, $\kappa = 2.94 \times 10^{-1}$ watt/cm^2-°C for sapphire, $a = 3.81 \times 10^{-3}$ cm, $b = 2 \times 10^{-2}$ cm, $W = 1.52$ cm, $L = 7.6 \times 10^{-3}$ cm, $WL = 1.155 \times 10^{-2}$ cm^2, $d'_{el} = 10^{-5}$ cm, $\kappa' = 6.72 \times 10^{-3}$ watt/cm^2-°C, and $E_1 \approx 50$, the maximum allowable powers can be computed as

$$P_{tot} = 3.05 \text{ W for glass}$$

$$P'_{tot} = 265 \text{ W/cm}^2 \text{ for glass}$$

$$P_{tot} = 42.7 \text{ W for sapphire}$$

$$P'_{tot} = 3.7 \text{ KW/cm}^2 \text{ for sapphire}$$

From the above maximum powers, the gain-bandwidth products may be calculated as

$$f_m = 6.43 \times 10^5 (P)^{1/3} = 0.87 \times 10^6 \text{ Hz for glass}$$

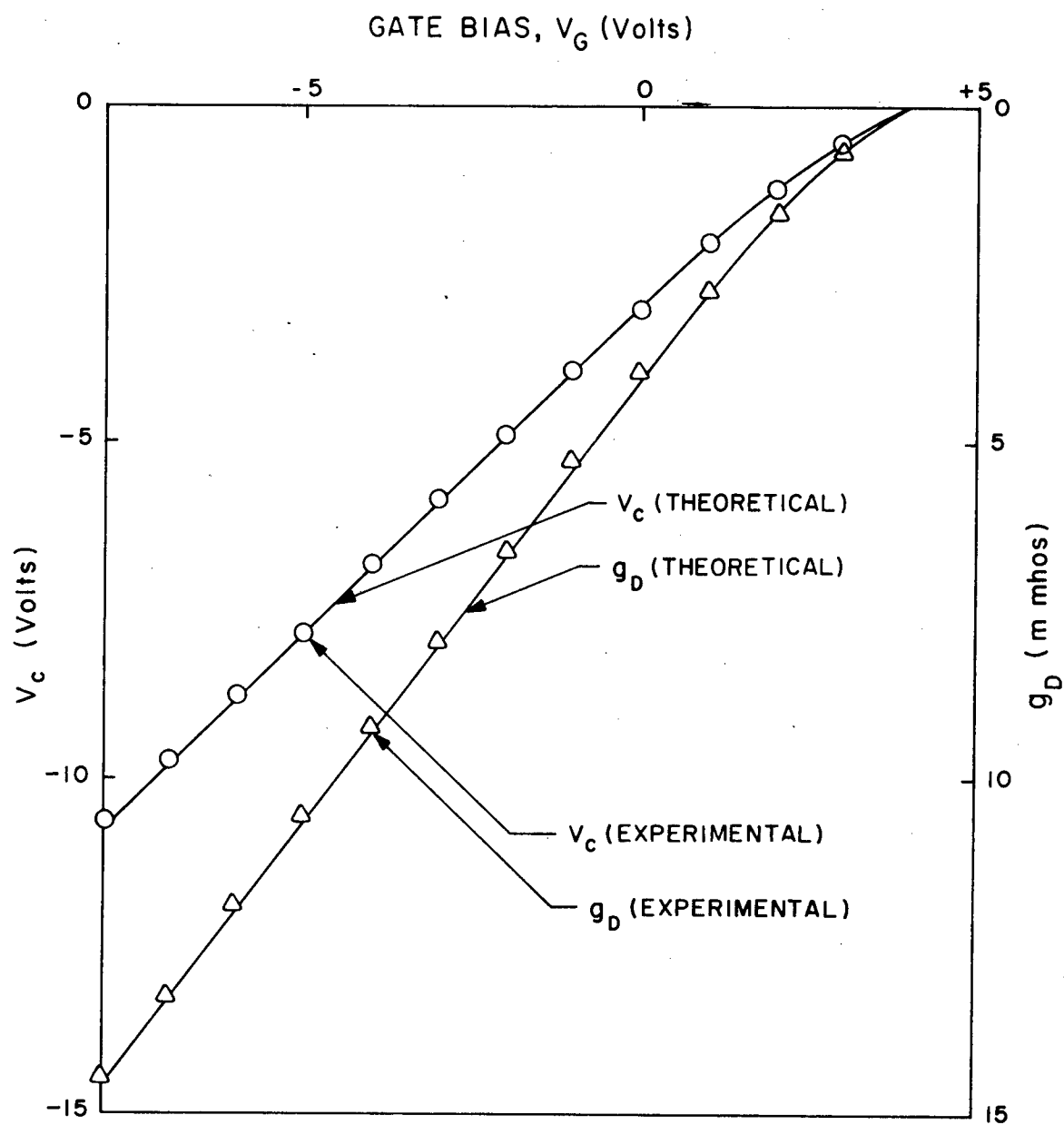$$f_m = 2.25 \times 10^6 \text{ Hz for sapphire}$$

GATE BIAS, V_G (Volts)

Figure 4-19. Effective Conducting Channel Voltage and
Conductance Characteristics of Al-Al$_2$O$_3$-Te TFTs

The tellurium thin-film transistor showed good saturation characteristics for a thin semiconductor ($\sim$100 Å); however, above 100 Å, I_D - V_D curves became stiffer and around 300 Å the triode characteristics were observed. The transconductance value can be increased by reducing the source-drain gap (L) and resulted in wide gain-bandwidth product. Depletion mode drain characteristics were also obtained, and the transconductance values were comparable to the enhancement mode (Figure 4-17).

References

4-1.   P. K. Wiemer, "The TFT--A New Thin Film Transistor," *Proc. IRE*, Vol. 50, p. 1462, 1962.

4-2.   R. S. C. Cobbold, *Theory and Application of Field Effect Transistors*, John Wiley and Sons, N.Y., 1970.

4-3.   S. M. Sze, *Physics of Semiconductor Devices*, John Wiley and Sons, N.Y., 1969.

4-4.   M. H. White, "MOS Transistors," in *Semiconductors and Semimetals* (ed. Willardson and Beer), Vol. 7, Part A, Academic Press, N.Y., 1971.

4-5.   D. H. Phillips and W. W. Grannemann, *Gallium-Arsenide-Phosphide MIS Capacitor Fabrication and Radiation Studies*, Bureau of Engineering Research Technical Report EE-195(72)ONR-005, The University of New Mexico, May 1972.

4-6.   D. Hoffman and D. Leibowitz, "Al_2O_3 Films Prepared by Electron-Beam Evaporation of Hot-Pressed Al_2O_3 in Oxygen Ambient," *Journal of Vacuum Science and Technology*, Vol. 8, No. 1, p. 107, 1971.

4-7.   D. Hoffman and D. Leibowitz, "Effect of Substrate Potential on Al_2O_3 Films Prepared by Electron Beam Evaporation," *Journal of Vacuum Science and Technology*, Vol. 9, No. 1, 1972.

4-8.   M. Kamoshita, I. V. Mitchell, and J. W. Mayer, "Influence of Heat Treatment on Aluminum Oxide Films on Silicon," *Journal of Applied Physics*, Vol. 43, No. 4, April 1972.

4-9.   S. R. Hofstein, "An Analysis of Deep Depletion Thin-Film MOS Transistors," *IEEE Transactions on Electron Devices*, Vol. ED-13, No. 12, p. 846, December 1966.

4-10. B. E. Deal, A. S. Grove, E. H. Snow, and C. T. Sah, "Observation of Impurity Redistribution during Thermal Oxidation of Silicon Using the MOS Structure," *Journal of Electrochemical Society*, Vol. 112, p. 308, March 1965.

4-11. F. P. Heiman, "Thin-Film Silicon-on-Sapphire Deep Depletion MOS Transistors," *IEEE Transactions on Electron Devices*, Vol. ED-13, No. 12, p. 855, December 1966.

4-12. A. S. Grove, B. E. Deal, E. H. Snow, and C. T. Sah, "Investigation of Thermally Oxidized Silicon Surfaces Using Metal-Oxide-Semiconductor Structure," *Solid State Electronics*, Vol. 8, p. 145, February 1965.

4-13. C. A. T. Salama and L. Young, "Evaporated Silicon Thin Film Transistors," *Solid State Electronics*, Vol. 10, p. 473, 1967.

4-14. D. J. Page, "Thermal Limitation of the Thin Film Transistor," *Solid State Electronics*, Vol. 11, p. 87, 1968.

4-15. P. K. Wiemer, "A p-type Tellurium Thin Film Transistor," *Proceedings of IEEE (Corresp.)*, Vol. 52, p. 608, May 1964.

4-16. R. W. Dutton and R. S. Muller, "Electrical Properties of Tellurium Thin Films," *Proceedings of the IEEE*, Vol. 59, No. 10, October 1971.

SUMMARY AND CONCLUSIONS

Thin-film structure and formation were studied and high mobility thin films of indium antimonide were prepared using the electron-beam evaporation technique. Thin-film Hall devices and magnetoresistors were fabricated, electrically tested, and the electron and stable fast neutron radiation effects on the films were studied. GaAsP and silicon MIS capacitors were fabricated by using aluminum oxide (Al_2O_3) as well as silicon oxide (SiO_x). Tellurium thin-film transistors were also fabricated using electron-beam evaporated Al_2O_3 and the wet anodization of aluminum. The device stability was studied before and after thermal annealing in various gases.

The physical properties of the InSb compound semiconductor were studied to understand the detailed mechanism of thin-film nucleation and growth. Effects of vacuum chamber pressure, deposition rate, defects, grain boundaries, and surface scattering were investigated. It was found that the larger grain size resulted in high mobility. High mobility InSb thin films were obtained using a modified electron-beam evaporation technique and recrystallization. Polycrystalline n-type indium antimonide was evaporated from a tungsten or molybdenum boat with an electron beam at rates of 300 to 500 Å/sec on precleaned glass substrates, maintained at 300°C, at a pressure of 2 to 3 x 10^{-7} torr. It is important to evaporate all the charges of indium antimonide from the boat. Thicknesses of these films varied between 2.5 and 5.2 microns. Before recrystallization the films were heated in an oven at 250°C for about 20 minutes to form a protective layer of oxide. Recrystallization was done in dry argon ambient (2 liters/min) between 520 and 535°C for 2 to 3 minutes. Electron Hall mobilities, measured by van der Pauw's method, ranged from 40,000 to 68,000 cm^2/V-sec.

Galvanomagnetic coefficients of bulk rectangular Hall devices were obtained as Hall coefficient of 310 cm^3/coul, conductivity of 252 ohm^{-1} cm^{-1}, carrier concentration of 2.22 x 10^{16} cm^{-3}, and Hall mobility of 78,000 cm^2/V-sec. For two-layer rectangular thin-film Hall devices,

galvanomagnetic coefficients of σ_{eff} = 200 ohm^{-1} cm^{-1}, μ_{eff} = 66,000 cm^2/V-sec, R_{Heff} = 330 cm^3/coul, σ_s = 234 ohm^{-1} cm^{-1}, μ_s = 1,000 cm^2/V-sec, R_{HS} = 4.28 cm^3/coul, n_s = 1.605 x 10^{18} cm^{-3}, σ_b = 195 ohm^{-1} cm^{-1}, μ_b = 68,000 cm^2/V-sec, R_{Hb} = 349 cm^3/coul, and $\langle n_b \rangle$ = 1.97 x 10^{16} cm^{-3} were computed at room temperature. For two-layer Corbino disks, σ_s = 234 ohm^{-1} cm^{-1}, R_{HS} = 4.28 cm^3/coul, μ_{es} = 1,000 cm^2/V-sec, n_s = 1.605 x 10^{18} cm^{-3}, σ_b = 195 ohm^{-1} cm^{-1}, R_{Hb} = 349 cm^3/coul, μ_{eb} = 68,000 cm^2/V-sec, and n_b = 1.97 x 10^{16} cm^{-3} were measured at room temperature. For Corbino disks of two-layer thin film, a magnetoresistance of 18 was obtained at B = 10 Kgauss.

These films, when irradiated with electron dose rates of 6 x 10^9 rads(InSb)/sec at 1.3 MeV and 2 x 10^{11} rads(InSb)/sec at 2.3 MeV as well as when irradiated with neutron fluences of 10^{14}, 10^{15}, and 10^{16} nvt, did not indicate any change in electron mobilities. However, at 10^{17} nvt, electron mobilities of all these films dropped below 20,000 cm^2/V-sec. The carrier removal rates range from 0.247 to 3.350 cm^{-1}. For insufficiently recrystallized InSb thin films, the opposite sign of the carrier removal rate is observed.

Al_2O_3 (99.999% purity) was used for electron-beam evaporation source material. The insulating films of Al_2O_3 were deposited from single-crystal sapphire at rates of 60 to 200 Å/min in an oxygen background of 5 x 10^{-5} torr to minimize dissociation of Al_2O_3. The semiconductors are n-type $GaAs_{1/2}P_{1/2}$ and silicon with precleaned surfaces. Gate metals are aluminum and chromium; evaporated silver formed ohmic contact at the bottom. The fabricated MIS devices are annealed at 250°C in helium ambient (1 liter/min) for 20 minutes and in oxygen (1 liter/min) for 40 minutes. The C-V measurement showed excellent stability—even the hysteresis loop is almost indistinguishable—since these annealings remove the charges in the insulating layer. Inversion was observed in silicon MIS capacitors; however, depletion rather than inversion was observed in GaAsP MIS capacitors even at low negative bias voltage (~40 volts). This characteristic could be caused by shortage of the minority carriers in the bulk or at the interface or by ineffectiveness of the minority carriers. Electron-beam evaporated silicon monoxide was also used for a dielectric, but instability was observed. An

Al_2O_3 insulator was obtained in a 0.05 N ammonium phosphate ($NH_4H_2PO_4$) electrolytic cell. The advantage of anodized Al_2O_3 is that it yields a thinner insulating layer (~400 Å); however, electron-beam evaporated Al_2O_3 contains fewer charged ions in the dielectric than does anodized Al_2O_3.

For the silicon MIS capacitor, typical values of surface-state charge and surface-state density were -5.21 x 10^{-9} coul/cm^2 and 3.26 x 10^{10} states/cm^2, respectively. For the $GaAs_{1/2}P_{1/2}$ MIS capacitor, surface-state charge of -1.175 x 10^{-8} coul/cm^2 and surface-state density of 7.35 x 10^{10} states/cm^2 were obtained. Constant capacitance values (C_i) were 13 pf for silicon and 4.6 pf for GaAsP. The resistivity and break-down voltage of fabricated Al_2O_3 ranged from 10^{13} to 10^{14} ohm-cm and from 2.2 x 10^6 to 2.8 x 10^6 V/cm, respectively.

MIS thin-film transistors of InSb and Te were fabricated using photoengraving techniques. With InSb, in spite of extensive experimental work, a high-transconductance TFT with well-saturated characteristics was not obtained. However, with Te, a rather high-transconductance TFT with well-saturated characteristics could be fabricated. A chromium gate could not be used because of etching difficulties; therefore, an aluminum gate with dimensions of 5 x 600 mils was used. The source and drain metal was gold. Thicknesses of the insulator and semiconductor were ~450 Å and ~100 Å, respectively. For V_G - V_T = 1 V and V_D = 1 V, g_m ≈ 9 x 10^{-3} mho and f_m ≈ 0.77 x 10^6 Hz were obtained.